Dielectric elastomer actuators

Kofod, Guggi

Publication date:
2001

Document Version
Publisher's PDF, also known as Version of record

Dielectric elastomer actuators

Guggi Kofod

Ph.D. thesis, September 2001

The Technical University of Denmark

This work took place in The Danish Polymer Centre, Risø National Laboratory and The Department of Chemistry, Technical University of Denmark between 1st of September 1998, and 1st of September 2001. The supervisors of the project were professor Steen Skaarup, Department of Chemistry, Technical University of Denmark, and Senior Scientist Peter Sommer-Larsen, The Danish Polymer Centre, Risø National Laboratory.
During the Ph.D. study, 5 months were spent with project work at SRI International in Menlo Park, California. Here the daily supervisor was Research Scientist Roy Kornbluh.
The Danish Research Agency supports the project through the THOR programme (Technology by Highly Oriented Research). GRANT No. 9700882
The Ph.D. project was part of the Artificial Muscles – ARTMUS project, a collaboration between Danfoss A/S, Department of Chemistry at DTU, and The Danish Polymer Centre at Risø.

The Thesis is submitted to the Department of Chemistry, Technical University of Denmark, for partial fulfilment of the requirements for the Ph.D. degree.

Risø report number: Risø-R-1286(EN)
ISBN: 87–550–2924–8 ; 87–550–2925–6 (Internet)
ISSN: 0106–2840

Print: Pitney Bowes Management Services Denmark A/S, 2001

Abstract

Stress and strain are introduced as tensor properties. Several theoretical models of stress-strain behaviour are presented, of which the Ogden model is capable of fitting the observed behaviour in the entire range of measurement. Dielectricity is defined, and Maxwell stress is derived. The theories of elasticity and Maxwell stress are combined, in the special case of a dielectric elastomer actuator (DEA) constrained in width. The resulting model has no adjustable parameters.

Percolation properties are introduced, and an experiment is presented, in which the fraction of conducting graphite in insulating silicone rubber is varied. Mixtures of conducting carbon black in insulating polymer were developed and used as compliant electrodes. In order to produce stable electrodes, a system of one-component silicone glue and Ketjenblack suspended in heptane is developed. This mixture is sprayed on pre-strained silicone elastomer films, providing stable compliant electrodes.

Procedures for manufacturing of DEA with two kinds of elastomer film are presented. Silicone actuators are made from spun elastomer films. Handling of thin silicone elastomer films is possible if temporary frames are used. VHB™4910 actuators are made from a commercial glue, which has a higher dielectric constant and stretches farther than silicone. The manufacture and handling of VHB™4910 actuators is easier, since the film itself provides gluing, such that frames and electrodes are very easy to apply. These DEA structures are simple, making it easier to describe them theoretically.

Force-strain measurements are obtained using an actuator test bench. For a silicone actuator, the force-strain curve included artefacts of the additional stress from the compliant electrodes. Introducing a cut-off function, similar to the Fermi-Dirac distribution function, it is possible to fit the force-strain curve in the whole range of strain.

The blocking force of a VHB™4910 actuator is presented. The dependence of the blocking force on applied voltage was parabolic, as expected from the Maxwell stress equation. There are discrepancies, which are explained as a channelling of the developed actuation stress in the transversal direction.

Measurements of electric breakdown strength of pre-strained VHB™4910 are presented, for isotropic pre-strains. The electric breakdown strength is shown to be near inversely proportional to the thickness of the stretched elas-

tomer, increasing from 17 MV/m to 270 MV/m.

The actuator test bench is programmed to simulate a constant applied weight through force feedback. An automated data collection program was written, which varies the applied voltage and weight. The actuated lengths are plotted in 3D-plots, which produces nicely interconnected plot surfaces, a sign of how well the actuator test bench functions.

Measurements are performed on both silicone elastomer and VHB™4910 actuators. A pronounced peak is observed in the 'engineering' strain, stating the fact that there is an optimum applied weight at which the highest actuated strain is obtained.

The parameters of the actuators are inserted in the derived model. Quantitative correspondence between experimental results and model prediction is found for the silicone actuator. The predictions for the VHB™4910 actuators do not match well with results, though there is qualitative agreement.

Contents

Acknowledgements

I would like to thank the following: My supervisor at Risø, Peter Sommer-Larsen, for the opportunity to work on this project, as well as for valuable discussions. Roy Kornbluh at SRI International, for his help and friendship during my stay at SRI International, for which I am also grateful. Keld West, for his kind help, whenever it was needed. Technician Torben Kjær, who built the actuator test bench, and solved all major technical problems.

The following companies are acknowledged: Akzo Nobel, Denmark, who donated a sample of Ketjenblack EC-300J. Wacker© Sweden, who donated tubes of Elastosil 43® RTV-1 Silicone Glue. Hydrin (P/N C2000LL) was donated by ZEON Chemicals, Inc., Kentucky. 3M™Denmark supplied a roll of VHB™4910 tape. The Danfoss Foundation (Mads Clausen og Frues Fond) granted a broadband dielectric spectrometer to the ARTMUS project.

I would also like to thank all my friends. Finally, I would like to thank the most important person in my life, Pernille.

1

Introduction

This thesis concerns the physical realisation and theoretical description of dielectric elastomer actuators. These are insulating, rubber-like structures, capable of undergoing reversible length change and producing work. An often used, popular description of a dielectric elastomer actuator (DEA) terms it an 'artificial rubber muscle'. The terms 'artificial' and 'rubber' usually poses no problem to the interested listener, though the term 'muscle' often gives rise to misunderstandings. To avoid any misunderstanding, the best description of a DEA is that it works just like an electrical motor, but instead of rotation, it produces linear motion. The linear motion is the defining feature; the similarity with a muscle is only brought to attention because the DEA outputs linear motion, just like the muscle.

Why produce electric actuators, when electric motors are very efficient as well as powerful actuators? The answer is simple: the electric engine outputs rotational motion, while the DEA outputs linear motion. Perfecting the DEA opens up new possibilities for design of robots, orthopaedic assists, toys, telepresence, etc.

A dielectric elastomer actuator is basically a compliant capacitor. The dielectric medium consists of incompressible, yet highly deformable elastomeric material. The electrodes are designed to be able to comply with the deformations of the elastomer. As for any capacitor, when an electric field is applied to the electrodes, positive charges appear on one electrode, and negative charges on the other. This gives rise to Coulomb forces between opposite charges, generating a pressure, known as the Maxwell stress. The Maxwell stress forces the electrodes to move closer, thereby squeezing the elastomer. As the elastomer is thinned, it elongates in the directions perpendicular to the applied force. Exploiting this simple principle involves materials design and processing, as well as design of actuator geometries.

The field has evolved over the last 15 years from a theoretical idea [1], to the main concern of ten research groups or more. First it was recognised that the polymer poly(vinylidene flouride) (PVDF) has potential as actuating material [1]. PVDF is an electrostrictive material, in which the dielectric con-

stant depends upon the strain of the material. In 1994, one of the first articles on electrically induced strain in this material appeared [2], in which a strain of 3% was reported. At the time this strain was an enormous improvement, which is appreciated when knowing that the only other field-actuated materials, piezoelectrics, produced strains of less than 1 per thousand. Later, it was realised that copolymerising PVDF with triflouroethylene, to produce poly(vinylideneflouride-triflouroethylene) (P(VDF-TrFE)), would increase the output strain [3], as would also breaking up the polarisation domains by the use of high-energy electron radiation [4–7]. These measures have raised the output strain to 4%. At the *Smart Structures and Materials 2001: Electroactive Polymers and Devices* conference [8], arranged by SPIE in 2001, electrostrictive actuators made from ter-polymers of P(VDF-TrFE) and hexaflouropropylene (HFP) or chlorotriflouroethylene (CTFE) were introduced [9], giving rise to strains of 5%. PVDF and its co/ter-polymers may have low strains compared to DEA, but they output large actuation stress, on the order of 500 MPa at an electric field of 250 MV/m [4–7,9], compared to the 7 MPa record of DEA [10]. The high stress may be transformed into longer stroke by the use of active frames, such as cymbals [9]. Typically, such a scheme involves moving and sliding parts, introducing undesirable mechanical wear.

Another electrostrictive polymer is polyurethane (PU), which is a physically cross-linked elastomer, in which the polymer chains comprise hard and soft segments. Small crystallites act as cross-links, while the hard and soft segments endow the elastomer with its mechanical and dielectric properties [11–18]. Upon variation of the hard and soft segments, the dielectric constant may reach values as high as 7, by which a strain of 1.34% at an electric field of 0.25 MV/m have been observed [11]. The electrostrictive and Maxwell parts of the strain coefficient have been evaluated theoretically [16] and experimentally [14, 16]. The Maxwell part can comprise from 10% to 60%, depending upon temperature when close to the glass transition temperature. An actuator made from only polymer constituents was demonstrated, with PU as the dielectric medium and conducting polymer (polypyrrole) as the electrodes [17]. The highest applied electric field so far is 5 MV/m [18], which is quite small compared to other field-actuated polymers. The electric field is limited to low values because PU has a relatively high loss, originating from ionic conductivity. These free ions are probably residues from polymerisation reactions. If it were possible to raise the applied electric field to the levels possible for other polymers, a much higher strain response would result. The actuation stress is high, but the polymer in its elastomer form is typically quite stiff, therefore

impeding high strain.

So far, actuators made from elastomer showing both an electrostrictive and a Maxwell stress component have been discussed. The term dielectric elastomer actuator (DEA) is reserved for the class of polymer actuators that show a Maxwell stress component only. The elastomers used in this thesis, silicone rubber and VHB™4910 acrylic glue, both show no, or very little, electrostriction. The number of groups committed to working with DEA is small. The group at SRI International is very productive [10, 19–23]. Comprehensive materials comparison studies have been performed [21], and a large number of actuator geometries have been devised and examined, including DEA loud speakers [20, 24]. This group is by far the most successful when it comes to applications, and it was within this group that the discovery of the very high actuation strain polymer, 3M™VHB™4910 , was made [10]. Using this polymer in an actuator with a special geometry, active area strains of 380% were observed [25]. VHB™4910 was used by a Korean university collaboration as the active material, in a versatile spring-loaded actuator [26].

DEA and related polymer actuators, known collectively as field-actuated electro-active polymer (EAP) actuators, all share one common drawback: the driving voltage is high. Typical driving voltages lie in the range between 3 kV and 10 kV, depending on the polymer breakdown field and thickness of the polymer film. Recently, switch-mode amplifiers able of converting from 10 V to 1000 V, have attained very small sizes, $\sim$ 2.5 mm $\times$ 2.5 mm $\times$ 2.5 mm, allowing the possibility of incorporating low to high voltage conversion inside the DEA. Also, transistors working at 1 kV have reached the market, and therefore there are no constraints concerning electronics. Actually, working with high voltages could in some applications prove advantageous, since then only small currents are needed, which would lower the loss due to resistance in wires and compliant electrodes. Applications that are not sensitive to high voltages can easily be made with field-actuated EAP actuators. If the application is sensitive to high voltages, like toys and orthopaedic assists, then these actuators could still be put to use, since it is possible to seal the high voltages within the actuator structure.

In the proceedings for the conference *Smart Structures and Materials 2001: Electroactive Polymer Actuators and Devices* [8], other applications are outlined. NASA has always had an interest in lightweight materials, and there is a special interest towards EAP for mobile applications on other planets. Dr. Yoseph Bar-Cohen, the NASA proponent of EAP, lists successful devices [27]: catheter steering element, miniature manipulator and robotics, miniature robotic arms,

grippers, loudspeakers, active diapragms, and dust-wipers. A more novel application is suggested in an article named “Biologically inspired robots” [28]. In this article the ‘soft’ material and dynamic properties of EAP is recognised as opening new areas of application for robot engineering, especially for biomimetic robots. Biomimetic robots that mimic biological structures in design, inherently require muscle-like actuators for optimal functioning.

In this thesis, theories describing the deformation of elastomers will be presented, in historical order. The predictions of the theoretical models are tested against an experiment on a regular rubber string. Elasticity theory is important for description of the elastic nature of the DEA.

A presentation of dielectricity follows, with a simple derivation of the Maxwell stress, the driving force in the DEA. The theories of elasticity and Maxwell stress are combined, to produce a theory for predicting the actuation properties of the DEA. In the final expression there will be no adjustable parameters, except for the elastic parameters obtained on the actuator before measuring it.

The function of the compliant electrodes employed here, rely on percolation of charge through a loosely connected network of graphite particles in an insulating matrix. A simple percolation experiment on graphite in silicone rubber is presented, together with basic percolation theory. The manufacture of compliant electrodes is then presented, for the types of electrodes used here.

The experimental procedures used here for the manufacture of DEA’s are out-lined. Only thin film DEA’s are presented. Here, they have been made from two kinds of elastomer film, and with several types of compliant electrode. The DEA test bench is presented, and the data collection programs are described.

Finally, the experiments pertaining to DEA are detailed. Stress-strain curves and dielectric breakdown strength measurements are presented. Actuation properties of the two types of actuator are presented in several kinds of plots for better interpretation, and for all measured actuators, the theoretical predictions are compared to the experimental data.

2

Theory of elasticity

Materials with high elastic strains became available in 1839 by the method of vulcanisation for cross-linking of rubber-tree sap, invented by Charles Goodyear. Although the materials became available, the theoretical methods for treating high elastic strain were not available until much later, instigated by the origin of synthetic rubbers invented during the Second World War by German scientists. The initial theoretical work on finite deformations (as opposed to infinitesimal deformations) was undertaken in the 1940's.

In this chapter, the concept of elasticity is introduced by treating the case of an ordinary rubber string. Various models are introduced and their ability to describe the force behaviour of the rubber string is evaluated. The goal is to reach a large strain elasticity model, which is essential for creating a good model of the dielectric elastomer actuator.

2.1 Polymer materials

A polymer is a molecule, composed of a large number of identical units in a long chain; the units are known as monomers. The polymer is created by a chemical reaction between the monomers known as polymerisation, which links the monomers together [29]. One such reaction is the addition polymerisation of ethylene monomers,

$$-CH_2\cdot + H_2C=CH_2 \quad \rightarrow \quad -CH_2-CH_2-CH_2\cdot$$

Addition polymerisation is just one of many types of polymerisation techniques, and the number of different monomers is theoretically infinite.

A given polymer may have a number of mechanical properties, originating from its molecular constituents. Density, stiffness, hardness, and durability, just to name a very few. Almost all properties depend upon the (average) length of the polymer chains, and a wide range of properties may be realised by varying the chain length, or by mixing different polymers.

Mixing of polymers is done in many ways. The crude way is to blend two different polymers, which allows only a limited room for optimisation, mostly

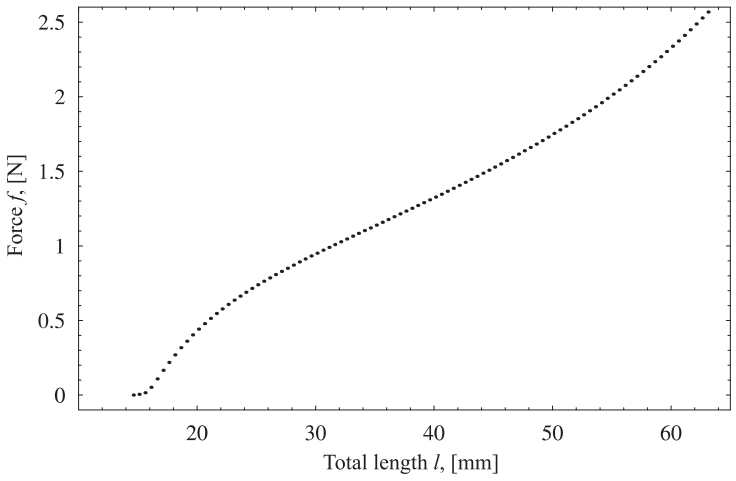

Figure 2.1: Measurement of the force-length relationship for a piece of regular, thin rubber band. The original length of the rubber band was 15.7 mm. The experimental procedure is presented in detail in chapter 5.

because polymers generally do not mix. Alternatively, the monomers can be blended before polymerisation, resulting in two different types of *copolymer*: random copolymers and block copolymers. Block copolymers give rise to very interesting system properties; sometimes the blocks are not miscible, forcing the system to phase-separate. Since the blocks are tied together in the polymer chain, they can only separate in certain, often highly fascinating configurations. Finally, it is possible to chemically attach molecules to the polymer chain, a process known as *grafting*. Grafted molecules may add completely new properties to a polymer.

When polymers are subject to pressure, they often comply by flowing, just like a liquid, but with much higher viscosity. When the polymer chains are very long, they will tend to be entangled, thus giving rise to a mixture of viscous and elastic behaviour, known as *visco-elasticity* [29, 30]. A description of a mechanical experiment on a polymer therefore must include the 'history' of the sample, making most properties time-dependent. Mechanical energy storage and loss signify visco-elastic behaviour.

Molecules capable of performing two grafting processes exist. Such mo-

lecules are used to bind two different polymer chains together, in a process known as *cross-linking*. When all polymer chains are linked together, they can not flow past each other. Such a cross-linked polymer is known as an *elastomer*. Elastomers have very little mechanical loss, and are capable of sustaining very high stretches. Therefore it is possible to derive a time-independent model, relating the stretching and the force of the elastomer.

The derivation is illustrated by referring to a simple experiment in which a piece of rubber band was stretched, while the corresponding force was measured. The piece of rubber under investigation was $x_2' = 1.22$ mm and $x_3' = 1.33$ mm on the sides, and $l_0 = 15.7$ mm (the notation is adapted from that used in appendix A). It was mounted between a force transducer and a translation stage, such that both extension and force could be monitored. The data are plotted in figure 2.1, only 1 in 50 points have been plotted for clarity. The data show a small plateau in the beginning of the data curve, which is present because the measurement was started with slack in the rubber band.

2.2 Hooke model

The Hooke model (also known as the spring model) is the simplest model for describing the length change of a piece of rubber in response to an external force. The model is linear, predicting that the force f on the ends of the sample is proportional to the change in length, Δl. This is sketched in figure 2.2(a). The mathematical representation of this behaviour is

$$f = k(l - l_0) = k\Delta l \qquad l > l_0 \tag{2.1}$$

where k is the spring constant, which is specific for a given sample.

A model describing the relation between force and length is inconvenient, as it depends on both sample material and geometry. In order to compare elastic properties between two different materials, it is necessary to remove any reference to the actual sample geometry on which the property was measured. The necessity of this is illustrated in the following.

Stretching the rubber piece in figure 2.2(b) (bottom) demands a force $f = k_1(l - l_0)$, which is the same throughout the rubber. The end of the rubber piece has travelled from l_0 to l. The point originally at $l_0/2$ has travelled to $l/2$, while delivering a force $f = k_2(l/2 - l_0/2)$, which must be the same as the previous. For the forces to be equal, $k_2 = 2\,k_1$, that is, the force constant of the shorter rubber band is twice that of the longer, even though they are made

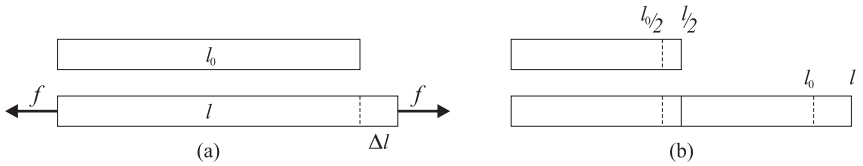

Figure 2.2: Stretching of rubber. (a) When a force f is applied to a string of rubber, it stretches from l_0 to l. (b) When the original length of the rubber is halved, the force constant is doubled.

from exactly the same material. A quantity, which describes the elastic properties of a material, yet is independent of sample geometry, is necessary for comparison of properties between materials. The concept of force constant as expressed in equation 2.1 is thus inappropriate, but introducing the concepts of stress and strain refines the model.

Introducing the extension ratio $\alpha = l/l_0$ (in the following, both 'extension ratio' and 'stretch ratio' refer to α), and the strain $\varepsilon = \alpha - 1$, the Hooke force is written as

$$f = kl_0(\alpha - 1) = kl_0\varepsilon$$

The stress is defined as

$$\sigma \equiv \frac{f}{A} \tag{2.2}$$

where $A = x_2x_3$ is the actual cross-sectional area of the rubber band during deformation. In order to remedy the shortcomings of the force constant, a specifically material dependent, geometry independent property, the tensile modulus, E, is defined as the slope at the very beginning of the stress-strain curve,

$$\frac{\partial\sigma}{\partial\varepsilon} \to E \qquad \text{for} \qquad \varepsilon \to 0 \tag{2.3}$$

The rubber deforms *uni-axially* (see figure 2.3), such that the only changes in geometry are along the axes of the rubber slab, thus the slab stays non-skewed. This is a circumstantial way of saying that the deformation must be without shear. The volume of the rubber is constant during deformation,

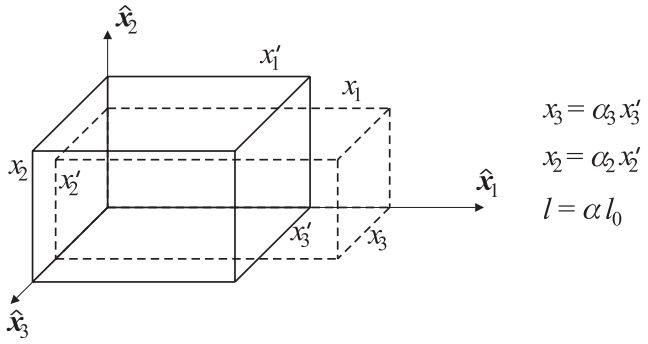

Figure 2.3: A sketch of the deformations that a piece of rubber undergo during uniaxial extension. While the rubber expands along $\hat{\boldsymbol{x}}_1$, it contracts equally along directions $\hat{\boldsymbol{x}}_2$ and $\hat{\boldsymbol{x}}_3$.

and the rubber deforms with rotational symmetry. This means that the strains along the $\hat{\boldsymbol{x}}_2$ and $\hat{\boldsymbol{x}}_3$ directions are equal, see figure 2.3.

The initial volume of the rubber band is $V' = l_0 x_2' x_3'$, while the final volume is written as $V = l x_1 x_2$, where $x_2 = \alpha_2 x_2'$ and $x_3 = \alpha_3 x_3'$. Since the deformation is rotationally symmetric perpendicularly to the extensional direction, $\alpha_2 = \alpha_3$. Using the incompressibility constraint,

$$V = V' \quad \Leftrightarrow \quad l_0 x_2' x_3' = l x_2 x_3 \quad \Leftrightarrow \quad 1 = \frac{l x_2 x_3}{l_0 x_2' x_3'} = \alpha_2^2 \alpha \quad \Rightarrow \quad \alpha_2 = \frac{1}{\sqrt{\alpha}}$$

The cross sectional area changes with the deformation as

$$A = x_2 x_3 = x_2' x_3' \alpha_2^2 = x_2' x_3' / \alpha = A_0 / \alpha$$

Collecting the above for the Hooke model, an equation for the stress is obtained

$$\sigma = \frac{f}{A} = \frac{f\alpha}{A_0} = \frac{k l_0 \varepsilon \alpha}{A_0} = \frac{k l_0}{A_0}(\varepsilon^2 + \varepsilon) = \frac{k l_0}{A_0}(\alpha^2 - \alpha)$$

Using the definition of the tensile modulus, equation 2.3,

$$\frac{\partial}{\partial \varepsilon} \frac{k l_0}{A_0}(\varepsilon^2 + \varepsilon) = \frac{k l_0}{A_0}(2\varepsilon + 1) \to \frac{k l_0}{A_0} \quad \text{for} \quad \varepsilon \to 0 \quad \Rightarrow \quad E = \frac{k l_0}{A_0}$$

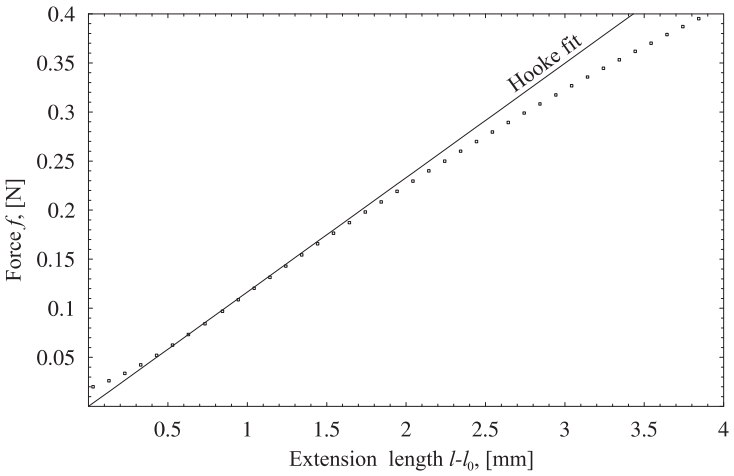

Figure 2.4: A fit of the Hooke model to the data of figure 2.1. The straight line represents the fit. A good fit is only possible for the first 1.5 mm, which is equal to a strain of 10%.

The Hooke model returns an estimate of the tensile modulus of $E = kl_0/A_0$. In practice this means that the tensile modulus can be retrieved from a force-extension measurement, if the original length and the original cross-sectional area are measured, and the force constant in limit of low strain is determined.

A fit was performed using the standard fitting routine `Fit`[*data*] in Mathematica© 3.0. The fit-expression was $\{1, \mathtt{e}\}$, returning a two parameter linear fit, $y = a + b \cdot x$, to the experimental data. The constant part of the fit was minimised, while a maximum in the proportional part was sought. The maximising of the proportional part of the fit is based on inspection of the data compared to the model: the largest slope is obtained at the beginning of the data curve, but there is a small region in which other factors, such as slack, plays a role. The fit strategy aims at disregarding the initial region of slack, and including only the linear region in the data. By inspection of the fit curve, figure 2.4, it is seen that the data are fit properly only for the first 1.5 mm of the curve, up to about 10% strain. For the data and fit in figure 2.4 a value of $k = 116$ N/m is extracted, returning a tensile modulus of $E = kl_0/(x_2' x_3') = 1.13$ MPa.

2.3 Neo-Hookean model

The simplest equation describing the relation between stress and strain for an elastic body is the Neo-Hookean equation [31], which assumes that the stress is proportional to the strain,

$$\sigma_{ij} = GB_{ij} \tag{2.4}$$

G is the elastic shear modulus, σ_{ij} is the stress tensor, and B_{ij} is the Finger (strain) tensor[1]. The Neo-Hookean model is an extension from one dimension to three dimensions of the stress response of an elastic body. The Neo-Hookean model is linear, but a linear relation between stress and strain is used in replacement of the linear relation between force and extension of the Hooke model.

The total stress corresponding to equation 2.4 is

$$T_{ij} = -p\,\delta_{ij} + GB_{ij} \tag{2.5}$$

where δ_{ij} is the identity matrix, and the Finger tensor is (see appendix A),

$$B_{ij} = \begin{bmatrix} \alpha_1^2 & 0 & 0 \\ 0 & \alpha_1^{-1} & 0 \\ 0 & 0 & \alpha_1^{-1} \end{bmatrix}$$

The boundary conditions determine p for any problem.

The stress-strain relation for the Neo-Hookean model is calculated for the uni-axial strain situation. The total stress components on the elastomer are

$$T_{11} = -p + G\alpha_1^2 \qquad T_{22} = T_{33} = -p + \frac{G}{\alpha_1}$$

Since the sides of the elastomer string are free to find an equilibrium position, the total stress in these directions must be zero. In direction of $\hat{\boldsymbol{x}}_2$,

$$T_{22} = 0 = \sigma_{22} - p \quad \Rightarrow \quad p = \sigma_{22}$$

When the value of p is known, the total stress in direction of $\hat{\boldsymbol{x}}_1$ becomes

$$T_{11} = \sigma_{11} - \sigma_{22} = G\alpha_1^2 - G\frac{1}{\alpha_1} = G\left(\alpha_1^2 - \frac{1}{\alpha_1}\right)$$

[1] For the basics on tensor notation in elasticity theory, see appendix A, which includes an account of the Finger tensor, section A.3.

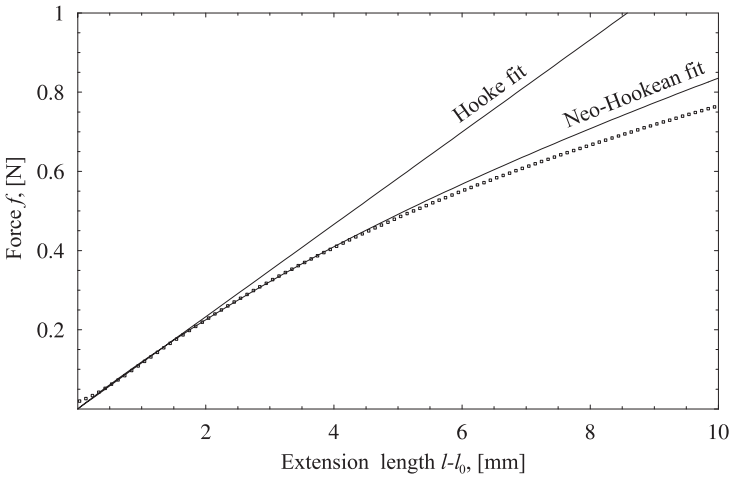

Figure 2.5: A fit of the Neo-Hookean model to the data of figure 2.1. The curved full line represents the Neo-Hookean fit, while the straight line is the Hooke model fit. A good fit now extends for the first 5 mm, which is equal to a strain of 33%, a good improvement over the Hooke model.

The force measured on the ends of the elastomer is found by multiplying the total stress on the ends with the area

$$\begin{aligned} a_1 &= x_2 x_3 = x_2' x_3' \alpha_1^{-1} \\ f_1 &= T_{11} a_1 = x_2' x_3' G \left(\alpha_1 - \frac{1}{\alpha_1^2} \right) \end{aligned} \tag{2.6}$$

where the *original* dimensions of the elastomer are x_2' and x_3'.

The tensile modulus is calculated from the definition, equation 2.3,

$$\frac{\partial}{\partial \varepsilon} \left[G \left(\alpha_1 - \frac{1}{\alpha_1^2} \right) \right] \to 3G \quad \text{for} \quad \varepsilon \to 0 \qquad \Rightarrow \qquad E = 3G$$

where $\varepsilon = \alpha_1 - 1$ was used.

With this model, a better fit of the data in figure 2.1 is obtained. Again the fitting routine `Fit`[*data*] is employed, but now the fit-expression is $\{1 + \mathtt{e} -$

$(1+\mathrm{e})^{-2}\}$, which returns the pre-factor of equation 2.6, $x_2' x_3' G$. Note that this is a one-parameter fit, only the value of G is fitted. The resulting fit is shown in figure 2.5, together with the previous Hooke model fit. Here a good fit continues up to around 5 mm, corresponding to about 33% strain. The tensile modulus obtained from this fit is $E = 3G = 1.22$ MPa. This value is 10 % higher than the value obtained from the Hooke model.

2.4 Mooney-Rivlin model

An even better description of the stress-strain properties of an elastomer derives from a strain energy minimisation analysis. The strain energy, ϕ, is constructed as a suitable function of the invariants of the strain tensor [32] (for invariants, see section A)

$$\begin{aligned} I_1^B &= \alpha_1^2 + \alpha_2^2 + \alpha_3^2 \qquad I_2^B = \frac{1}{\alpha_1^2} + \frac{1}{\alpha_2^2} + \frac{1}{\alpha_3^2} \\ \phi &= C_1(I_1^B - 3) + C_2(I_2^B - 3) \end{aligned}$$

The stress is then obtained as the derivative of the energy function with respect to the extension ratio,

$$\begin{aligned} T_{ii} &= \alpha_i \frac{\partial \phi}{\partial \alpha_i} - p \\ &= \alpha_i \left(C_1 2\alpha_i + C_2 \cdot (-2) \frac{1}{\alpha_i^3} \right) - p \\ &= 2C_1\alpha_i^2 + 2C_2 \frac{1}{\alpha_i^2} - p \end{aligned} \tag{2.7}$$

for the Mooney-Rivlin strain energy function. This result can be written in tensor notation using

$$\begin{aligned} \mathbf{T} &= -p\,\mathbf{I} + 2C_1\mathbf{B} + 2C_2\mathbf{B}^{-1} \\ T_{ij} &= -p\,\delta_{ij} + 2C_1 B_{ij} + 2C_2 B_{ij}^{-1} \end{aligned} \tag{2.8}$$

for the incompressible case. The Neo-Hookean model is obtained when $C_2 = 0$ and $2C_1 = G$. The Neo-Hookean model is obviously a one-parameter model, while the Mooney-Rivlin model contains two parameters.

Now uni-axial extension is evaluated for the Mooney-Rivlin model. The Finger tensor for uni-axial extension was written above, and the inverse of the Finger tensor is

$$(B_{ij})^{-1} = \begin{bmatrix} \alpha_1^{-2} & 0 & 0 \\ 0 & \alpha_1 & 0 \\ 0 & 0 & \alpha_1 \end{bmatrix}$$

Inserting the tensors in equation 2.8, the elements of the stress tensor become

$$T_{11} = -p + 2C_1\alpha_1^2 + 2C_2\alpha_1^{-2} \qquad T_{22} = T_{33} = -p + 2C_1\alpha_1^{-1} + 2C_2\alpha_1$$

With boundary conditions like in the previous section, the result for the total stress on the ends of the rubber string is

$$\begin{aligned} T_{11} &= \sigma_{11} - \sigma_{22} \\ &= 2C_1\alpha_1^2 + 2C_2\alpha_1^{-2} - (2C_1\alpha_1^{-1} + 2C_2\alpha_1) \\ &= 2C_1\left(\alpha_1^2 - \frac{1}{\alpha_1}\right) - \frac{2C_2}{\alpha_1}\left(\alpha_1^2 - \frac{1}{\alpha_1}\right) \\ &= \left(2C_1 - \frac{2C_2}{\alpha_1}\right)\left(\alpha_1^2 - \frac{1}{\alpha_1}\right) \end{aligned} \tag{2.9}$$

and the force on the ends of the sample is

$$f_1 = x_2' x_3' \left(2C_1 - \frac{2C_2}{\alpha_1}\right)\left(\alpha_1 - \frac{1}{\alpha_1^2}\right) \tag{2.10}$$

The tensile modulus, E, is evaluated using the definition, equation 2.3, on equation 2.9,

$$\frac{\partial}{\partial\varepsilon}\left[\left(2C_1 - \frac{2C_2}{\alpha_1}\right)\left(\alpha_1^2 - \frac{1}{\alpha_1}\right)\right] \to 3(2C_1 - 2C_2) \quad \text{for} \quad \varepsilon \to 0$$

The model was fitted to the data of figure 2.1. Equation 2.9 was expanded, such that each fitting term (C_1, C_2) was fitted separately. This was mediated by running `Fit`[*data*] with the fit-expression $\{(1+\mathtt{e}-(1+\mathtt{e})^{-2}), (1-(1+\mathtt{e})^{-3})\}$. The fit then returns (C_1, C_2) as the coefficients for the best fit. With this expression it was possible to fit the data for the first 150 % of the stress-strain curve, as shown in figure 2.6. The result of the fit was $C_1 = 133\,\text{kPa}$, $C_2 = -87.3\,\text{kPa}$, and $E = 3(2C_1 - 2C_2) = 1.32\,\text{MPa}$.

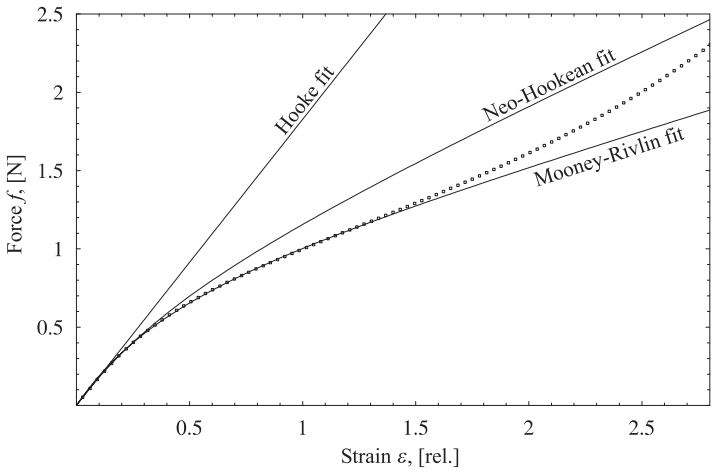

Figure 2.6: Fit of the Mooney-Rivlin equation (equation 2.10) to the data of figure 2.1. Now the strain is used as the independent variable, instead of the length. The previously presented fits are included for comparison. With the Mooney-Rivlin equation, a good fit is obtained up to 150% strain.

2.5 Ogden model

Inspection of figure 2.6 reveals that the Mooney-Rivlin fit does not describe the whole region. This is because it does not follow the up-turn in the data from 150% strain and upwards. The up-turn behaviour is sometimes referred to as strain-hardening. The fitting regime is extended through a theory introduced by Ogden [32]. Similarly to Mooney and Rivlin, a stress-strain relation is obtained through evaluation of the strain-energy function.

The strain is redefined to

$$\varepsilon_i = \frac{\alpha_i^k - 1}{k} \qquad k \neq 0$$

where k can be any real number, different from zero. Notice how the strain does not depend linearly upon the extension ratio, α. The invariant of the new strain tensor can be written as

$$\phi(k) = \frac{\alpha_1^k + \alpha_2^k + \alpha_3^k - 3}{k}$$

The former invariants I_1^B and I_2^B are linked to the new invariant through

$$\phi(2) = \frac{1}{2}(I_1^B - 3) \qquad \phi(-2) = -\frac{1}{2}(I_2^B - 3)$$

Ogden proposed a strain energy function, which is a linear combination of the invariants $\phi(k)$,

$$\phi = \mu_l \phi(k_l)$$

The index l runs over the number of terms. Since it is only possible to find three linearly independent invariants, no more than three terms should be used. The stress is derived by evaluating equation 2.7 for the above definition of the strain energy,

$$T_{ij} = \mu_l \alpha_i^{k_l} - p$$

with an implicit sum over the number of included terms.

Again, the uni-axial extension experiment is considered. It is recalled that due to the incomressibility constraint, the values of the extension ratios are $\alpha_2 = \alpha_3 = 1/\sqrt{\alpha_1}$. Using the boundary condition for uni-axial extension, the formulas for the strain and force are

$$\begin{aligned} T_{11} &= \mu_l \left(\alpha_1^{k_l} - \alpha_1^{-\frac{1}{2}k_l} \right) \\ f_1 &= x_2' x_3' \mu_l \left(\alpha_1^{k_l - 1} - \alpha_1^{-1-\frac{1}{2}k_l} \right) \end{aligned} \tag{2.11}$$

Again, summation over the necessary number of terms l is implicit.

The force-extension data of the rubber string are treated once more. A two-term expression is used ($l = \{1, 2\}$), explicitly

$$f_1 = x_2' x_3' \left[\mu_1 \left(\alpha_1^{k_1 - 1} - \alpha_1^{-1-\frac{1}{2}k_1} \right) + \mu_2 \left(\alpha_1^{k_2 - 1} - \alpha_1^{-1-\frac{1}{2}k_2} \right) \right]$$

As the value of exponents k_l can be any real number, the routine `Fit[`*data*`]` can no longer be used. Still, Mathematica®3.0 is up to the job. A non-linear fit is performed using the routine `NonLinearFit[`*data*`]`, or its equivalent `NonLinearRegress[`*data*`]`, which outputs a regression analysis when the fit procedure is completed. All four variables (μ_1, μ_2, k_1, k_2) can be fitted simultaneously with this routine.

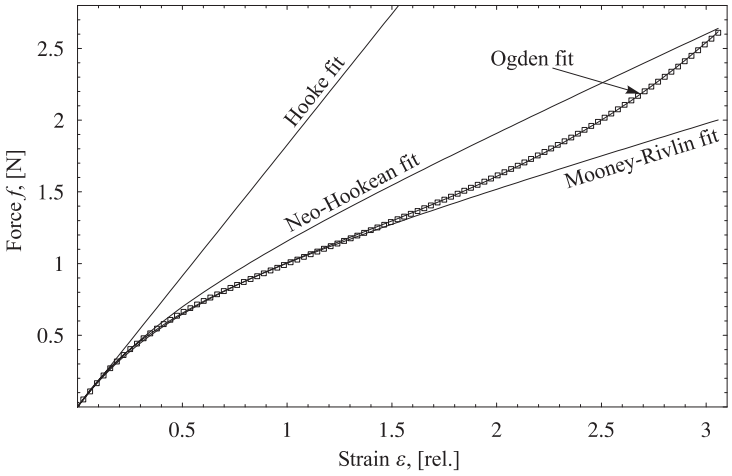

Figure 2.7: Fit of a two-term Ogden model to the rubber string force-extension data. The fit now extends throughout the whole range of the strain. Ogden used a three-term model to fit an experiment with a maximum strain of 750% [32].

A set of seed data (μ_1, μ_2, k_1, k_2) for the fit is defined. Then the routine is run, while k_1 is kept constant. In the second step, k_1 is free and μ_1 is fixed. Bouncing back and forth between having k_1 or μ_1 fixed, lets the set of parameters converge quickly towards a good fit. The result of this fitting procedure is plotted in figure 2.7, where also the previous fit curves are included. The resulting fit parameters are

$$\begin{array}{ll} \mu_1 = 745\ \text{kPa} & k_1 = 1.101 \\ \mu_2 = 6.90\ \text{kPa} & k_2 = 4.42 \end{array} \qquad E = 1.70\ \text{MPa}$$

The fit values of the tensile modulus presented in table 2.1 are not equal. There are two reasons for this, and they work in opposite directions. The models are fitted to different parts of the experimental data. The fit of the Hooke model only uses the first 13% of the strain region, where the sample seems stiffer, because the force grows more rapidly. This should yield a *higher* value of the tensile modulus than for the more advanced models. The second reason is that the mathematical structure of the more advanced models includes negative components. Therefore a higher value of the tensile modulus results.

Model	Stress	Tensile modulus	Fit value
Hooke	$\frac{kl_0}{A_0}(\varepsilon^2+\varepsilon)$	$\frac{kl_0}{A_0}$	1.13 MPa
Neo-Hookean	$G\left(\alpha^2-\frac{1}{\alpha}\right)$	$3G$	1.22 MPa
Mooney-Rivlin	$\left(2C_1-\frac{2C_2}{\alpha}\right)\left(\alpha^2-\frac{1}{\alpha}\right)$	$3(2C_1-2C_2)$	1.32 MPa
Ogden	$\mu_l\left(\alpha^{k_l}-\alpha^{-k_l}\right)$	$\mu_l k_l$	1.70 MPa

Table 2.1: Fit results for the four presented models of stress-strain behaviour.

When reporting a value of the tensile modulus, it is therefore important to include its definition. And this is also what is done for all rheological values obtained and presented in articles, where explicit emphasis is put on the experimental procedure by which the value was obtained. Usually, the value of the tensile modulus is obtained from the Hooke model which itself is defined as the limiting slope of the stress-strain curve for small strains, as in the definition of the tensile modulus.

2.5.1 Constrained movement

Up to now, only the case with no constraints on the directions perpendicular to the pulling direction was considered. A different situation is outlined in figure 2.8, applying to an elastomer film. In the direction perpendicular to the film plane the dimension is much thinner than the length of the sample. The width of the sample on the other hand is larger than both the length and the thickness of the film. Therefore the strain response is different in the two directions perpendicular to the pulling direction. This is illustrated left in figure 2.8, with an extension ratio of $\alpha_1 = \frac{5}{3}$. The sample contracts in thickness, $\alpha_3 = 1/\alpha_1$, while the width of the sample remains constant, $\alpha_2 = 1$. The deformation tensors describing this deformation are

$$w_{ij} = \begin{bmatrix} \alpha_1 & 0 & 0 \\ 0 & 1 & 0 \\ 0 & 0 & \frac{1}{\alpha_1} \end{bmatrix} \qquad B_{ij} = \begin{bmatrix} \alpha_1^2 & 0 & 0 \\ 0 & 1 & 0 \\ 0 & 0 & \frac{1}{\alpha_1^2} \end{bmatrix} \tag{2.12}$$

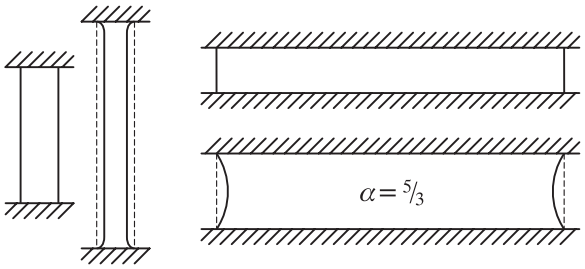

Figure 2.8: Justification of assumptions regarding constrained movement. A piece of elastic film is stretched with an extension ratio of $5/3$. The thin dimension is much lower than the length; therefore it is allowed to shrink. The wide dimension is constrained from shrinking; therefore the strain in this direction is zero.

The boundary conditions are altered, now the film is free only in the direction of $\hat{\boldsymbol{x}}_3$. Still, it is possible to obtain a value for p, since

$$\begin{aligned} & T_{33} = \sigma_{33} - p = 0 \quad \Leftrightarrow \quad p = \sigma_{33} \\ \Rightarrow \quad & T_{11} = \sigma_{11} - \sigma_{33} \end{aligned}$$

The stress and force are calculated for the Neo-Hookean model, equation 2.5,

$$\begin{aligned} T_{11} &= G(B_{11} - B_{33}) = G(\alpha_1^2 - \alpha_1^{-2}) \\ f_1 &= x_2' x_3' G(\alpha_1 - \alpha_1^{-3}) \\ E &= 4G \end{aligned} \tag{2.13}$$

The tensile modulus increases by one third compared to the non-constrained experiment (for which the tensile modulus was $E = 3G$). Simply put, a constrained film is stiffer than the corresponding film free of constraints, even though they are made from the same material.

For the Mooney-Rivlin model, equation 2.8, the results are

$$\begin{aligned} T_{11} &= \sigma_{11} - \sigma_{33} = (2C_1 - 2C_2)(\alpha_1^2 - \alpha_1^{-2}) \\ f_1 &= x_2' x_3' (2C_1 - 2C_2)(\alpha_1 - \alpha_1^{-3}) \\ E &= 4(2C_1 - 2C_2) \end{aligned} \tag{2.14}$$

The Neo-Hookean and the Mooney-Rivlin models return the same prediction for the stress-strain behaviour of a constrained elastomer film, when $G = 3(2C_1 - 2C_2)$. Again the tensile modulus grows by one third.

Finally, for the Ogden model, the results are

$$\begin{aligned} T_{11} &= \sigma_{11} - \sigma_{33} = \mu_l \left(\alpha_1^{k_l} - \alpha_1^{-k_l} \right) \\ f_1 &= x_2^l x_3^l \mu_l \left(\alpha_1^{k_l - 1} - \alpha_1^{-(1+k_l)} \right) \\ E &= 2\mu_l k_l \qquad (\text{sum over } l) \end{aligned} \tag{2.15}$$

For the Ogden model, the tensile modulus is doubled by the introduction of the width constraint.

3

Dielectricity and electrostriction

The polarisation of molecular dipoles stores energy in the dielectric medium. This electrostatic energy can be converted to mechanical energy (strain, stress) through a number of mechanisms, the simplest being through the Maxwell stress, which all materials exhibit. Further mechanisms include electrostriction and piezoelectricity, but only certain classes of dielectric material have these properties. In the following these phenomena are presented.

3.1 Dielectricity

All materials become polarised when exposed to an electric field. However, the exact response of a certain material to an applied electric field is quite hard to predict. If the material is conducting, the electric field will give rise to charge transport, due to which the effects of polarisation will be obscured. The remainder of this chapter considers insulating, non-conductive materials.

3.1.1 The dielectric constant

A typical model of an insulating material regards the material as composed of small dipoles, which are electrically neutral, but possess internal charge separation. When exposed to an external electric field, the tendency of a single dipole is to align itself with the electric field, such that the positive end points toward lower potential, and the negative end points toward the higher potential [33]. When all the dipoles in a material align in this way to an applied electric field, the material is known as a *dielectric*.

Figure 3.1(a) depicts the situation when a constant voltage is applied to a set of juxtaposing capacitor plates. Electric field lines may only begin on free positive charges, and end on free negative charges. Thus, surface charge concentration builds up on the capacitor plates. The charge build up continues, until the voltage drop over the capacitor plates matches that of the voltage source. The relation between the amount of free charge, Q, and the voltage

drop, V, is $Q = CV$, where C is the capacitance of the capacitor,

$$C = \frac{\epsilon_0 A}{d}$$

A is the area of the plates, and d is the distance between them. ϵ_0 is the vacuum permittivity, $\epsilon_0 = 8.854 \cdot 10^{-12}$ F/m. The density of the field lines is known as the electric flux density, or just flux density, and is given by

$$D_i = \epsilon_0 E_i$$

where E_i are the components of the electric field between the capacitor plates.

If a piece of dielectric material is inserted between the plates, figure 3.1(b), the dipoles in the material will reorient such that the positive end of the dipole points toward the negative potential. Even though no free charges have been created in the material, the reorientation of the dipoles exposes a net 'bound' charge on the surface of the dielectric, and in fact a current will flow from the battery to keep the voltage over the plates constant.

The flux density in the material has increased, and is now

$$D_i = \epsilon E_i$$

where ϵ is the dielectric constant of the material. This equation implies that the actual electric field in the material is the same as when no material is placed

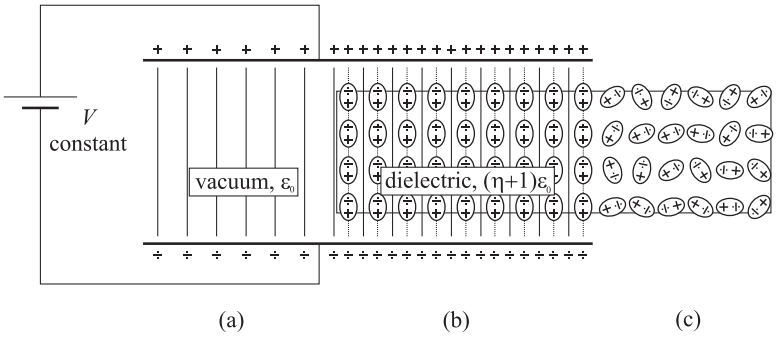

Figure 3.1: Dielectric susceptibility. (a) vacuum capacitor, (b) polarised dipoles in the dielectric inserted between the capacitor plates, (c) random dipoles when no electric field is applied.

between the capacitor plates, only the flux density D_i has changed. The flux density is also known as the electric displacement, because it is a measure of the displacement of the dipoles in the material. The relative dielectric constant is then defined as the ratio between the flux density in vacuum and in the dielectric,

$$\epsilon_r = \frac{\epsilon}{\epsilon_0}$$

Part of the electric displacement originates from the vacuum displacement, the other part from actual polarisation of the dielectric. The electric polarisation is the flux density originating solely from the polarised material

$$P_i = D_i - \epsilon_0 E_i$$

and the electric susceptibility is the part of the relative dielectric constant caused by the material,

$$\eta = \epsilon_r - 1 \qquad \Rightarrow \qquad P_i = \epsilon_0 \eta E_i$$

In this thesis, ϵ_r is referred to as just the dielectric constant, because reference is never made to the actual dielectric constant ϵ. In general, the dielectric constant is a complex parameter, so by definition the complex dielectric constant is

$$\overline{\epsilon} = \epsilon' - i\,\epsilon''$$

where $i = \sqrt{-1}$.

3.1.2 Time-dependent fields

The complex frequency response of the lumped-circuit components (resistors, R, capacitors, C, and inductors, L) is derived from basic principles. The relation between the charge on a capacitor and the voltage drop over it is

$$Q = CV \tag{3.1}$$

The current is considered positive if it flows from the positively charged plate,

$$I = -\frac{dQ}{dt}$$

If equation 3.1 is differentiated with respect to time, the following relation between the voltage and the current is obtained,

$$\frac{dQ}{dt} = \frac{d(CV)}{dt} = C\frac{dV}{dt} \quad \Leftrightarrow \quad I = -C\frac{dV}{dt}$$

if the capacitance is constant. When an alternating voltage is applied, $\overline{V}(t) = V_0 \exp(-i\omega t)$, the resulting alternating current is

$$\overline{I} = -C\frac{d(V_0 \exp(-i\omega t))}{dt} = i\omega C V_0 \exp(-i\omega t) = i\omega C\overline{V}$$

from which the impedance is extracted as

$$\overline{Z} = \frac{\overline{V}}{\overline{I}} = \frac{1}{i\omega C}$$

where $\overline{Z} = \overline{V}/\overline{I}$ is the complex version of Ohm's Law.

The impedance of an inductor is calculated using Lenz' Law, stating that when the flux through a coil changes, a voltage arises in order to keep the flux constant,

$$V = -\frac{d\Phi}{dt} = -\frac{d(LI)}{dt} = -L\frac{dI}{dt}$$

where the relation $\Phi = LI$ is inserted, L being the inductance of the inductor. Inserting the oscillating voltage from before, the equation can be solved by separation of variables,

$$\int V_0 \exp(-i\omega t)\, dt = -L \int dI$$

$$\Leftrightarrow \quad V\frac{1}{-i\omega} = -LI \quad \Rightarrow \quad \overline{Z}_L = i\omega L$$

Component	Frequency response (impedance, $\overline{Z}$)	
	Real	Imaginary
Resistor	R	
Capacitor		$1/iC\omega$
Inductor		$iL\omega$

The frequency response of these components can be plotted in an impedance spectrum, in which both axes are logarithmic. The technique by which these spectra are obtained, is known as *dielectric spectroscopy*.

3.1.3 Dielectric spectroscopy

The features of a dielectric spectrum reveal basic physical properties of a material. Whether the material behaves as a simple resistor or capacitor, or specific molecular relaxations or ionic conductivity takes place, can be determined from the dielectric spectrum. If also the temperature is varied, knowledge on the interaction between molecular dipoles can be extracted. It is therefore important to determine whether features in the dielectric spectrum originate from lumped-circuit behaviour, or if an explanation of the spectrum must include molecular relaxations and conduction in the material.

The real part of the impedance spectrum of an ideal resistor is constant, R, and the spectrum has a zero imaginary part. The response of the capacitor has no real part. The imaginary part is $Z_C'' = 1/C\omega$, which in a log-log plot becomes a straight line with slope -1,

$$\log Z_C'' = \log \frac{1}{C\omega} = -\log C - \log \omega$$

which intercepts $-\log C$ for $\omega = 1$. For the inductor, the slope is 1, since

$$\log Z_L'' = (\log L\omega) = \log L + \log \omega$$

The inductor component is only useful for description of samples with magnetic properties, and therefore demands no further consideration in this thesis.

With these components as building blocks, it is possible to construct more complex dielectric spectra, as for instance a circuit consisting of a resistor and

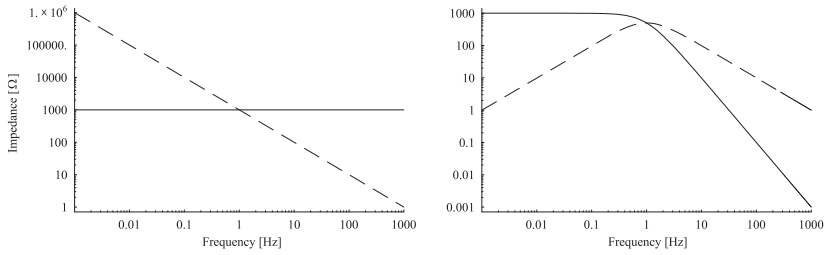

Figure 3.2: Impedance spectra of serial (left) and parallel circuits of a resistor and a capacitor. The resistance is $R = 1$ kΩ, and the capacitance is $C = 1$ mF. The real part is plotted as the full curve, the imaginary part as the dashed.

a capacitor in series. The frequency dependent impedance of this circuit is

$$\overline{Z} = Z_R + Z_C = R + \frac{1}{iC\omega}$$

as impedances are added when in series. With this impedance, a more realistic dielectric spectrum with both a real and an imaginary part, is obtained. The left part of figure 3.2 is a plot of the impedance of a parallel circuit, with a capacitance of $C = 1$ mF, and a resistance of $R = 1$ kΩ. The real part of the spectrum has a constant value, while the imaginary part is a straight line with slope -1, as predicted above.

An impedance spectrum with more features is obtained when the two components are added in parallel, rightmost in figure 3.2. The impedances in parallel are added reciprocally,

$$\frac{1}{\overline{Z}} = \frac{1}{Z_R} + \frac{1}{Z_C} \quad \Leftrightarrow \quad \overline{Z} = \frac{R}{1 + R^2C^2\omega^2} - i\frac{R^2C\omega}{1 + R^2C^2\omega^2}$$

The real part is constant until a certain frequency $\omega \equiv 1/\tau$, after which it drops off with slope -1. The imaginary part goes through a maximum for $\omega = 1/\tau$. With $\tau = RC$, the above equation for the impedance is re-cast,

$$\overline{Z} = R\left(\frac{1}{1 + (\omega\tau)^2} - i\frac{\omega\tau}{1 + (\omega\tau)^2}\right) = \frac{R}{1 + i\omega\tau}$$

by which it can be seen that a characteristic frequency must lie at $1/\tau$.

The relation between the properties of a macroscopic capacitor and the properties of the dielectric between the capacitor plates is

$$\overline{C} = \frac{\overline{\epsilon}_r \epsilon_0 A}{d}$$

where A is the surface area of the capacitor, and d is the distance between the plates. This simple equation is used for the computation of the dielectric spectrum.

The dielectric in the capacitor affects the applied ac voltage, such that both the amplitude and the phase are changed. The dielectric analyser extracts the frequency dependent impedance from a comparison between the applied and the resultant voltage, see section 5.1. For the purpose of dielectric spectroscopy, the impedance is then converted to capacitance through the equations stated above, and finally divided by the vacuum capacitance of the cell,

$C_{\mathrm{vac}} = \epsilon_0 A/d$, to return the dielectric spectrum, formally written as

$$\overline{\epsilon}_r(\omega) = \frac{\overline{C}}{C_{\mathrm{vac}}} = \epsilon'(\omega) - i\,\epsilon''(\omega)$$

The corresponding conductivity spectrum is calculated directly from the dielectric spectrum using the relation

$$\overline{\sigma}(\omega) = \sigma'(\omega) - i\,\sigma''(\omega) = i\omega\,\epsilon_0(\overline{\epsilon}_r(\omega) - 1)$$

3.1.4 Dielectric relaxation

The dipoles in the dielectric need a certain time for aligning with the applied field. This time is known as the relaxation time, and it affects the dynamic response of the dielectric. One method for obtaining information about the relaxation is to monitor the response by the use of the dielectric analyser.

The simplest physical model of a dielectric material was introduced by Debye [33], for description of the dielectric relaxation properties of a gas. The presence of the gas changes the dielectric constant from that of the vacuum capacitor. In addition, the dipoles are able to respond to an alternating field by oscillating in phase with the field, but only if the field does not oscillate too rapidly. At low frequencies the real part of the dielectricity is high. At a frequency corresponding to the relaxation time, τ, it drops off to a lower level, because the dipoles are not able to follow the alternating field. The imaginary part is low in the whole frequency range, except in the region close to $1/\tau$ where the oscillations of the dipoles are imperfect with respect to alternating field, therefore they dissipate the energy stored in the electric field into heat.

These features are contained in the lumped-circuit model depicted in figure 3.3. The frequency dependent capacitance of this network is

$$\overline{C} = C_\infty + (i\omega R + \frac{1}{C_0 - C_\infty})^{-1}$$

which is rewritten to

$$\frac{\overline{C} - C_\infty}{C_0 - C_\infty} = \frac{1}{1 + i\omega R(C_0 - C_\infty)} \tag{3.2}$$

Defining the molecular relaxation time as $\tau = R(C_0 - C_\infty)$ and multiplying nominator and denominator with $d/\epsilon_0 A$, the Debye model becomes

$$\frac{\overline{\epsilon} - \epsilon(\infty)}{\epsilon(0) - \epsilon(\infty)} = \frac{1}{1 + i\omega\tau}$$

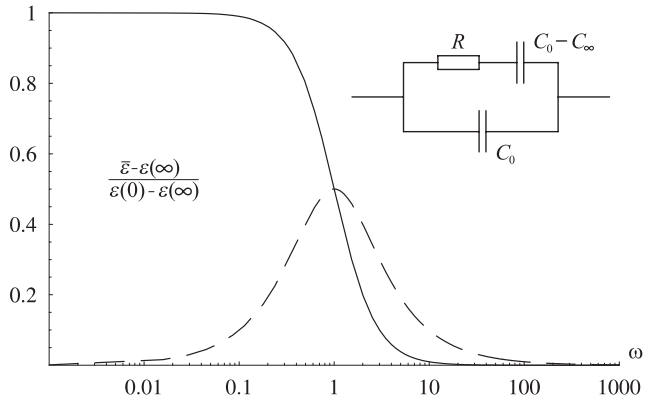

Figure 3.3: The dielectric spectrum of the Debye model in a log-linear plot. The corresponding electric circuit is sketched as well.

where $\epsilon(0)$ and $\epsilon(\infty)$ are the real parts of the dielectric constant at zero and infinite frequency, respectively (the imaginary part is zero at both zero and infinite frequencies). The relaxation time is strongly dependent upon temperature for almost any system.

The Debye model is basic to most of the attempts at modelling the more complex dielectric spectra, including those of polymers. One of the more general models is the Havriliak-Negami (H-N) function [34],

$$\frac{\overline{\epsilon} - \epsilon(0)}{\epsilon(\infty) - \epsilon(0)} = \frac{1}{(1 + (i\omega\tau)^{\alpha})^{\beta}}$$

where in general α, β, τ, $\epsilon(0)$, and $\epsilon(\infty)$ are fitting parameters. τ, α, and β are temperature dependent. For $\alpha = \beta = 1$ the Debye model is recovered. If several relaxations occur in the dielectric, the whole spectrum is fitted by adding further H-N elements. Most work in the field of dielectric spectroscopy deals with measuring the temperature dependence of the H-N parameters [34, 35].

3.1.5 Maxwell stress

The mechanical driving force of the dielectric elastomer actuator derives from Coulomb charge attraction. When a capacitor is charged by application of an

electric field, positive charges reside on one electrode, balanced by negative charges on the other electrode. The compliance of the elastomer allows the charges to move closer by squeezing the capacitor together. Volume conservation forces the elastomer to expand transversely to the electric field, increasing the area of the electrodes. This increase lets like charges on one electrode move further apart, lowering the internal energy of the charges. This is, in words, the principle behind the dielectric elastomer actuator. A more mathematical derivation follows, kept as simple as possible.

The capacitance of a capacitor, $C = \epsilon\epsilon_0 A/z$, dropping the subscript r on ϵ_r, and using z for the thickness of the capacitor. The energy density of the electric field is

$$u = \frac{1}{2}\,\mathbf{D}\cdot\mathbf{E} = \frac{1}{2}\,\epsilon\epsilon_0 E^2$$

where the last equality holds because **D** and **E** are in the same direction, as is the case in isotropic dielectrics. This expression is transformed by using $E = V/z$, yielding

$$U = u\,Az = \frac{1}{2}C\,V^2$$

the familiar expression for the energy stored in a capacitor.

The force between the electrodes is found from

$$f = -\frac{dU}{dz}$$

The differential of the energy is

$$dU = \frac{\epsilon\epsilon_0 V^2}{2}\,d\!\left(\frac{A}{z}\right) = \frac{\epsilon\epsilon_0 V^2}{2}\,\left(\frac{1}{z}\,dA - \frac{A}{z^2}\,dz\right)$$

when the voltage is constant. The differential of A/z is found by noting that the volume is constant during deformations,

$$\begin{aligned} d(Az) &= z\,dA + A\,dz = 0 \\ \Leftrightarrow \frac{dA}{A} &= -\frac{dz}{z} \end{aligned}$$

which is inserted in the above to yield

$$\begin{aligned} dU = -\frac{\epsilon\epsilon_0 V^2}{2}\,2\frac{A}{z^2}\,dz = \epsilon\epsilon_0 AE^2\,dz \\ \Leftrightarrow \quad f = -\frac{dU}{dz} = \epsilon\epsilon_0 AE^2 \end{aligned}$$

for the force between the electrodes. It is more useful to calculate the stress, by using the definition stated in equation 2.2,

$$\sigma = \frac{f}{A} = \epsilon\epsilon_0 E^2 \tag{3.3}$$

This equation was derived a century ago for the stress on the surface of a dielectric in an electric field [36], but with a prefactor of $\frac{1}{2}$. The doubling of the stress derived here, stems from the compliant electrodes.

The stress does not depend directly upon any geometrical factors. Because of this, a DEA can have any desired size, limited only by manufacturing and application constraints. The stress is proportional to the dielectric constant. The dielectric constant of dielectric elastomers is typically in the range of 2–8 ϵ_0. Materials with dielectric constants of $\sim 10,000\ \epsilon_0$ exist, these are typically crystalline and not applicable to DEA, except as filler material. To this author's knowledge, no accounts exist of a dielectric elastomer with filler used for DEA.

The stress depends upon the applied electric field to second order. Writing the electric field as $E = V/z$, it is seen that the thickness of the insulating elastic film *does* enter, and in fact the stress is inversely proportional to the square of the thickness. This opens two ways of increasing the stress: either by thinning the elastomer, or by increasing the voltage. The elastomer thickness in this thesis was limited downwards to about 25 μm; the thickness could probably be lowered, but that is not necessary for a proof of principle, since the voltage amplifier provides up to 10 kV. The voltage is limited upwards by the dielectric breakdown strength, a material specific constant. The dielectric breakdown strength depends upon material structure, the temperature, and on the presence of impurities.

3.2 Electrostriction

The original paper by Anderson [1], calculates the volume force density arising from an applied, uniform electric field. The starting point of the derivation is a thermodynamically derived, basic textbook expression [36], here given in the form used by Anderson,

$$\mathbf{F} = \rho_f \mathbf{E} - \frac{1}{2}\epsilon_0 E^2 \boldsymbol{\nabla}\epsilon + \frac{1}{2}\epsilon_0 \boldsymbol{\nabla}\left[E^2 \rho \frac{\partial \epsilon}{\partial \rho}\right]$$

where ρ_f is the density of free charges in the dielectric, and ρ is the mass density of the dielectric. The second term is the Maxwell stress term, derived in the previous section, and the third term is the electrostrictive term. It is seen that electrostriction explicitly arises from changes in the mass density of the material. In the derivation of the Maxwell stress presented above, it was assumed that the dielectric was incompressible. This assumption holds for liquids, and for the soft elastomers that are the subject of this thesis.

The strain arising from polarisation of the dielectric is more generally written as [37–39]

$$\varepsilon_{ij} = d_{ijk}E_k + \gamma_{ijkl}E_kE_l + \dots$$

where the coefficients explicitly depend upon strain through

$$d_{ijk} = \frac{\partial \varepsilon_{ij}}{\partial E_k} \qquad \gamma_{ijkl} = \frac{\partial^2 \varepsilon_{ij}}{\partial E_k \partial E_l}$$

The d_{ijk} are better known as the piezo-electric coefficients, and γ_{ijkl} are the electrostrictive coefficients. For isotropic dielectrics symmetry considerations show, [39], that the electrostrictive coefficient tensor reduces to just two independent components, γ_{1111} and γ_{1122}. Redefining these two components of the electrostrictive tensor, an expression for the dielectric tensors dependence upon strain is written as [16] (for small strains),

$$\epsilon_j = \epsilon^0\delta_{ij} + a_1\varepsilon_{ij} + a_2\varepsilon_{kk}\delta_{ij}$$

where ε_{kk} is the trace of the strain tensor, and ϵ^0 is the dielectric constant of the unstrained material. It has been pointed out that this expression is flawed, since when the incompressibility constraint is relieved, the stress components are multiplied by the Poisson ratio of the material [40]. In all circumstances, this error is minor.

When the dielectric tensor depends upon the strain, the stress calculated by equation 3.3 retains strain-dependent components,

$$\sigma_{ij}^{\text{electric}} = \epsilon_0\frac{2\epsilon^0 - a_1}{2}E_iE_j - \epsilon_0\frac{\epsilon^0 + a_2}{2}E^2\delta_{ij}$$

which are all of second order in the dielectric field, just like the Maxwell stress. Explicitly, electrostriction arises from the strain-dependence (a_1, a_2) of the dielectric tensor, while the Maxwell stress arises from normal polarisation of the dielectric medium.

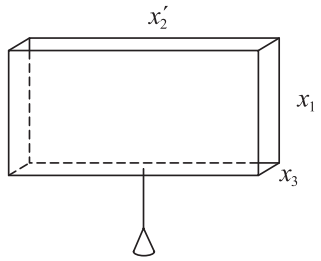

Figure 3.4: Dimensions of the actuator. The width of the actuator x_2' is constrained, while the length x_1 and the thickness x_3 are free to change. Finally, a weight is hanging from the actuator to apply a constant force.

For the elastomers deployed in this work, the electrostrictive constants are negligible, hence the term dielectric elastomer actuators, with no reference to electrostriction. For some workers, electrostriction is explicitly sought for, a typical elastomer to this end is poly(vinylidene-flouride), and also its copolymer with triflouroethylene [3, 5, 6]. When the films are irradiated with electrons with energies of 3 MeV, the large polarisation domains of the elastomer are broken up into many smaller domains, enhancing the electrostrictive properties. With such materials, electrostrictive strains of 5% have been observed, for an applied electric field of 200 MV/m. Though the strain is not that large, with an actuation energy density (see section 6.2) close to 200 MPa, the electrostrictive actuators are still important. Actuators made from polyurethane are also electrostrictive [2, 12, 13], here strains of 4% have been observed.

3.3 Elasticity and Maxwell stress combined

The theories of elasticity and Maxwell stress are now combined, under the assumption that the actuator (figure 3.4) is constrained in the width direction, such that

$$x_1 = \alpha x_1' \qquad x_2 = x_2' \qquad x_3 = \alpha^{-1} x_3'$$

A weight is attached from the bottom of the actuator, and the electric field is applied along $\hat{\boldsymbol{x}}_3$. All *forces* have to balance,

$$f_{\mathrm{g}} + f_{\mathrm{Maxwell}} = f_{\mathrm{elastic}} \tag{3.4}$$

This formula is evaluated for all three models of elastic behaviour under width constraint.

Before continuing, a new definition of the strain must be introduced, the actuator 'engineering' strain. This strain measure is more useful for describing actuation, when both a weight is suspended from, and a voltage is applied to the actuator.

The actuated length and strain are written as explicit functions of the applied mass and voltage, $l(V,m)$ and $\varepsilon(V,m)$. With these functions, the normal strain is written as

$$\varepsilon(V,m) = \frac{l(V,m) - l(0,0)}{l(0,0)}$$

while the new, engineering strain is defined as

$$\varepsilon'(V,m) = \frac{l(V,m) - l(0,m)}{l(0,m)}$$

where the reference position is different for each weight. The engineering strain is calculated from the normal strain by noting that

$$l(0,m) = l(0,0)\,(\varepsilon(0,m)+1)$$
$$l(V,m) = l(0,0)\,(\varepsilon(V,m)+1)$$

Collecting the above, the engineering strain in terms of the normal strain becomes

$$\varepsilon'(V,m) = \frac{\varepsilon(V,m) - \varepsilon(0,m)}{\varepsilon(0,m)+1} \tag{3.5}$$

an equation which is used for evaluating the engineering strain from the strain delivered by the models.

3.3.1 Hooke model

For the Hooke model, the result is easily derived,

$$\begin{aligned} & m\,g + \frac{x_2'}{x_3'}\epsilon\epsilon_0 V^2\alpha = G x_2' x_3' (\alpha - 1) \\ \Leftrightarrow \quad & \alpha = \frac{G x_2' x_3' + f_g}{G x_2' x_3' - \frac{x_2'}{x_3'}\epsilon\epsilon_0 V^2} \end{aligned} \tag{3.6}$$

The expression has a singularity, which for silicone rubber occurs at an electric field of roughly 600 MV/m, far above the dielectric breakdown strength of silicone rubber.

The engineering strain is calculated by combining equations 3.5 and 3.6. Abbreviations are used, $k \equiv x_2' x_3' G$, $f \equiv mg$, and $e \equiv x_2' \varepsilon\epsilon_0 V^2 / x_3'$, by which the (real) strain is written as

$$\varepsilon = \frac{k+f}{k-e} - 1$$

and the engineering strain becomes

$$\varepsilon' = \frac{\left(\frac{k+f}{k-e} - 1\right) - \left(\frac{k+f}{k} - 1\right)}{\left(\frac{k+f}{k} - 1\right) + 1} = \frac{k}{k-e} - 1$$

which is independent of the weight applied to the actuator.

3.3.2 Neo-Hookean and Mooney-Rivlin models

The Neo-Hookean and the Mooney-Rivlin models returned the same behaviour for an elastomer film obeying a constrained width (section 2.5.1). For simplicity only the Neo-Hookean model is evaluated. The calculation of the strain response using the Neo-Hookean begins by writing the force-response of the constrained elastomer film. The result was derived in chapter 2, equation 2.13, which when inserted in the force balance equation becomes

$$m\,g + \frac{x_2'}{x_3'}\,\epsilon\epsilon_0 V^2 \alpha = x_2' x_3' G \left(\alpha - \frac{1}{\alpha^3}\right) \tag{3.7}$$

In order for Mathematica© to solve this equation using a smaller amount of computing time, some parameters are redefined. This also helps in understanding the structure of the equation. Replacing $\alpha = \varepsilon + 1$, and defining $f = mg$, $g = x_2' x_3' G$, and $e = \frac{x_2'}{x_3'}\,\epsilon\epsilon_0$, the above equation is written in the more readable form,

$$g\left((1+\varepsilon)^4 - 1\right) = f(1+\varepsilon)^3 + eV^2(1+\varepsilon)^4 \tag{3.8}$$

which is a fourth degree polynomial in the strain.

The equation is solved by Mathematica© using the input sequence `Solve[g((1+x)^4-1) == f(1+x^3)+eV^2(1+x)^4,x]`, which returns 4 roots, of which the first two are complex, the third is strictly negative, and the fourth makes sense. Unfortunately, this root is much too space consuming to be written here. In Mathematica© the root is used as an analytic function, in which all the physical parameters introduced above may be inserted. For a given actuator, all these parameters are known, such that the function has two free variables, the mass of the weight attached from the actuator and the voltage applied to it. The output of the function is the equilibrium strain, obtained when the actuator is at rest. This derivation returns the *static* strain; an analysis of the *dynamic* strain must include kinematic terms in the force balance equation, equation 3.4. Such an analysis on DEA was performed by P. Sommer-Larsen *et al.* , in reference [41].

3.3.3 Ogden model

The relationship between force and strain is no longer analytic, since the exponents of α may attain any real number. The approach adopted is to measure the force-strain curve of a given actuator, fit the obtained curve to the Ogden model for constrained width, equation 2.15, and plug the fit into the generic force balance, equation 3.4. The expressions for the forces from the applied weight and voltage are the same, and an equation is obtained, which is written as

$$\sum f = mg + \frac{x_2'}{x_3'}\epsilon\epsilon_0 V^2 \cdot \alpha \; - \; f_{\mathrm{Ogden}}(\alpha) = 0$$

The (physical) root of this equation is the stretch ratio, α, which balances the forces. The root is found with Mathematica© by numerical evaluation, using the routine `FindRoot[`*expression*, *parameter*`]`, refer to appendix C.

The above models can be evaluated for experimental actuators. For a silicone actuator, the properties of which are listed in section 6.4, the theoretical curves are plotted in figure 3.5 for an applied weight of 50 g. The curve of the Hookean actuator model lies lowest, because the elastic force from the Hooke model is highest. For the same reason, the Neo-Hookean model predicts the highest strain, simply because the predicted elastic force is the lowest. Finally, the Ogden model gives a prediction that lies between the prediction of the Hooke and Neo-Hooke actuator models.

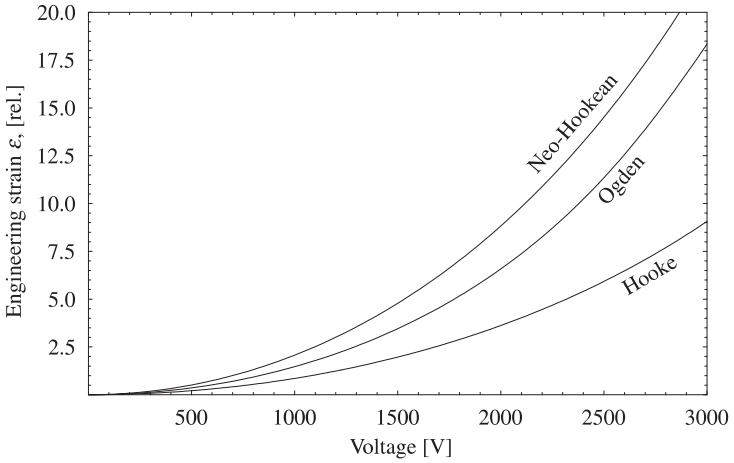

Figure 3.5: The voltage-strain curves, as predicted by the presented models. The applied weight was 50 g. The values entering the model are listed in section 6.4. The fitting programs are listed in appendix C.

3.3.4 Strategies for model improvement

The strain state in the centre of the elastomer film is different from the strain state on the edge of the film; this variation is not included in the model. Since the stress depends on the strain, also the stress state varies over the elastomer film. To include this variation, the stress and strain tensors should be written as functions of position, and the Maxwell stress should be included in the stress tensor. The given state should then be obtained using a variational calculation, or through finite element modelling. This is a complicated approach, and was considered to be too elaborate for this experimentally oriented thesis.

4

Applied percolation

The concept of percolation is explained using the following supposition. A box is filled with two types of spherical balls: insulating and conducting. The purpose of this experiment is to measure the conductance from one side of the box to the other. For measurement purposes, two juxtaposing sides of the box are electrodes.

The experiment begins with insulating balls only. It is found that practically no current can be drawn from one electrode to the other. Conducting balls are then added in random positions one by one, while removing insulating balls to keep the number of balls constant. During this, the development of the conductance is measured. The number of conducting balls divided by the total number of balls is the fraction, p, of conducting balls, and the properties of the system are measured with respect to this quantity.

The addition of one conducting ball does not change the conductance markedly. As conducting balls are added, two or more might accidentally end up next to each other, forming a *cluster*. As the number of conducting balls grows, the structure of the system becomes complex. At some point it is more reasonable to describe the system using distributions of e.g. cluster sizes. Individual clusters grow larger, and they begin to coalesce. In this process one single

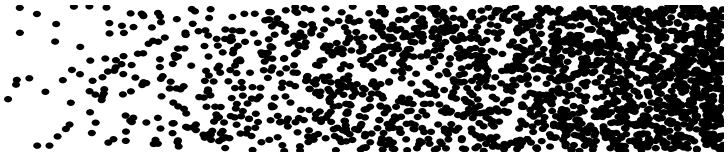

Figure 4.1: Black balls are placed at random in a two-dimensional space, with increasing probability upon going from left to right. The cluster sizes become larger when going from left to right, until finally one cluster connects the top and bottom of the picture. This picture does not resemble an actual physical experiment, because balls are allowed to overlap.

cluster (the incipient cluster) becomes very much larger than the rest [42], and in the end the incipient cluster of conducting balls is as large as the whole box. A connecting path is established between the electrodes, and a huge jump in the conductance of the system is observed. Addition of more conducting balls only increases the conductance slowly, therefore a *threshold* in the conductance becomes distinct. This threshold is known as the percolation threshold [42], and the volume percent at which it occurs is p_c.

Another percolation experiment is sketched in figure 4.1. Black balls are placed at random, with increasing probability from left to right. At the far left, one ball lies isolated. Going right, two balls lying close are encountered; they constitute a cluster of two. Further right, clusters grow larger and larger, while the number of clusters changes little. Further right still, adjacent clusters begin to coalesce, the number of clusters drops to just a few, until they finally coalesce completely, to form a path from the lower picture frame to the upper. The fraction at which a conducting path is established is defined as the percolation threshold.

Of course, this illustration is flawed in several ways: balls are allowed to overlap, and a range of experiments cannot be condensed this way into one picture. Pictures of random mixtures at single volume fractions p should be presented. Nevertheless, this simple figure illustrates some aspects of the nature of percolation.

The transition from a non-conducting to a conducting mixture is a critical transition. Because of this, when the experiment is repeated, the same p_c is not necessarily obtained. This is due to the finite size of the experimental system. If the experiment were performed many times, large fluctuations in the conductivity close to p_c would be observed, as for the magnetisation in a magnet close to the Curie temperature. A better estimate of p_c is obtained when the size of the system is increased, until the change in p_c is low.

Most percolation studies deal with obtaining the value of p_c. This can be obtained in many ways, both analytically and through simulation. The percolation threshold of just a few systems can be derived analytically, one limitation being that only systems of dimensionality lower than 3 are solvable [42]. Further, only percolation thresholds on certain types of lattice can be derived analytically. Therefore, it is necessary to rely on approximations, simulations or experiments to obtain a value for p_c. It is well established that for an experiment with insulating and conducting balls, as described above, the percolation threshold has a value of $p_c = 16\%$ [43].

4.1 Rubber and graphite mixtures

The artificial muscles under study in this thesis all have compliant electrodes made from binary mixtures of an insulating substance and graphite. Percolation influences the dielectric properties of the mixture. The mixture of polymer and graphite is the system of choice for many experimentalists [44–46].

Consider a mixture of a polymer and graphite. The polymer is regarded as insulating, while the graphite is conducting. Consider the polymer as an insulating background, while the dispersed graphite powder can be considered as conducting flakes. It is important to use laboratory measures that mix these substances very thoroughly. A properly mixed sample has a random distribution of graphite in the polymer background.

The dielectric spectrum of a given mixture is a good way to inspect the state of percolation. For volume fractions above and below p_c, the mixture will be either insulating or conducting. The development of the conductive and dielectric properties of the system as more graphite is added is discussed in the following.

4.1.1 Experimental

The experiment presented in figure 4.2 was also presented in an unpublished report [47]. A short description of sample preparation follows.

The samples were prepared as a mixture between graphite powder (4206, Merck, Germany) and Dow Cornings Sylgard 184, which is a two-component silicone[1] rubber kit. The rubber cross-links by addition of a carbon double bond to an Si–H bond, on the backbone of a silicone polymer. The addition process is catalysed by a platinum complex. The graphite consists of flakes of hydrolysed coal, with flakes in sizes around 10 μm in length.

It is important to obtain a random distribution of flakes in the rubber, in order to achieve percolation. The graphite was pre-wetted in excess heptane, and then subjected to several hours of ultra-sound for complete wetting. The graphite-heptane slurry was used as one component in the mixing of a whole range of samples with varying volume percentage of graphite.

The Dow Corning kit was also pre-mixed with heptane. Because the graphite flakes are hydrolysed, some of the catalyst is consumed in side reactions; therefore the amount of cross-linker was increased when the graphite content

[1] Silicone, also known as poly-demethylsiloxane, oil has the following structure: –O–Si$(CH_3)_2$–

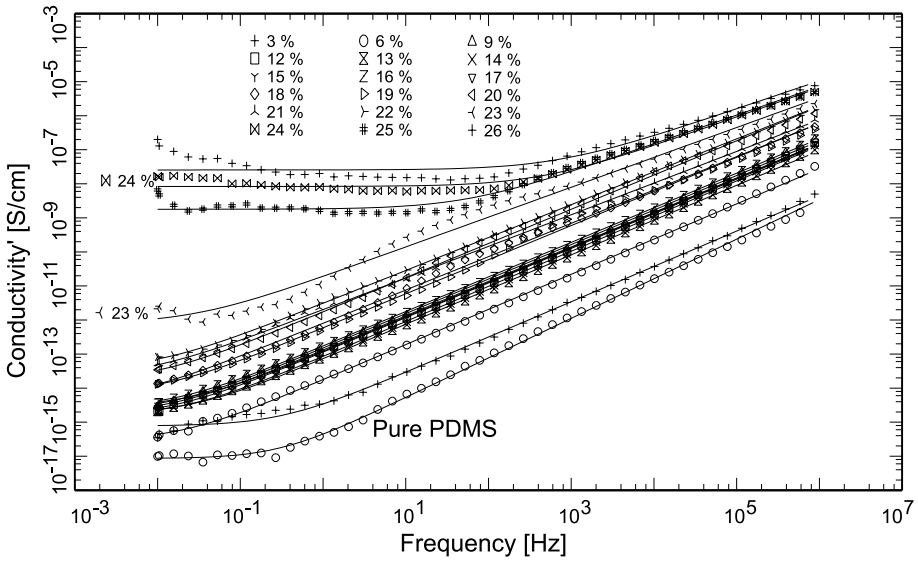

Figure 4.2: A percolation experiment. Samples of Merck's graphite and Dow Corning Sylgard 184 were made with the volume percentages, p, indicated on the graph. The conductivity is plotted vs. the frequency in a log-log diagram.

became large. This has no effect upon the dielectric spectrum, since the catalyst is only present in trace amounts, and the weight distribution of the base component and the cross-linking components are the same.[2]

The amount of heptane added to the pre-mixes is important for calculation of the volume percentage of graphite in the silicone rubber. The density is 0.68 g/mL of heptane, and is 1.1 g/mL of silicone rubber, while that of graphite is 2.23 g/mL. Using the definition of the volume percentage,

$$p_{\text{graphite}} = \frac{V_{\text{graphite}}}{V_{\text{rubber}} + V_{\text{graphite}}}$$

it is possible to keep track of the graphite content in the final samples, even though heptane is present in the mixtures during sample preparation.

[2] As measured with HPLC by Walther Batsberg, The Danish Polymer Centre, Risø

Samples were cast from a heptane solution directly on to glass plates. The silicone rubber does not adhere strongly to the glass plates, making it easier for the samples to peel off. The heptane content when casting must be low, otherwise the graphite will sink to the bottom of the slurry, and then the samples will no longer be random mixtures, that possess percolation qualities.

The final thickness of the samples was from 500 μm to 1000 μm, which is easy to handle. Samples were prepared with graphite content in percentages from zero to 30%, in steps of 1%. The conductivity jumps very much between the samples with $p = 23\%$ and $p = 24\%$, the jump is about 4 decades in conductivity at 10 mHz, the hallmark of percolation.

For low p, the graphs have a constant slope of ~ 1. For $p > p_c \approx 23\%$, the graphs have a constant plateau at low frequencies, while at higher frequencies they return to a slope of ~ 1. The conductivity graphs are always shifted upwards for higher p. It seems that the very low p curves have a constant plateau as well, but this is an artefact caused by the limitations of the dielectric analyser.

4.1.2 Analysis of conductivity spectrum

The development of the conductivity at zero frequency, the dc conductivity σ_0, is found for all conductor-insulator systems to be

$$\sigma_0 \propto |p - p_c|^t \tag{4.1}$$

Therefore it is expected that σ_0 will diverge close to the percolation threshold, which will then serve as a clear indication of the value of p_c.

A mathematical fitting function is introduced, which fits the conductivity curves in figure 4.2 fairly well [44],

$$\sigma' = \sigma_0 + \beta\omega^\gamma \tag{4.2}$$

The full curves in figure 4.2 are fits of this function to each experimental curve. The results are presented in figure 4.3.

The dc conductivity jumps by five orders of magnitude close to $p = 23\%$. These data are not very good, therefore it is futile to attempt to fit them to equation 4.1. The pre-factor, β, designates the cross-over frequency from the frequency-independent to the frequency-dependent part of the experimental curves [44]. It is seen to be increasing with increasing volume percentage, though there is a plateau in the centre region, 10–17 p%. Finally, the exponent,

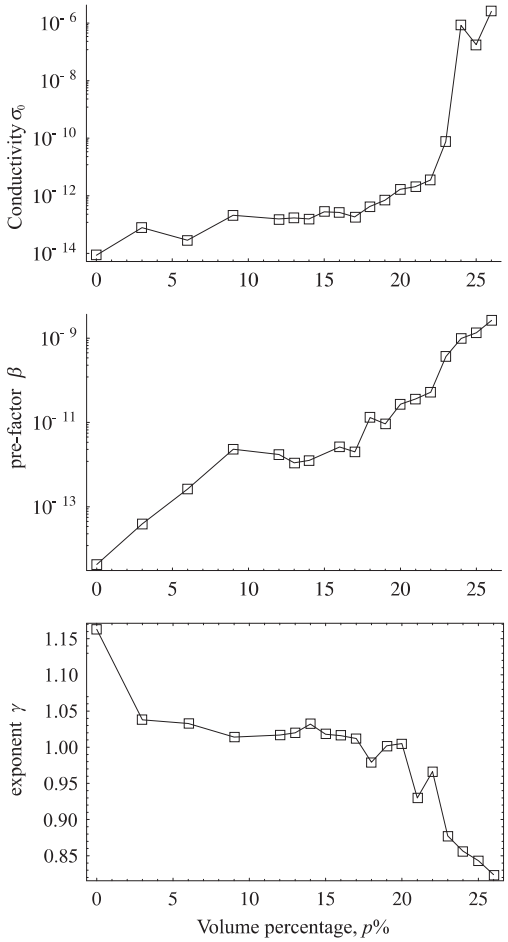

Figure 4.3: Plots of the parameters in equation 4.2, fitted to the data in figure 4.2.

γ, is decreasing with volume percentage, and again a plateau is present, here from $p = 3 - 20\%$. In [44], the exponent γ is the same for all volume fractions above the critical. It must be concluded that data quality is inferior, and one should therefore refrain from comparing them to the model presented in [44].

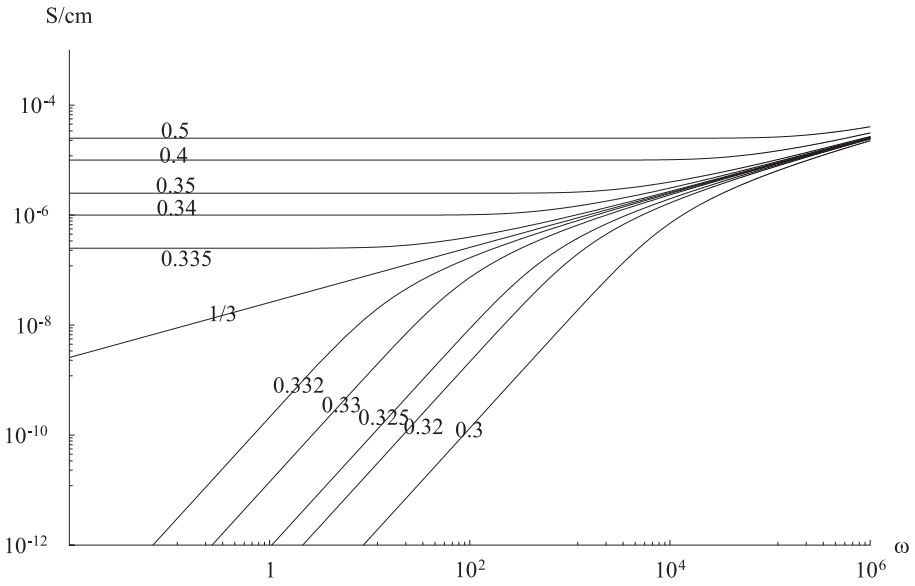

Figure 4.4: Plots of the real part of the conductivity, as predicted by the effective medium approximation. For all curves, the same values of ϵ and σ were used, $\epsilon = 3\epsilon_0$ and $\sigma = 0.0001$.

4.2 Effective medium approximation

One approach to obtain approximate percolation behaviour in a model of binary mixtures is the effective medium approximation (EMA) [43]. The effective medium approximation is a semi-analytical model for describing the qualitative nature of the conductivity spectra. The conductivity is evaluated for a network known as the hypercubic network, which consists of links between lattice points. The links may be either conducting or insulating, as determined by a distribution function $\rho(\sigma)$, where σ denotes the conductivity of a single link.

In two dimensions the hypercubic network is the links between the lattice points on the square lattice, in three dimensions the hypercubic network corresponds to the simple cubic lattice. A single link between two adjacent points A and B has been replaced with a link of conductivity σ_{AB}. An electric field

V_0 is applied on the links parallel to AB. The voltage on AB, V_{AB}, is generally different from V_0, since generally $\sigma_{AB} \neq \Sigma$. The voltage fluctuation, defined as $V_{AB} - V_0$, is required in the EMA to vanish, when it is averaged over all distributions $\rho(\sigma)$ of link conductivities.

The link conductivities may resemble those of an insulator ($\sigma = 0$), a dielectric ($\sigma = i\epsilon\omega$), a conductor ($\sigma = \sigma_0$), or a superconductor ($\sigma = \infty$). For a binary mixture of two types of links (σ_1 and σ_2), averaging over all configurations with a probability p for a link with σ_1, and probability $q = 1 - p$ for σ_2, the result is

$$p\frac{\Sigma - \sigma_1}{\sigma_1 + (d-1)\Sigma} + q\frac{\Sigma - \sigma_2}{\sigma_2 + (d-1)\Sigma} = 0$$

which is a second-order polynomial in Σ. When $d = 3$, $\sigma_1 = \sigma$, and $\sigma_2 = i\epsilon\omega$ is inserted, the root with a positive real part is

$$\Sigma = \frac{1}{4}\left((3p-1)\sigma + (2-3p)i\epsilon\omega + \sqrt{\Delta}\right) \tag{4.3}$$

with a discriminant

$$\Delta = (3p-1)^2\sigma^2 - (2-3p)^2\epsilon^2\omega^2 + 4(1+p(1-p))i\epsilon\sigma\omega$$

In this three dimensional model, the percolation threshold is $p_c = \frac{1}{d} = 0.33$.

A graph containing curves, plotted for several volume percentages p in equation 4.3, is shown in figure 4.4. The volume percentages are indicated on each curve. For the lowest percentages, the low frequency part has a slope of 2 in the log-log plot, which flattens out to a slope of 1 at higher frequencies. For higher p, the low frequency part is shifted upwards. When $p = \frac{1}{3}$, the curve has a slope of exactly 1. Curves for higher p have a flat region at low frequencies, and a region with slope 1 for higher frequencies.

The low frequency features for the curves with $p < \frac{1}{3}$ are not found in the data of figure 4.2. All the other features of the data have been reproduced by the EMA, apart from the percolation threshold of $\sim$ 23%. It is therefore inferred that the data indeed do correspond to a percolating system, yet they are inferior with respect to predicting any critical values, as was possible for Adriaanse *et al.* [44].

4.3 Compliant electrodes

The concepts and knowledge gained form the percolation experiment presented in this chapter was put to use in the design of compliant electrodes. The term 'compliant' designates the ability of a thin, conducting electrode to follow the strain of the artificial muscle, without generating opposing stress or losing any conductivity. In this thesis, only electrodes made from the general system 'polymer-graphite' were put to use. Measurements on the value of the conductivity of the electrodes have not been made. The resistance of the electrodes or the electrode material was only tested with a multi-meter, to establish if there was percolation.

4.3.1 Carbon black

The previous experiments dealt with a mixture of a cross-linking rubber matrix, Dow Corning Sylgard 184, and graphite with a high percolation threshold, Merck's. The percolation threshold of the mixture is lowered dramatically if more structured graphite is used. This kind of graphite is usually called carbon black, because it is deep black compared to the graphite, which consists of flakes that have metal lustre.

Burning oil incompletely in a special furnace, under controlled conditions results in highly structured carbon black.[3] Percolation thresholds as low as 0.03% have been reported [44], though this is rare. Carbon blacks with percolation thresholds of 5% to 50% are available commercially [48].

The reason for the lowering of the percolation threshold is elucidated by the following thought experiment: consider a carbon black shaped as a long string (e.g. carbon nanotubes), which is as long as the distance from one electrode to the other. If this one carbon nanotube reaches from one electrode to the other, in principle the condition for percolation is met, as the 'mixture' is electrically conducting. The percolation threshold in this experiment would be vanishing.

Akzo Nobel supplies a carbon black under the name Ketjenblack EC-300J [49]. The appearance is powder-like and black, the material is supplied as little nodules of 2 mm in diameter, with much dust in between. The material is very fluffy, therefore the density of the powder before use is extremely low, $\sim$ 100 g/L. According to the technical papers [49], the percolation threshold

[3] Carbon blacks are soots, and are also known as furnace blacks.

of Ketjenblack EC-300J is about 5%. The structure of single particles is that of shells linked to shells, with consequent deep pores and a high degree of internal structure.

When 10 mL heptane is added to 200 mg of Ketjenblack in a small vessel, the mixture hisses, therefore the suspension reaction is exothermic. If the mixture is left to itself, the Ketjenblack sinks to the bottom, taking up only the lower 5% of the vessel. Then the mixture is subjected to about 1 hour of ultra-sound, which breaks the nodules apart and forces the Ketjenblack into suspension, resulting in the Ketjenblack distributed in the whole vessel. Left to itself, the Ketjenblack suspension now collapses very little.

The density of Ketjenblack, or of any furnace black, has to be defined from the nature of its surroundings. The density of graphite in most solvents is 2.2 g/mL, as it is very easy for solvents to wet all surfaces on the graphite. The volume of the graphite is minimal, and therefore the apparent density is maximised. Ketjenblack on the other hand has high internal structure, therefore the density suggested by the technical papers was 1.75 g/mL [49]. These issues have to be taken into account, when binary mixtures of polymer and carbon black are used for conducting electrodes.

4.3.2 Grease electrodes

Ketjenblack suspended in heptane is easy to work with. Heptane also dissolves PDMS oil, including the elastomer-forming Sylgard 184 kit. For grease electrodes, PDMS oil with a viscosity of 500 cst was chosen. Suspensions were prepared with volume percentages of 3%, 5%, 10%, and 20%, by first suspending the Ketjenblack in heptane using ultra-sound, and then adding the PDMS, which was dissolved in heptane as well. Knowing the weight of the PDMS oil, the weight of Ketjenblack to be added is calculated from the density formula, $m = \rho V$, where p is the desired volume fraction,

$$p_{\mathrm{KB}} = \frac{V_{\mathrm{KB}}}{V_{\mathrm{KB}} + V_{\mathrm{PDMS}}} \quad \Leftrightarrow \quad m_{\mathrm{KB}} = \frac{\rho_{\mathrm{KB}}}{\rho_{\mathrm{PDMS}}} \frac{p_{\mathrm{KB}}}{1 - p_{\mathrm{KB}}} m_{\mathrm{PDMS}}$$

The density of silicone oil is $\rho_{\mathrm{PDMS}} = 1.0$ g/mL, and the density of Ketjenblack is taken to be $\rho_{\mathrm{KB}} = 1.75$ g/mL in PDMS.

The mixtures were capped, and placed in ultra-sonic bath over night. The caps were removed and the vessels placed in the fume hood, to allow the heptane to evaporate. It takes at least two days for the heptane to evaporate if the grease is left in the vessel.

The conductivity of the four mixtures was measured with a multi-meter, and they were all conducting, though the 3% mixture had a high resistance, and was discarded because of this. The smearing properties of the three other mixtures varied. The mixture with $p = 20\%$ of Ketjenblack was impossible to smear out as a nice thin layer, with the 10% fraction it was possible, but best results were obtained with the $p = 5\%$ mixture. The resistance when two electrodes were jammed into the mixture at random was on the order of few Ohm. This mixture was used as grease electrodes, and for establishing electrical connection.

As a grease electrode, the conducting grease is very good. With actuator strains below 50%, there was no significant migration of the electrode material. Visible migration was only detected in actuators with strains above 100%, here the grease tended to roll up as small cylinders, perpendicular to the direction of strain. The whole electrode area as such was still conducting, as the actuator was able to perform at more than 100% of strain. The drawback of a grease electrode is that it is messy to handle.

4.3.3 Rubber electrodes

In order to make electrodes more stable, the PDMS oil is cross-linked. A different silicone rubber kit is used, RTV-1. This is a one-component silicone glue, which cross-links at room temperature when it is exposed to moisture in the air, releasing acetic acid as condensation bi-product. Several glues of this type was used, of which Wacker© E43ⓡ RTV-1 Silicone Glue was best. The volume percentage was 20% Ketjenblack in glue. Ketjenblack and glue was mixed with heptane in separate vessels. The evaporating heptane keeps moisture away from the glue, preventing unwanted cross-linking. Following ultra-sound treatment, the smaller vessels are poured into a bigger 'reactor vessel', which is then filled with heptane and shaken vigorously. The mixture in the reactor vessel can be stored for at least a month without degradation or loss of glue power.

The mixture is sprayed onto a silicone film with an airbrush. The solution has to be thin otherwise it is not possible to control the amount of electrode material. It is very important that the surface does not wet completely during spraying. If there are large amounts of liquid solution on the electrode surface, the components will separate, such that the over-all structure is not percolating, resulting in non-conducting areas (see figure 5.6). This is mediated by applying very little material at a time, and by using wide strokes. When the

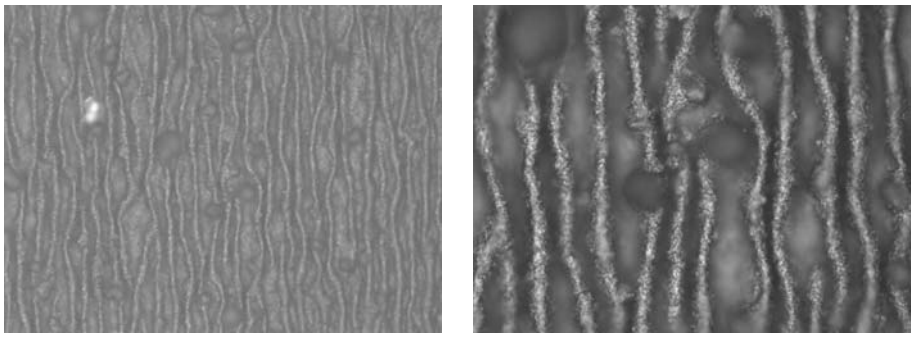

Figure 4.5: Microscope images of PDMS / Ketjenblack electrodes, at 20× and 50× magnification. The ridges form when the 'substrate' silicone elastomer film is relaxed, by which the electrodes that are sprayed on top will suffer compressive strain, which is relieved by the ridges mentioned.

solution hits the surface, most of the heptane has evaporated. The solution is now subject to moisture in the air, therefore the glue cross-links, and a stable, conducting rubber is formed. These electrodes can only be used for silicone rubber actuators, since it is well known that silicone will only stick to silicone.

The silicone actuators presented in this thesis were all made by stretching the silicone film 100% on a frame before spraying. This was to make sure that the electrode film was able to stretch at least 100% before breakdown processes would occur. To test the order of magnitude of the resistance of the rubber electrodes, solution was sprayed on a large piece of silicone film. Small dots of conducting grease (section 4.3.2), were placed at random over the sprayed area, for better electrical connection with the film. The typical distance between dots was a few cm. A multi-meter was used for resistance measurements, and the measured resistance was in the range of 10–50 kΩ. For the high voltages used for actuation this is quite a low resistance.

Images of the sprayed rubber electrodes were made with an optical microscope at 20× and 50× magnification, see figure 4.5. The films were mounted at 0% strain. Ridges are visible on top of the films perpendicular to the stretch direction of the films when they were sprayed.

The buckling of the electrodes influences the force-strain curve of the actuator, but the effect only sets in from 50% strain. The Mooney-Rivlin fit deviates from the data, much earlier than for the measurement presented in chapter 2.

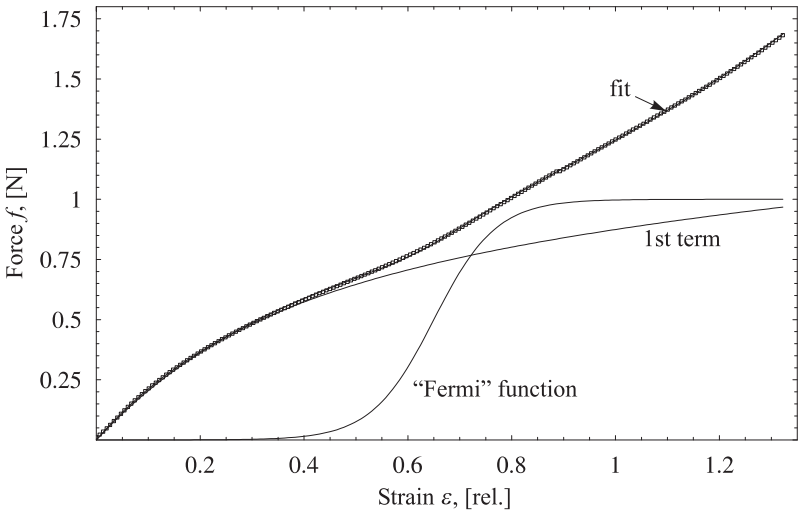

Figure 4.6: Force-strain curve for an Elastosil 625 silicone actuator with sprayed electrodes. The full curves are fits of the Neo-Hookean and Ogden models to the data, and also the 'cut-off' function is plotted. The tensile modulus was 990 kPa, from the Hooke model. The details of the fitting of the Ogden model are described in the text.

This deviation is attributed to the electrodes, which do not affect the stiffness of the actuator while they are buckling. At higher strains the ripples are stretched out, by which the electrodes behave like a regular elastic band. Therefore they do not contribute to the over-all force-strain behaviour at low strain, while at higher strain their influence slowly sets in.

The force-strain behaviour was also fitted with the Ogden model, which was adapted specifically for the purpose. A two-term model was used, one to fit the part of the force originating from the elastomer film, and one part for the electrodes. In the electrode part the extension ratio, α, was multiplied by a factor λ in order for this part to find its own 'zero length'. A special function, $\theta(\varepsilon)$, was introduced by this author in order to 'turn off' the electrode fitting term for low strains. This function resembles the Fermi-Dirac distribution, known from quantum mechanics, though here it was adapted to become zero for small strains, and one for larger strains. The final fitting function is of the

form

$$\begin{aligned} \frac{f}{x_2' x_3'} &= \mu_1 \phi(k_1, \alpha) + \theta(\varepsilon)\mu_1 \phi(k_2, \lambda\alpha) \qquad (4.4) \\ \theta(\varepsilon) &= \left(1 + \exp\left(\frac{\varepsilon_0 - \varepsilon}{\Delta\varepsilon}\right)\right)^{-1} \end{aligned}$$

The fitting of this expression to the experimental data obtained on a silicone actuator with rubber electrodes, is performed with a fitting program written in Mathematica. A non-linear fit routine was employed, which was necessary because the exponents k_l are non-integer. The program used for fitting is presented in appendix C.

The best fit was obtained for the following values,

$$\begin{array}{ll} \mu_1 = 388 \text{ kPa} & k_1 = 1.300 \\ \mu_2 = 16.7 \text{ Pa} & k_2 = 6.03 \\ \lambda = 2.984 & \\ \varepsilon_0 = 0.67 & \Delta\varepsilon = 0.06 \end{array}$$

The fit is plotted with the values in figure 4.6, and indeed a pretty nice fit is obtained. This fit is used as the basis for modelling silicone actuator response.

The rubber electrodes were also imaged with a confocal microscope (Zeiss LSM 5 PASCAL), which images topography variations on surfaces. The period of the ridges was ca. 20 μm, and the height was $\sim$ 5 μm. From a rough estimate the thickness of the electrodes is between 5 μm and 20 μm.

The required thickness of the film depends upon the percolation threshold, as well as the amount of conducting material used in excess of the threshold. The geometry of the electrode is that of a thin film. Thus, the size of the clusters is limited in the thin dimension of the film, so it is possible that the volume fraction is in a range where the film is conducting along the thin dimension, while it is insulating across the film. The percolation threshold is therefore effectively increased. There is an upper limit to the amount of carbon black since there must be room for the glue that sticks the carbon black to the film, and lends elastic stability to the whole electrode.

4.3.4 Dust electrodes

Many of the results presented in this thesis were obtained on actuators made from 3M© VHB™4910 tape. This film is very compliant, it stretches at least

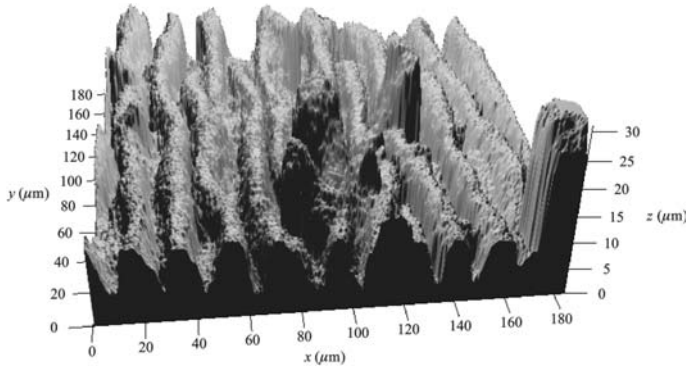

Figure 4.7: Zeiss LSM 5 PASCAL confocal topography imaging of relaxed Ketjenblack / DC732 30 / 70 sprayed electrode.

700% before snapping. It is of a class of tapes known to be pressure-sensitive, in which the sticking force depends strongly upon the stress field. For this tape the consequence is that it sticks very well, unless shear forces are applied, then the tape is readily released. The tape is a 1.0 mm thick film.

The VHB film is easily stretched on a frame, up to 6 times in two directions (corresponding to 500% $\times$ 500% strain). After this stretch the film is still sticky. Everything sticks to the film (except silicone), including carbon black. A carbon black supplied by Cabot®, Vulcan XC 72 R, is a powder when supplied. This dust can be transferred to the VHB film using a small hairbrush. These electrodes are as conducting as the electrodes presented earlier, and they are stable. This kind of electrode is only possible to apply to films that are sticky.

4.3.5 Glue electrodes

An unsuccessful attempt at making sprayed electrodes for application to silicone film used hydrin as the binding material. Hydrin is a hydrogenated acrylonitrile / butadiene polymer, typically used in mixtures with polyethyleneoxide as a cross-linked ion-conducting material for e.g. batteries. The supplied material is a slightly yellowish, transparent and rubbery brick, with a density of 1.0 g/mL. It dissolves slowly in THF, and the solution process is hardly accelerated by applying ultra-sound. The spray solution was made with a

volume percentage of 50% Ketjenblack, and a large quantity of THF as carrier fluid. It is easy to spray, and sticks very firmly to most materials, except silicone. Silicone film actuators made with hydrin / Ketjenblack electrodes would work for a few cycles, then the electrode material begins to coalesce into small lumps on the surface of the film, because the gluing power is larger for hydrin / hydrin, than for hydrin / silicone.

The hydrin / Ketjenblack solution was put to use for fabrication of stretchable leads. Rubber string with an over-layer of cloth is available in any sewing store. This string is dipped into the solution several times, allowing it to dry between successive dips. After some 20 dips, it becomes quite conducting, $R \sim 10$ kΩ, and keeps the conductivity while and after being strained 100%. These leads are better than using aluminium foil for some applications, as the foil has sharp edges, which the conducting strings do not.

5

Experimental

This chapter is devoted to descriptions of experimental procedures, including measurement set-ups and manufacture of actuators. The principle behind the dielectric analyser is outlined. Actuator manufacture is presented, for actuators made from silicone elastomer and VHB™4910 . The actuator test bench is described, with some of the improvements caused by careful programming of the data sampling software.

5.1 Dielectric spectroscopy

A sample capacitor is made from two capacitor plates, clamped on either side of the sample, see figure 5.1. The capacitor plates are made from smooth brass discs, covered with a thin evaporated gold layer. The thickness must be constant over the entire sample, since an error in thickness results in a first order error in the measured dielectricity. Depending upon the type of sample, there are more sample preparation precautions to consider.

The principle of the measurement is to apply an AC voltage with a certain frequency to the sample, then measure the current through the sample. The applied and the measured signals are compared, to obtain the complex impedance of the sample [50]. From complex impedances at several frequencies, the complex dielectricity and conductivity spectra are extracted. The dielectric analyser has a sine wave generator and two analysis channels. It is named Broadband Dielectric Spectrometer, and was manufactured by Novocontrol.

The sine wave generator supplies a voltage $V(t) = V_0 \sin(\omega t)$ to the system under test (SUT), figure 5.2. With two probes, the signals $U_1(t)$ and $U_2(t)$ are extracted,

$$\begin{aligned} U_1(t) &= A_1 \sin(\omega t + \phi_1) \\ U_2(t) &= A_2 \sin(\omega t + \phi_2) \end{aligned}$$

These signals have certain amplitude and phase with respect to the incoming

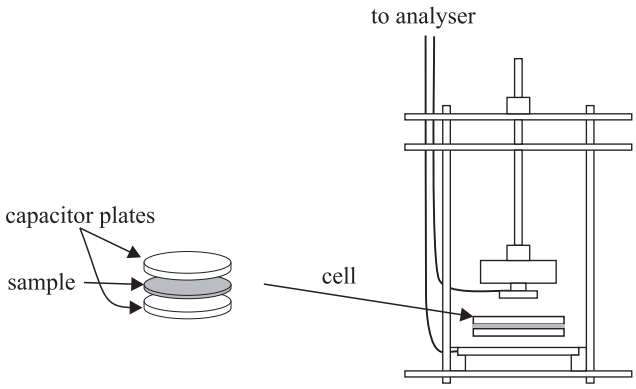

Figure 5.1: The sample capacitor is a thin film disc placed between two capacitor plates. It is placed in the sample holder, and clamped tightly in place, in order to ensure perfect connection between plates and sample.

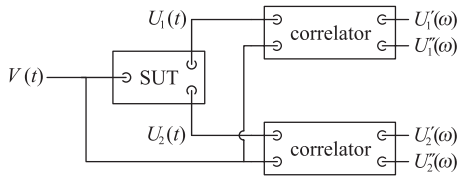

Figure 5.2: A sketch of the principle behind the measurement procedure of the dielectric analyser. A generator supplies a sinusoidal reference voltage, which is applied to the system under test (SUT). Two probes extract signals from the SUT, these are multiplied with the reference signal, and integrated over several periods of the applied signal. This returns two constant signals for each probe, from which the amplitude and phase is extracted. This procedure is repeated for a range of frequencies of the reference signal in order to obtain a full spectrum.

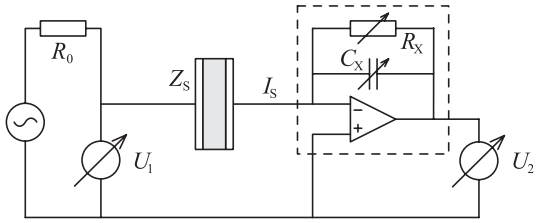

Figure 5.3: Measurement circuit for dielectric analyser. The generator supplies an oscillating voltage, which is applied to the sample in series with a protection resistor, R_0. The applied signal, U_1, is measured with a vector voltage analyser. The oscillating current from the sample is passed through an operational amplifier with an impedance Z_X in the negative feedback loop. Finally, U_2 is measured with a second vector voltage analyser.

generator signal. The analysis correlators transform the time-dependent signals into the frequency domain by multiplying the measured signal with the reference signal, for U_1

$$\begin{aligned} U_1'(\omega) &= \frac{1}{NT}\int_0^{NT} U_1(t)\sin(\omega t)dt \\ U_1''(\omega) &= \frac{1}{NT}\int_0^{NT} U_1(t)\cos(\omega t)dt \end{aligned}$$

where N is the number of periods $T = 2\pi/\omega$, over which the measurement is performed. The amplitude and phase (with respect to the reference signal) are calculated from

$$\begin{aligned} A_1(\omega) &= 2\sqrt{U_1'^2 + U_1''^2} \\ \phi_1(\omega) &= \arctan\left(\frac{U_1''}{U_1'}\right) \end{aligned}$$

The measurement circuit is sketched in figure 5.3. An alternating voltage is generated and applied to the capacitor in series with a safety resistor $R_0 = 50\ \Omega$. The actual voltage signal applied to the capacitor, U_1, is analysed with the correlator, as described above. After application to the sample capacitor, the sample current $\overline{I}_S$ is fed through the inverting entrance of an operational amplifier with variable impedance in the feedback loop (circuit

within perforated box in figure 5.3). The feedback stabilises the current, such that the voltage analysed with the second correlator is

$$\overline{U}_2 = -\overline{I}_S \, \overline{Z}_X$$

where $\overline{Z}_X$ is the impedance of the components in the feedback loop,

$$\overline{Z}_X = \left(\frac{1}{R_X} - i \, C_X \omega \right)^{-1}$$

The impedance of the sample under study is now extracted from $\overline{U}_1$ and $\overline{U}_2$ through

$$\overline{Z}_S = \frac{\overline{U}_1}{\overline{I}_S} = -\frac{\overline{U}_1}{\overline{U}_2} \, \overline{Z}_X$$

After each measurement, a reference capacitor is switched into the measurement circuit in place of the sample capacitor, and the measurement is repeated. The capacitance of the reference capacitor is chosen by the analyser to be close to the capacitance of the sample. The current through the reference capacitor is $\overline{I}_R$ and the impedance is $\overline{Z}_R = i/C_R\omega$. $\overline{U}_{1R}$ and $\overline{U}_{2R}$ are measured again (subscript *R* for 'reference'), but they are now used to determine the impedance of the components in the feedback loop,

$$\overline{Z}_X = -\frac{\overline{U}_1}{\overline{U}_2} \, \overline{Z}_C$$

The advantage of this procedure is that the reference measurement includes the impedance of all the wires and equipment, and this is not accounted for when computing Z_X from the values stated on the components. Also, as the reference impedance is comprised of just a capacitor, the value of its impedance is better determined than the value of $\overline{Z}_X$.

5.1.1 Impedance spectroscopy

An experimental procedure complimentary to dielectric spectroscopy is that of *impedance spectroscopy*. The primary difference is that the samples investigated using impedance spectroscopy are inherently conducting, therefore the real part of the impedance often is large compared to the imaginary part. A typical use for this method is the investigation of chemical reactions as

they take place. As a chemical reaction progresses, chemical species are consumed and others generated, imparting the sample with conductivity from ionic transport mechanisms. A single parameter describing the difference between the situations of perfect dielectricity or perfect conductivity is the loss angle, δ, defined as

$$\tan\delta = \frac{C''}{C'} = -\frac{Z'}{Z''}$$

For a near perfect dielectric the loss angle is very close to zero, while for a near perfect conductor, the loss angle is close to 90°. This has large implications for the electronic design of the analyser equipment. The dielectric analyser must be able to resolve a loss angle very close to zero, the Novocontrol resolves 0.00001°. This is possible because of the use of the reference capacitor. The impedance analyser achieves a resolution of 0.001°, close to $\delta = 90°$, by switching a reference resistor in place of the sample. When performing experiments on a sample to investigate for the frequency response, it is therefore important to know whether the interesting properties of a sample are in the conducting or insulating regime.

5.2 Actuator fabrication

The theoretical dielectric elastomer actuator consists of an insulating elastomer film with compliant electrodes on both sides. As the elastomer film has to be very thin for the dielectric field to be sufficiently high, the durability and strength of the film is small. Handling of the film during manufacture, and when put to service in the actuator, is facilitated by a suitable frame, to which the film is glued, either by itself (for VHB™4910) or with silicone glue (silicone films). The following sections deal with the problems, and the solutions arrived at. First, manufacture of actuators made from VHB™4910 is described.

5.2.1 VHB 4910 actuator manufacture

The manufacture of VHB™4910 (material data sheet: [51]) actuators begins with the stretching of the film on a frame. The stretching serves the purpose of thinning the film: the film as supplied has a thickness of 1.0 mm, which is far to thick for an actuator. By stretching the film 4 times in each direction,

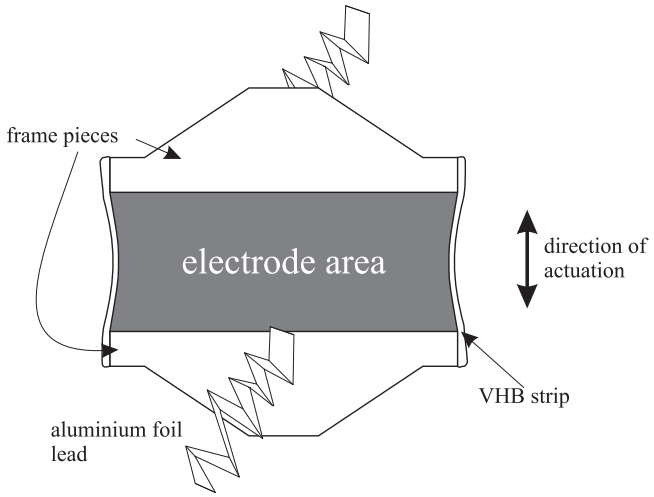

Figure 5.4: Sketch of VHB™4910 film actuator. The VHB™4910 film is pre-stretched in the direction perpendicular to the direction of actuation, therefore a stiff frame is needed to keep the pre-stretch. The electrode material should not be applied too close to the edges otherwise edge arcing will ruin the performance of the actuator.

the thickness drops to 1.0 mm$/4^2$ = 63 μm, which is excellent for actuator purposes. Stretching frames were made from polystyrene petri dishes, 14 cm in diameter. A hole is cut in the centre of the dish, in a suitable shape. A pattern of dots, 5 by 5 mm, is marked on the film, and the desired initial stretch ratio is defined on the frame by a layout of alignment dots. If the VHB™4910 film is not left too long on the frame it is possible to remove it, and slowly build up the desired initial strain configuration.

Actuator frames are made from a stiff plastic, 250 μm thick Mylar by DuPont, to which VHB™4910 glues very tightly. The Mylar is cut with scissors into frame pieces, of which four are needed for each actuator. The corners of the frame pieces are sanded down with P2000 sandpaper, such that they do not cut the film. They are placed directly on the film, which glues them firmly. Thin strips of VHB™4910 are glued to the sides of the film (see figure 5.4) for reinforcement of the sides when the actuator is released from the frame.

The compliant electrodes are applied before the actuator is cut from the

frame. It is necessary to use masking when applying electrodes. Both conducting grease and dust electrodes will work, see section 4.3.2. Aluminium foil strips are used for wire leads; they are taped to the frame using double-sided tape. The electrical connection between the leads and the electrodes is ensured with conducting grease.

5.2.2 Silicone film spinning

A typical elastomer kit consists of a base polymer, to which a small amount of cross-linking agent is added. The viscosity of a silicone elastomer kit is lowered with a solvent; heptane was the solvent of choice in this work. Polystyrene petri dishes serve as spinning substrates, because they are cheap and nearly flat. The petri dishes are blown clean with compressed air before use.

The spinner has options for acceleration and deceleration rates, spinner speed up 7000 rpm. and spinning time. Liquid elastomer kit was poured in the centre of the spinning substrate. A small pump sucks the substrate to the spinning clutch during spinning. Immediately after spinning, a lid is put over the petri dish, in order to avoid dust landing in the film. Then the petri dish is placed in an oven, at 60 °C. In the oven cross-linking is finished in $\sim$ 20 minutes and the viscosity lowering heptane is evaporated.

Several elastomer kits were tried: Dow Corning Sylgard® 184 and 186, and Wacker Elastosil® M4500, M4600, and RT 625. M4500 and M4600 were discarded immediately, one because it contained a pigmentation additive, the other because the base material contained lumps. Sylgard®184 and 186, and Elastosil® 625 produce nice, smooth films when spin-cast with heptane as viscosity lowering solvent. Typical spinning time is 60 s, and a typical spinning velocity is 700 rpm. The resulting films have a thickness of 20–30 μm.

The silicone films usually have radial variation in the thickness. Sylgard 186 especially produces films with a nip in the centre. About 20 mm from the centre and out the films are quite uniform, so centre part of the film is not used. For every batch of films the thickness and its variation was measured on a Sloan Dektak 3030 profilometer. Each film was inspected visually for dust specks and streaks.

5.2.3 Silicone actuator manufacture

The manufacture of silicone film actuators is more elaborate than the manufacturing of VHB™4910 actuators, because of the difficulties in film handling.

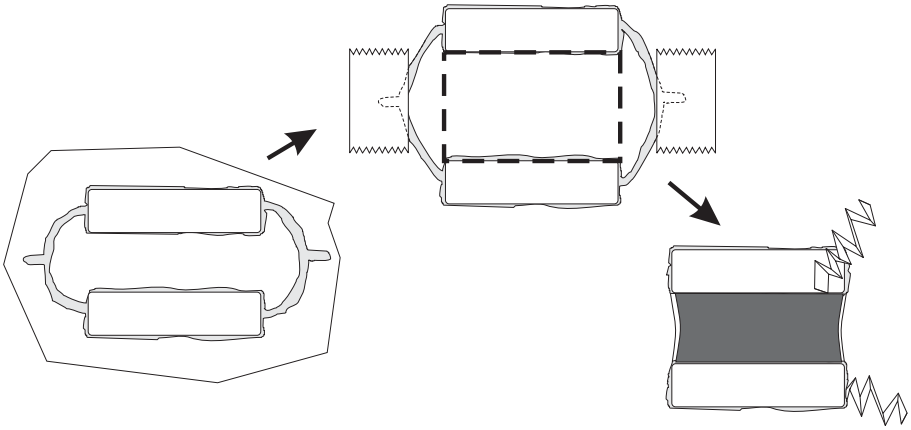

Figure 5.5: Sketch of silicone film manufacture. The steps are explained in the text.

Due to the low thickness of the films they are quite fragile. Temporary framing is necessary, and facilitated by applying thin lines of one-component silicone glue directly from the tube. The manufacture process of silicone actuators is sketched in figure 5.5.

First, two pieces of Mylar are glued to the film, which is still in the petri dish it was spun in. A handling frame of silicone is also marked up. With a scalpel, a cut is made around the whole structure in the petri dish, after which it is peeled off the substrate. Two such pieces are put together back to back to form one film (the reason for this is discussed later), and glued at the frame pieces. Then the two-layer film is stretched 100% on a spraying frame. The stubs are taped down to the frame, for keeping 0% stretch in the width direction, as sketched in figure 5.5.

Before spraying, everything but the film is masked by 3M™ Magic Tape, which does not stick firmly to silicone. An airbrush is loaded with the Ketjenblack / glue mixture described in section 4.3.3. Compressed air blowing through the airbrush sucks solution from a reservoir and blows it through an atomising nozzle. A flow pressure of 2 atm is used. Using a small flow of material ensures that the film surface never wets. Wetting would allow the components in the mixture to separate, ruining the percolation properties of the finished electrode. As soon as the material hits the surface, the glue com-

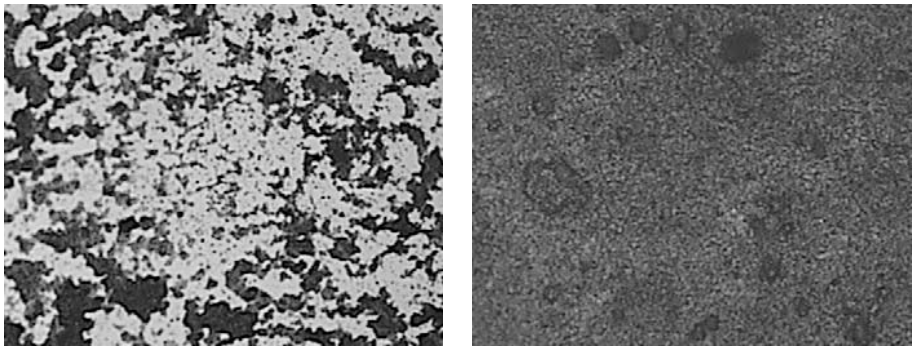

Figure 5.6: Optical microscopy images of sprayed Ketjenblack / PDMS rubber electrodes. The left image shows electrode material sprayed such that the adhering material was not allowed to dry during application. In the right image, electrode material was allowed to dry. The dry sprayed electrode is homogeneous in appearance, while the wet sprayed electrode is not interconnected, and therefore not conducting.

ponent cross-links, and the rubber electrode forms.

After spraying, the two films are released from the frame. The framing glue must be cut from the actuator in one, clean cut. Good quality of the cut is mandatory, because there is nothing else to keep cracks from propagating through the film. With a bad cut, small cracks are present on the edges, which can act as nucleation points for cracks.

5.3 Actuator failure mechanisms

An actuator may fail in several ways; these failure mechanisms should be countered. Some countermeasures unfortunately render the actuator useless, others allow the actuator to output the force and strain sought for.

One failure mechanism is tearing of the elastomer film. A fracture may appear on the edge of the film, which propagates through the whole film, ripping the actuator in two. Due to the large strains, even tiny cracks quickly grow until the actuator is destroyed. Further, a crack is not as insulating as the elastomer film, therefore sparks between the two electrodes will occur through the crack. When sparks occur, the build-up of charge is impossible, turning the

actuator useless.

Cracks are countered in different ways for silicone and VHB™4910 actuators. For silicone actuators made from Elastosil®625, it is enough to cut the edges of the film cleanly, with a scalpel. This impedes the creation of cracks; only one actuator was ever seen to tear. The edges of silicone actuators made from Sylgard®184 and 186 were reinforced by thin lines of one-component silicone glue. A straight line between the end-pieces of the actuator will add far too much stiffness to the actuator; therefore a zigzag line was made. With small enough angles between the segments, the zigzag line added no stiffness. The difference in tear strength between the Sylgard® elastomers and the Elastosil™ elastomer comes from an additive in the Elastosil™. The Elastosil™ contains micro-dispersed silica particles – well known to improve tear strength. The silica particles also endow the Elastosil™ with a slightly milky appearance, an appearance which the Sylgard® elastomers do not possess, they are perfectly translucent.

VHB™4910 actuators are reinforced by strips of the material itself, this ensures that actuator and reinforcements glue well. The reinforcing strips are applied to the film in a different state of stress, therefore the stress state varies rapidly in the region between them. This author believes that it is the stress variation which helps stop propagating cracks on the rim of the actuator. The reinforcing strips serve another important purpose, which is to stretch the actuating area in the width direction, maintaining a large actuation surface.

A final breakdown mechanism is that of dielectric breakdown: under applied voltage a defect region occurs, where sparks jump from one electrode to the other. This means death to an actuator. Dielectric breakdown mechanisms seem different for silicone and VHB™4910 actuators. Dielectric breakdown in silicone actuators seems confined to defects, while VHB™4910 actuators break down due to the applied electric field reaching a well-define maximum value, see section 6.3.

The reason for using two layers of film in the silicone actuator is to reduce the risk of burning the film. With a density of e.g. 1 defect pr. cm^2, film areas smaller than this area have to be chosen. With two films in series, the risk of two defects placed on top of each other is small, eliminating the risk of burning the actuator at defects. With these precautions, a typical breakdown field for silicone actuators was 50 MV/m.

The dielectric breakdown for VHB™4910 actuators is treated in detail in section 6.3.

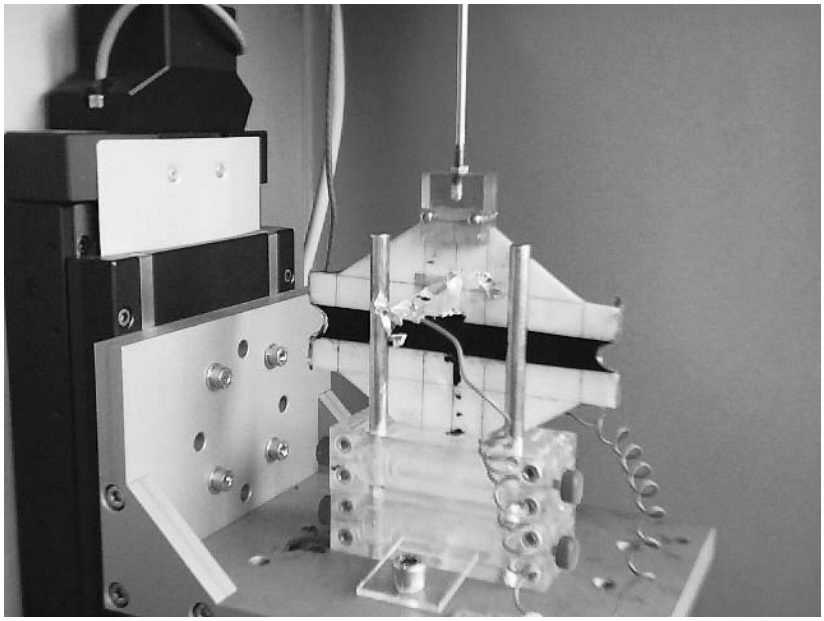

Figure 5.7: Picture of the actuator test bench. An actuator is mounted to a table, which again is mounted on the translation stage, seen leftmost in the picture. A shaft mounted to the top of the actuator reaches out of the picture to the force transducer. The actuating part is the black rectangle between the frame pieces.

5.4 Actuator test bench

In the ARTMUS lab, a test bench for the simultaneous measurement of force and extension was built. In addition, a high voltage amplifier is available. The frame of the test bench consists of a very stiff cage on top of a damped optical table (Thorlabs, Inc.). A translation stage manufactured by Physik Instrumente, Germany, was mounted vertically inside the cage. A computer interface card, manufactured also by Physik Instrumente, controls the translation stage. Under the ceiling of the cage a piezo-electric force transducer, model number GSO-250 (Transducer Techniques), is mounted. The transducer is powered and measured by an amplifier with analogue read-out (product

number TMO-2-240VI), which is fed to a National Instruments card (AT-MIO-16E-10). The high voltage (up to 10 kV) is generated by a high voltage tube amplifier, COR-A-TROL model 610D, manufactured by Trek®. It further has the possibility of reading out both the applied voltage and current. The data collection is performed on a computer, using LabView™5.0 software, distributed by National Instruments™.

5.4.1 Translation stage

The heart of the test bench is the translation stage. It has a range of 60 mm, with a precision of few μm. An electric rotation motor turns a spinnel with very fine turns, on which a sleigh slides. A table is mounted in this sleigh, to which a sample is fixed. The position of the spinnel is encoded by an optical sensor, situated behind a wheel with slits that are illuminated by a diode.

The position finding procedure is optimised for speed. The speed with which the controls turn the screw is determined by a PID procedure.[1] This allows long distances to be traversed somewhat quickly, though the top-speed is still only 2 mm/s. The translation stage is adequate for the static experiments presented in this thesis, but for dynamic experiments faster and longer-stroke equipment is needed; the loss of positioning accuracy for these experiments is not important.

The translation stage is programmable, parameters such as position, speed, and acceleration are set and read using drivers developed by Physik Instrumente. A complete set of drivers is available for use in LabView™5.0 programs.

5.4.2 Force transducer

The force on a sample is measured with a piezo-electric force transducer, manufactured by Transducer Techniques. The transducer measures both compressive and tensile (positive and negative) forces. With the 250 g transducer, measurement of forces up to 300 g is reliable. A combined voltage source and analog amplifier powers the transducer. The amplifier reads out a voltage signal

[1] A PID-optimised procedure is employed when it is important to find equilibrium quickly. When the state of the system is not in equilibrium, the control system estimates the position of the equilibrium. The distance from equilibrium is calculted to obtain the Proportional factor. The system reponse is also Integrated and Differentiated. The three calculated figures are multiplied by each their control factor, returning an estimate for the control parameter in question.

between −10 and 10 V, which is collected by the computer via a voltage I/O card. The I/O card offers just 12-bit resolution, much coarser than the amplifier signal noise. However, the input channel range is re-configurable, such that the 12 bits are used to resolve only the voltage range actually accessed in a given experiment. Averaging over 50 force measurements for each data point improves the resolution.

5.4.3 Force feed-back

The measurement of the actuation strain of an actuator with a weight hanging from it is one of the basic experiments to perform on an actuator. A weight is simulated with a force feedback loop involving the translation stage and the force transducer. The feedback loop attempts to apply a constant force on the ends of the actuator, without information about the applied voltage.

Using the current position and a force constant calculated from the immediately preceding data points, an estimate of the distance to the equilibrium position is made. The translation stage then moves to this position, with a speed proportional to the distance from the current equilibrium position. Below a certain distance from the estimated equilibrium position, the velocity is set to a constant value. The constant force experiment is simulated with this force feedback loop. For an actuator with no visco-elasticity, the feedback loop typically finds equilibrium within 1 s.

5.4.4 Stress-strain curve

Formulas for the relation between stress and strain were developed in chapter 2. Experimental data for elastomers are collected using the set-up described above. The translation stage is set to move with constant velocity, while the transducer reads the resulting force. Because the range of the translation stage is only 60 mm, the sample should be shorter than 20 mm for measurement of strains up to 300%.

6

Experimental results

A description of large strain elasticity was presented in chapter 2. An experiment on a piece of rubber string was used to illustrate the derivation, and it was established that the Ogden model was able to describe the force-strain behaviour for the entire range of strain. In chapter 3, the equation for the Maxwell stress was derived from the energy stored in a capacitor. Also in chapter 3, the two were combined for a DEA, yielding strain as a function of the weight and voltage applied to the actuator, under the constraint that the width of the actuator was fixed. In chapter 4, a experiment on the percolation properties of a graphite / silicone rubber system was presented.

In the following, force-strain curves are measured for some of the objects that are under study. The validity of the Maxwell stress equation will be shown experimentally. Then follows measurements on the dielectric breakdown strength of VHB™4910 . Finally, measurements of the voltage-strain curves for varying applied weight of several actuators will be presented, along with comparisons to the analytical model developed in section 3.3.

6.1 Force-strain measurements

In figure 6.1 the force-strain curve of a VHB™4910 actuator, with a constant width pre-strain of 500%, is shown. Again, the fits of the previously presented models are included, and again the Ogden fit is superior. The success of the Ogden fit derives from two properties of the model. First, the model has more free parameters than the other models, second, the exponents are fitted as well. The tensile modulus obtained from the Hooke model is 105 kPa, which is just 10% of the tensile modulus of silicone.

The return curve is also shown. The return curve does not follow the initial curve; it lies at lower forces. The lower force is caused by disentanglement of the constituent polymer chains. This has grave consequences for an actuator made from this material, since the elastic energy stored in the actuator material is not recovered completely, an effect which directly affects the attainable

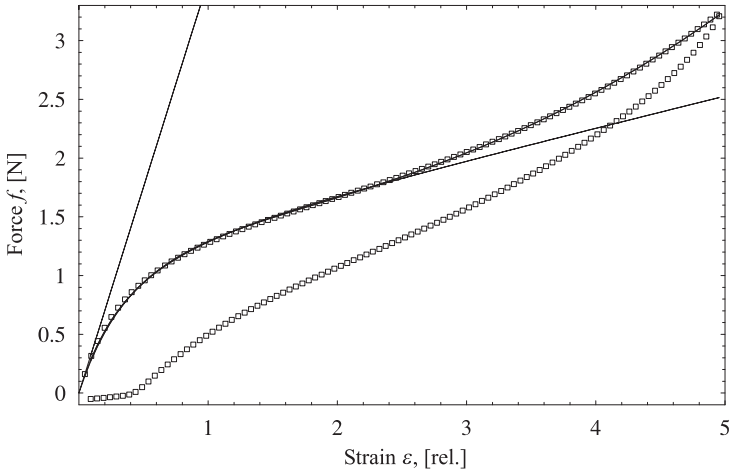

Figure 6.1: Force-strain measurement of VHB™4910 actuator, pre-strained 500% in the width direction. Initial length was 5.0 mm, the width was 100 mm, and the thickness 0.167 mm. The measured tensile modulus, from the Hooke model, was 105 kPa. The two-term Ogden fit yielded parameters $\mu_1 = 68.5$ kPa, $k_1 = 0.700$, and $\mu_2 = 767$ Pa, $k_2 = 3.441$, providing an excellent fit in the whole range.

efficiency of an actuator in operation.

6.2 Constant strain actuation

A simple experimental test of the validity of equation 3.3 follows,

$$\sigma = \epsilon\epsilon_0 E^2 \tag{3.3}$$

The actuator is pre-strained to a certain amount and then fixed in length. One end of the actuator is fixed to a force transducer, such that the force applied by the actuator on its surroundings is measured, see figure 6.2. The voltage is then varied, while the corresponding force is monitored. The actuation force measured in this type of experiment is known as the blocking force.

The co-ordinates of the system are as defined in figure 3.4: the length of the actuator lies along $\hat{\boldsymbol{x}}_1$, the width along $\hat{\boldsymbol{x}}_2$, and the thickness along $\hat{\boldsymbol{x}}_3$. All

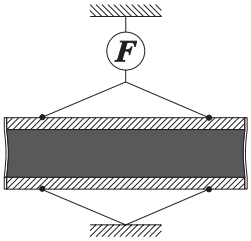

Figure 6.2: Experimental setup for the measurement of the blocking force from an actuator. The length of the actuator is fixed. A transducer measures the force output from the actuator.

dimensions are fixed during this experiment therefore the forces originating from the stetched elastomer are disregarded. Then the stress tensor is

$$T_{ij} = \epsilon\epsilon_0 E_3^2 - p\,\delta_{ij} \quad \Rightarrow \quad T_{11} = -\sigma_{33} = \epsilon\epsilon_0 E_3^2$$

The force originating from Maxwell stress, on the ends of the actuator, is then

$$f = x_2 x_3\, T_{11} = \frac{x_2 \epsilon\epsilon_0 V^2}{x_3} \tag{6.1}$$

The total force is inversely proportional to the thickness of the sample, proportional to the width, and to the square of the voltage. The length of the actuator does not enter equation 6.1, therefore it is a free parameter when designing an actuator.

The measurements presented were performed while visiting SRI International, and have been published in two articles [23, 52]. These articles are included in appendix B. Actuators were made from VHB™4910 , and carbon grease manufactured by CircuitWorks™ was used for electrodes. The films were pre-strained 500% in width, by which $\alpha_2 = 6$. The final width of the actuator was $x_2 = 200$ mm, and the zero strain length was $x_1' = 5.0$ mm ($\alpha_1 = 1$).

The pre-strains enter equation 6.1 as

$$f = \frac{x_2}{x_3'}\,\alpha_1\alpha_2\epsilon\epsilon_0 V^2 \tag{6.2}$$

From this equation it is seen that increasing the pre-strain, in both the length and width directions, enhances the generated force. The electric field applied

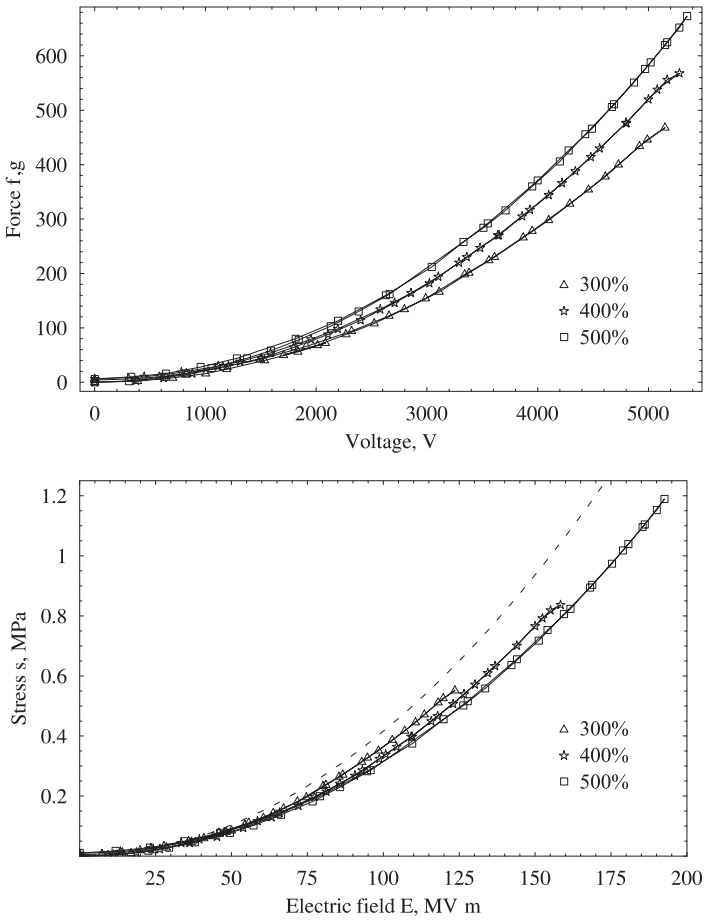

Figure 6.3: Measurements obtained on a VHB™4910 actuator with width pre-strains of 300%, 400% and 500%. The upper graph shows the measured force vs. the voltage. The data points for each pre-strain fall on separate parabola. The second graph shows the stress vs. the electric field as calculated from equations 6.3 and 6.4. Notice how the data points now fall on nearly the same parabola, as expected from equation 3.3. The dashed line is a plot of equation 3.3 for a dielectric constant of $\epsilon = 4.7$.

to the actuator is calculated from the voltage using

$$E_3 = \frac{\alpha_1 \alpha_2 V}{x_3'} \tag{6.3}$$

and the generated stress is calculated from the measured force using

$$\sigma = \frac{\alpha_1 \alpha_2 f}{x_2 x_3'} \tag{6.4}$$

The data is presented in figure 6.3. For each curve, the voltage was first increased from 0 V to $\sim$ 5000 V, then decreased. The uneven spacing between data points originates from the experimental procedure: the voltage was applied using a manually operated voltage supply.

The upper graph shows voltage vs. force, measured in gram. Before each measurement, a pre-strain in the length direction was applied, 300%, 400%, and 500% were chosen, with a worst case error of $\sim$ 10%. Voltages were varied between 0 – 5 kV. Usually, there is a tendency on the experimentalist's side to push the voltage as high as possible, causing electrical breakdown of the sample. Here, the sample was inspected visually during measurement. Wrinkles would appear at about 5 kV, with oscillations in the width direction of the sample. Experience showed that if the voltage were taken much higher the samples would burn, so the 'wrinkle limit' was imposed during measurements. When this limit was reached, the voltage was lowered, and a new set of data points was obtained for decreasing voltages.

The curves plotted in figure 6.3 are obtained from the same sample. Measurements performed on similar samples returned the same results. The resulting curves are parabolic, as expected from equation 6.2. The correlation between f and V^2 was investigated for several curves, the values of the relative standard deviation ranged from 2.32 to 5.36 per thousand.

The generated force at a given voltage increases with pre-strain, higher pre-strain gives higher force. The maximum generated force was 670 g. For comparison, the actuator with frame weighs about 10 g, and the active material, the dielectric film between the electrodes, weighs just 0.2 g, so this muscle supplies a force approximately 3000 times its own weight.

The second graph shows the electric field vs. stress, as calculated from the above equations. The three curves fall on nearly the same master curve, the parabolic curve predicted by equation 3.3, though there is a tendency for the higher pre-strain curve to lie a bit lower. The dashed curve is a plot of

the Maxwell stress from equation 3.3. The value of the dielectric constant of VHB™4910 is $\epsilon = 4.7$. The stress output was systematically lower than expected, for the three pre-strains the performance was 87%, 81%, and 76% in order of increasing pre-strain.

The shortfall of the generated stress is not explained by the presented theory. One explanation for the shortfall is that the experimental actuator has edges that curve inwards, a property, which lowers the active area, and adds to the thickness of the film, locally. Also, it is suggested that the assumption that all the stress generated by the electric field pushes in the length direction, is wrong. The assumption would hold if the sides of the actuator were completely stiff in the width direction, but in the experiment the sides of the actuator were seen to move a small distance. Indeed, for higher pre-strains the sides moved farther than for lower pre-strain, which complies with the more highly pre-strained actuator generating less stress.

The higher pre-strain curve reaches higher electric field, giving rise to higher stress. The stress is equal to the energy density, which is seen from a dimension analysis,

$$[\text{stress}] = \text{Pa} = \frac{\text{N}}{\text{m}^2} = \frac{\text{kg}\frac{\text{m}}{\text{s}^2}}{\text{m}^2} = \frac{\text{kg}\frac{\text{m}^2}{\text{s}^2}}{\text{m}^3} = \frac{[\text{energy}]}{[\text{volume}]}$$

Therefore it is concluded that higher pre-strains yield higher energy density.

6.3 Breakdown voltage

In the previous section it was seen that the curve for higher pre-strain was able to withstand a higher electric field. This interesting effect was investigated, also while at SRI International. Films of VHB™4910 were stretched an equal amount in each direction, and glued to frames. A film with an initial thickness of 0.50 mm was used for these experiments, since the voltage was limited to about 9 kV. The film was clamped between two planar metal electrodes with a diameter of 5.0 mm. The electrodes were mounted on a stand that allows measurement of the distance between the electrodes on a Mitotuyo™ thickness meter. The voltage was slowly driven to breakdown; the highest registered voltage was taken as the breakdown voltage. The pre-strains chosen were from 0% × 0% to 500% × 500%, in increments of 100%. About 30 measurements were made for each pre-strain, the results are shown in figure 6.4.

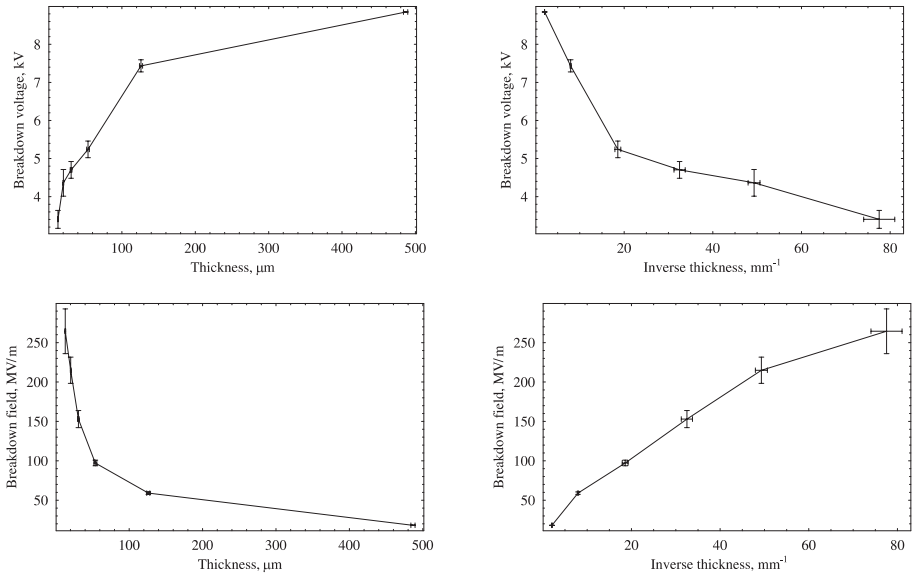

Figure 6.4: Plots of the breakdown properties of VHB™4910 , variables are indicated on the axes. The length of the error bars is equal to the standard deviation. Not shown is the calculated thickness vs. the measured thickness, which agree very well.

First, it is seen that thicker samples give higher breakdown voltages, from which it is concluded that the data are valid, because the breakdown is not caused by some glitch in the voltage source at a given voltage, or any other fault in the experimental procedure. Disregarding the other plots, the inverse thickness vs. breakdown field returns a near straight line, only the first and last points drop below. It is concluded that there is an inverse proportionality of the breakdown field on the inverse thickness. Note also, that the breakdown field increases from 17 MV/m to 270 MV/m from no pre-strain to the highest.

An heuristic explanation of this effect is given, based upon the molecular structure of the elastomer. The typical elastomer is composed of long chains of monomer, cross-linked at points hundreds of monomers apart. When the elastomer is stretched bi-axially, the chains are uncurled, forming a grid perpendicularly to the applied electric field. This grid has a higher cross-section for collision with the charges that are accelerated by the electric field. A high

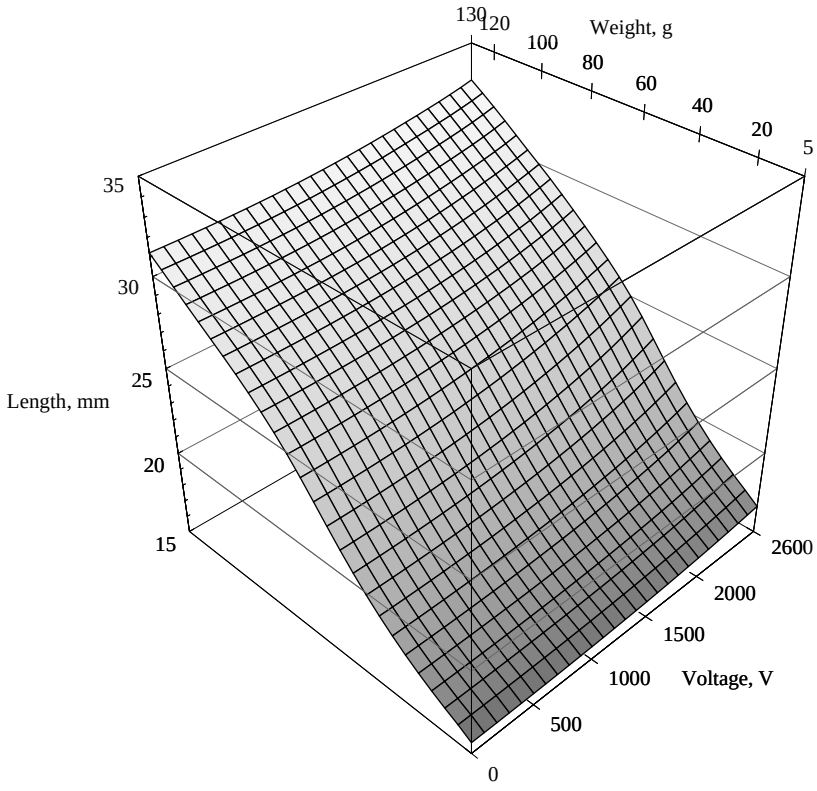

Figure 6.5: Directly measured length of the silicone actuator, of which the force-strain curve, and its fit, was presented in figure 4.6.

cross-section impedes the accelerating charges from gaining enough energy to start an avalanche, which would otherwise result in electric breakdown.

6.4 Silicone actuators

Silicone actuators were manufactured by the procedures described in chapter 5. The width of the elastomer film between the frame pieces was $x_2' = 44$ mm, and the width of the sprayed electrode was only $w_2 = 40$ mm, in order to avoid edge arcing. The thickness of the Elastosil®625 elastomer film was 26 μm, by which the thickness of the two-layer actuating film became $x_3' = 52$ μm. The length of the unstrained actuator was $x_1' = 15.0$ mm. The volume of the active material is then 30 mm^3, and the mass is 33 mg.

The actuator was mounted in the actuator test bench described in chapter 5. The force feedback measurement procedure was used, the voltage was applied from 0 V to 2600 V in steps of 100 V, while the applied weight was varied from 5 g to 130 g in steps of 5 g. The actuator would burn if the voltage was increased, therefore a breakdown voltage of ~ 50 MV/m can be inferred. This is half the nominal value, which fits well with expectation, since two layers of elastomer were used. It is expected that both films have defects, but that they do not lie atop each other.

The length as measured is plotted in figure 6.5, as a function of applied weight and voltage. The data points are placed at the intersection of the lines on the surface plot. Notice how smooth the surface is, a sign of how well the actuator test bench performs these measurements

Not surprisingly, the length of the actuator increases for increasing voltage and weight. The minimum length of the actuator is 15.7 mm, while the maximum length is 33.0 mm. The overall maximum strain is therefore 110%. Other than this not much information is obtained from this plot, as it is quite featureless. The features hidden in this plot are, however, brought forward by plotting the engineering strain, as defined in section 3.3. The engineering strain for the silicone actuator is presented in figure 6.6.

A striking feature is a pronounced peak in the strain, which comes about because the voltage is constrained to 2600 V. When travelling along the 2600 V iso-line, the strain at 5 g is 6.16%, then it increases for higher applied weight. This continues until a maximum strain of 12.68% is reached at an applied weight of 55 g, after which the strain drops. For this particular actuator it can be concluded that it has the longest stroke, when it works against a weight of 55 g. It is also seen that the slope of a strain curve at a given weight is always increasing. This feature emphasises the importance of being able to increase the breakdown voltage.

To complete the presentation of the data, a contour plot of the engineering

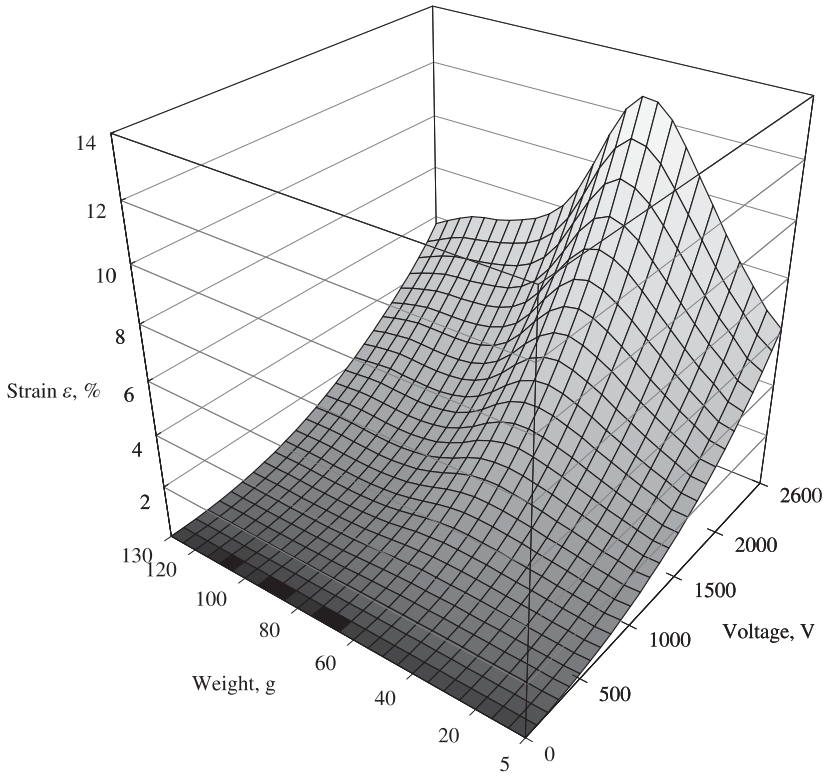

Figure 6.6: The engineering strain, calculated from the data in figure 6.5.

strain is presented in figure 6.7. Again an optimum applied weight is visible, contour lines surround the point (55 g, 2600 V) quite narrowly. When scrutinising the contour plot, it can be seen that the optimum weight shifts, when the voltage is increased. If it were only possible to apply a voltage of 1000 V, the optimum weight would be 60 g.

It should be noted, that measurements of this quality for dielectric elastomer actuators have never been presented before, and that the conclusion that a DEA has an optimum in the strain for applied weight, is new. This also underscores the usefulness of the concept of engineering strain.

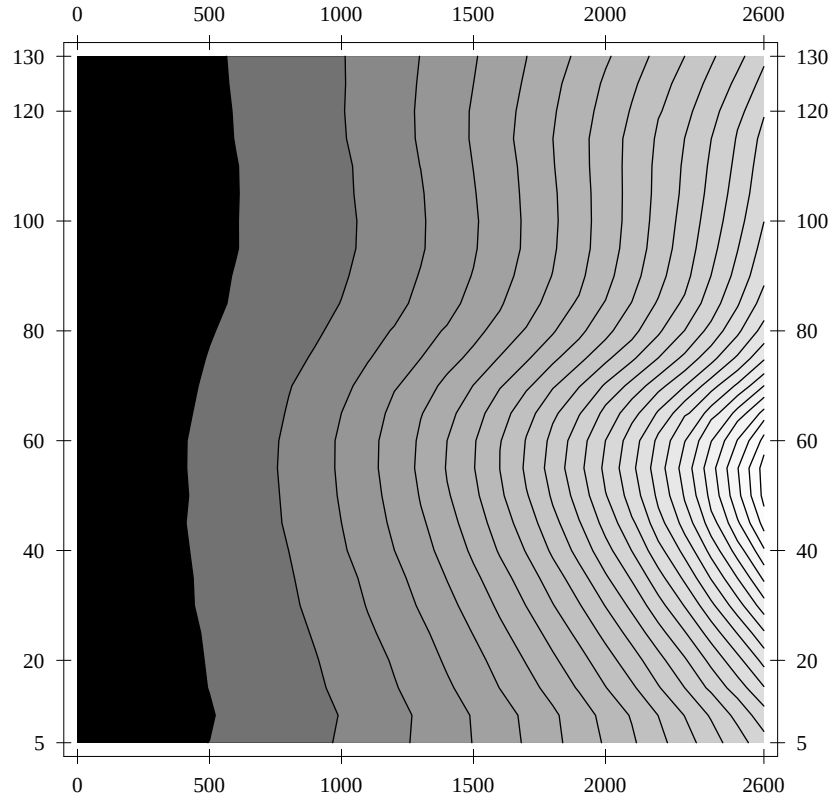

Figure 6.7: The engineering strain, calculated from the data in figure 6.5, plotted in a contour-plot.

6.4.1 Model of the silicone actuator

The values stated above are used for modelling the silicone actuator, applying the scheme outlined in section 3.3.3. The elastic width of the actuator is set to 44 mm, while the width in the Maxwell stress part was set to just 40 mm, since this was the width of the electrodes. The dielectric constant was $\epsilon = 2.3$. The engineering strain obtained from this model is plotted in figure 6.8.

The model is seen to capture the features of the experimental data over

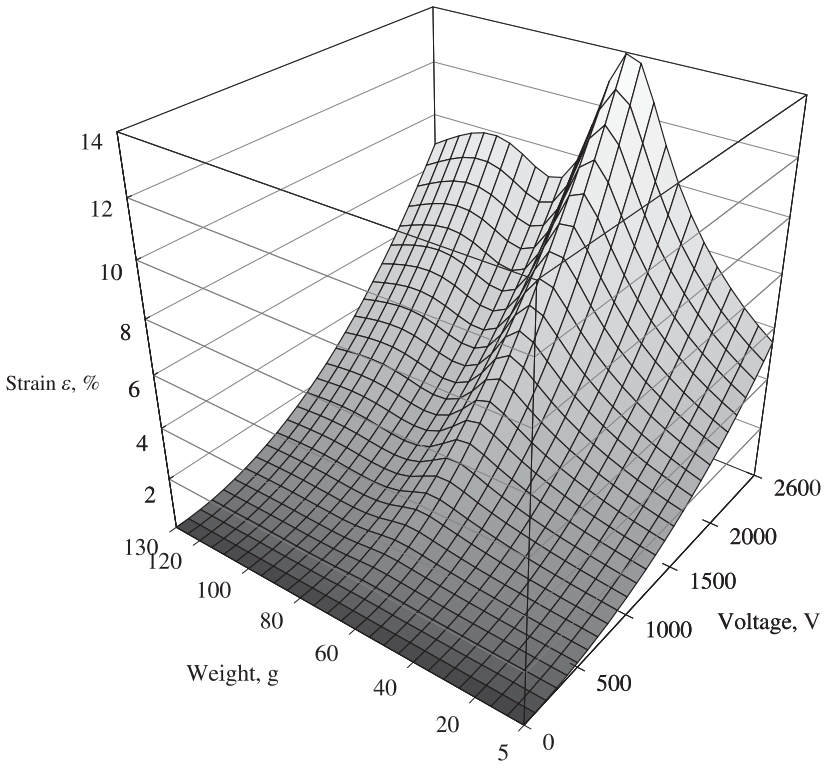

Figure 6.8: The engineering strain, calculated from the model. The dielectric constant was set to $\epsilon = 2.3$.

quite a large area. The optimum weight at 2600 V is still 55 g, though now an extra, local maximum appears at 100 g. The 'ridge' around the 55 g strain curve is narrower than for the measured data. The engineering strain of the model peaks at 13.95%, only 10% off the measured value, which must be considered a huge success, since for this model only the stress-strain behaviour is fitted, the remaining parameters are all real, physical parameters as measured on the actuator. It is concluded that the (Ogden) model of the dielectric elastomer actuator captures the properties of this silicone actuator to a high degree.

6.5 VHB™4910 actuators

A set of VHB™4910 actuators was made, with grease electrodes. The initial pre-strain in the width direction was varied between 300%, 400%, and 500%, the total width was 100 mm, and the zero-strain length was 5.0 mm. The actuators were mounted in the actuator test bench described previously, section 5.4, and the applied weight and voltage were varied, such that a whole grid of measurements was obtained.

As a safety precaution, invoked only to protect the actuators from burning during test, the voltage was kept as low as 4 kV. VHB™4910 actuators will withstand voltages of 5 kV, but under testing they still had a tendency to burn, probably caused by spikes in the applied voltage. A computer I/O card of mediocre quality controlled the voltage supply, this card is likely to produce spikes when the voltage is changed in steps. Because the voltage was limited to 4 kV, the resulting strains presented here are not as high as they could be.

6.5.1 Width pre-strain 300%

Results obtained from the actuator manufactured with a pre-strain of 300% are presented in figures 6.10, 6.9, and 6.11. The sequence of measurements of individual points in the grid is the following. A weight was chosen, then a series of voltages was applied in steps of 100 V, starting from 0 V and ending at 4000 V. The applied weight was varied from 80 g to 270 g in increments of 10 g. The data as measured are plotted in figure 6.9, again the individual data points lie at the intersections of the grid lines.

In figure 6.10 the engineering strain is plotted. At lower applied weight, the max strain reaches a level of about 20%. As the applied weight is increased, the attainable strain also increases, until it saturates at 55% at a weight of 140 g. Adding more weight causes the max strain to drop, but at an applied weight of 170 g a sudden increase is observed, when the strain jumps to 60%. The jump occurs because the actuator begins to wrinkle, inducing waves along the direction of the width of the actuator. Apparently these wrinkles further the length increase, rather than impeding it. The wrinkles help to relieve the constraint imposed on the width, allowing the actuator to expand more easily in both directions.

Adding more weight reduces the strain, at a weight of 250 g the maximum strain is lowered to 25%. As a result of this a clear maximum in the output strain is observed, the maximum strain is above 50% for applied weights from

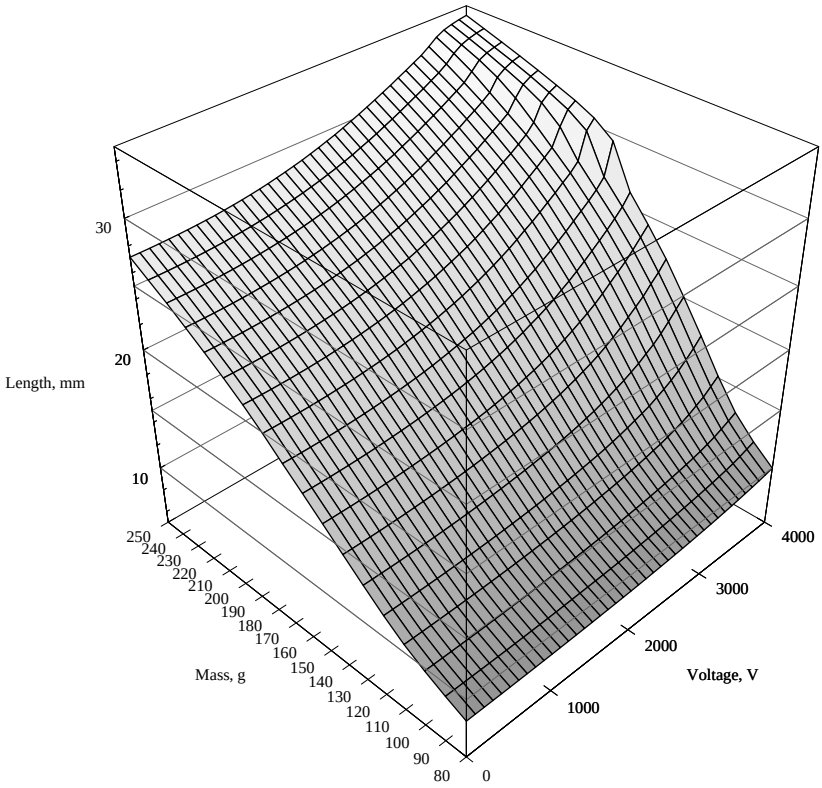

Figure 6.9: Plot of the length during actuation of a VHB™4910 actuator, for which the pre-strain in the width direction was 300%. The measured data points lie at the intersections of the grid-lines.

130 g to 180 g, peak strain lies at 140 g. The maximum strain is below 30% for applied weights below 90 g and above 240 g.

A contour plot of the engineering strain is shown in figure 6.11. As an overall feature, the contour lines lie closer and closer for higher voltage. This is clear indication of the importance of being able to increase the dielectric breakdown field. With a higher breakdown field, far higher actuation strains

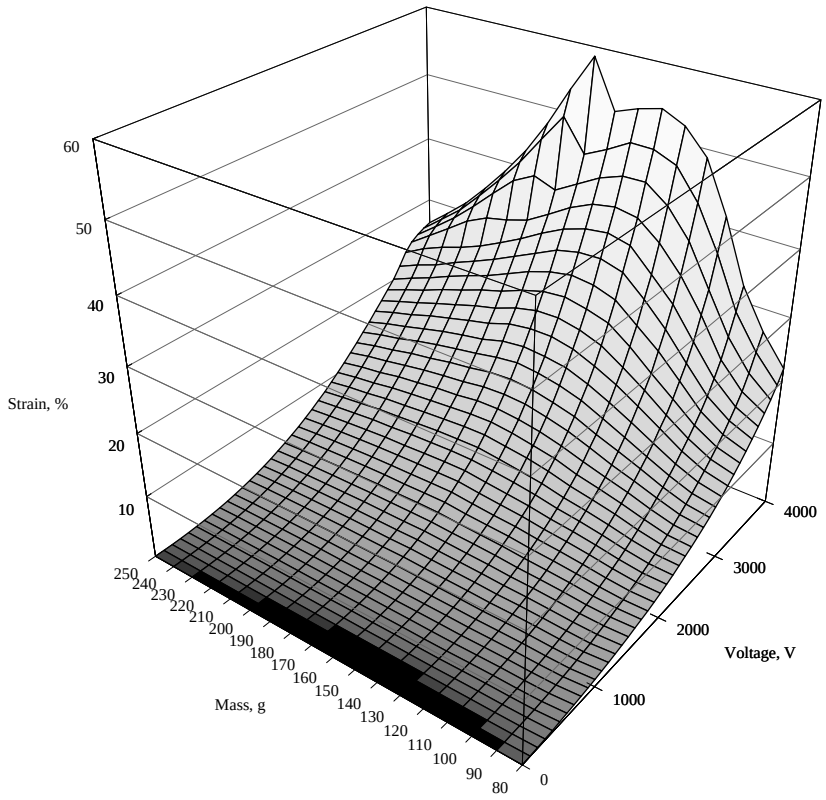

Figure 6.10: Plot of the engineering strain for a VHB™4910 actuator, pre-strain in width direction was 300%. The step in the strain surface at $\sim$ 170 g derives from the actuator entering a new actuation mode, in which wrinkles occur in the width direction of the actuator.

would be achieved, since the strain is proportional to the voltage to a higher order than 1.

The contour plot also reveals the onset of wrinkle mode actuation, here as dense iso-strain curves. From this plot it is seen that the wrinkle mode begins at lower applied voltage for higher applied weight. It is seen that if no wrinkle

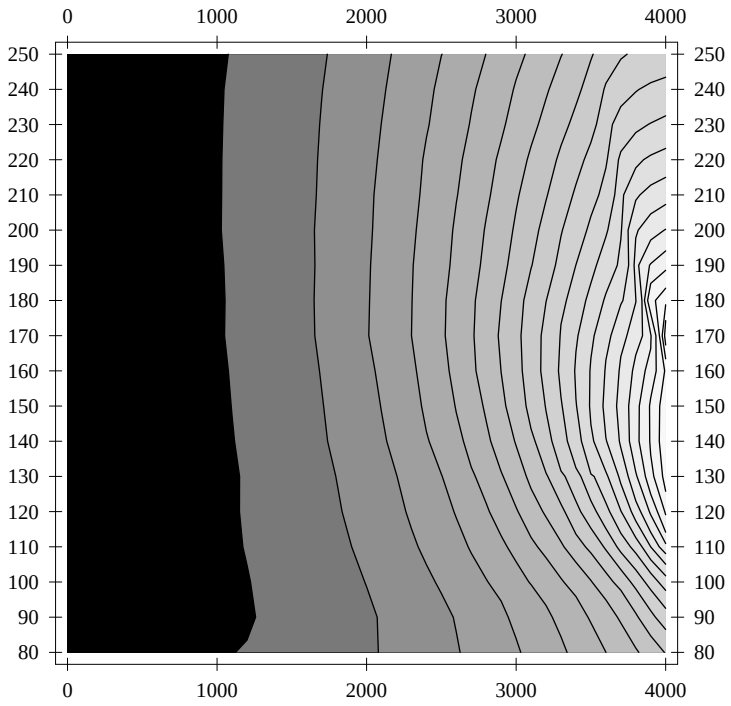

Figure 6.11: Contour surface of a VHB™4910 actuator, for which the pre-strain in the width direction was 300%. Now the 'wrinkle' actuation mode appearing at high applied weight and voltage is very clearly seen.

mode appeared the global maximum would lie at ca. 145 g, but the appearance of the wrinkle mode introduces a narrow peak at 170 g, exceeding the other.

An attempt was made at modelling the VHB™4910 actuator, with the model applied to the silicone actuator, section 6.4.1. A value for the dielectric constant of $\epsilon = 4.7$ was used [51], and the same range of voltages and applied weight. The force-strain curve of the actuator was measured in a separate experiment, and used as input for the model calculation. The result is presented in figure 6.12.

The model returns an estimate that is much higher than the measured val-

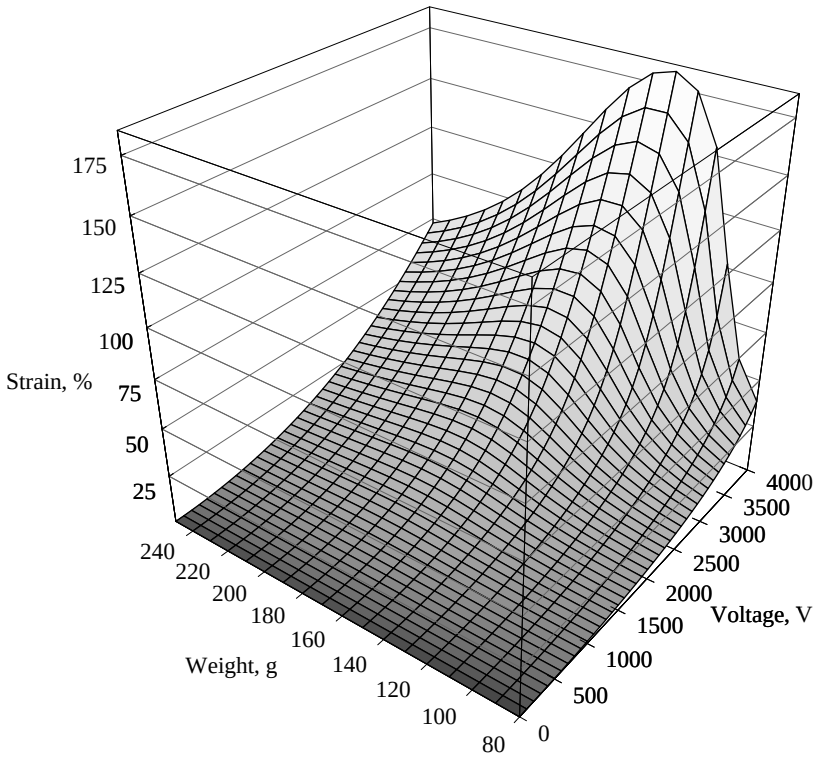

Figure 6.12: Plot of the modelled engineering strain for a VHB™4910 actuator, pre-strain in width direction was 300%.

ues, for instance the maximum strain is 182%, more than three times higher than measured. The strain at 400 V for the 80 g curve is twice the measured value. Of course, it does not display the wrinkle actuation mode, since this feature is not included in the model. The peak strain lies at a value of 130 g, which is close to the measured value.

If the Maxwell stress component of the model was multiplied with 0.48 (figure 6.13), the model returns a nearly exact match with the experimental

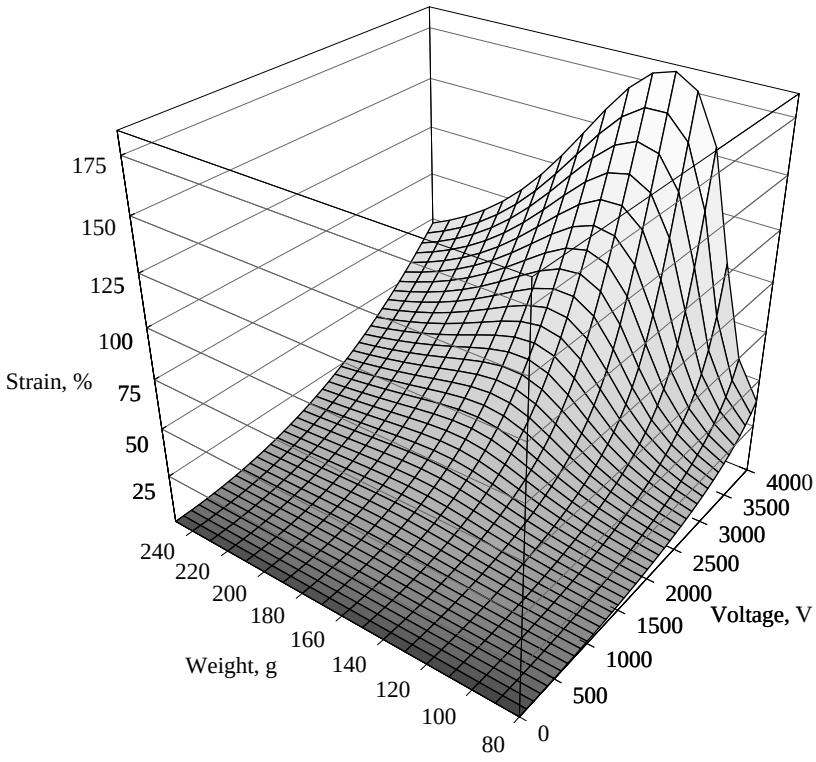

Figure 6.13: Modelled engineering strain of a VHB™4910 actuator, pre-strain in width direction was 300%. The Maxwell stress part of the model was multiplied with 0.5.

data. The factor can be justified by the same arguments as in section 6.2, in which the efficiency of the actuators blocking was lowered, because some of the actuation stress was channelled in the transversal direction. The efficiency measured in section 6.2 was 87% for the actuator in the 300% length pre-strain configuration, and 76% for 500% length pre-strain. Here the efficiency is down to 48%, a lowering which is harder to explain.

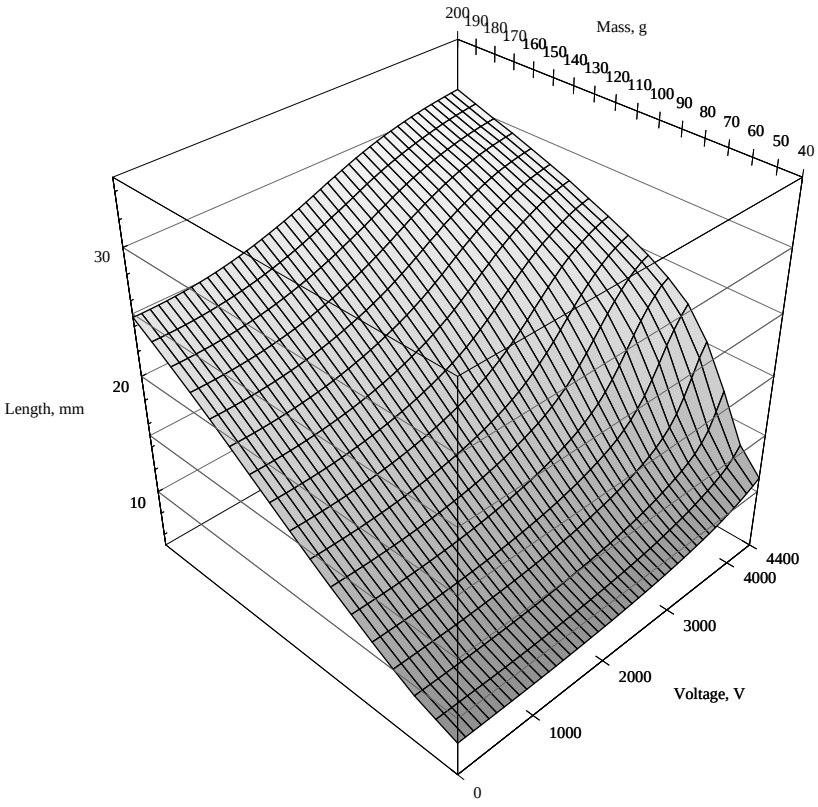

Figure 6.14: Actuated length of a VHB™4910 actuator, for which the pre-strain in the width direction was 400%.

6.5.2 Width pre-strain 400%

A VHB™4910 actuator was built with a pre-strain in the width direction of 400%. The measured actuation lengths are plotted in figure 6.14. The applied voltage was varied between 0–4400 V, and the applied weight was varied between 40–200 g. The maximum length is lower for the actuator with 400% width pre-strain than for the 300% width pre-strain actuator, mainly because

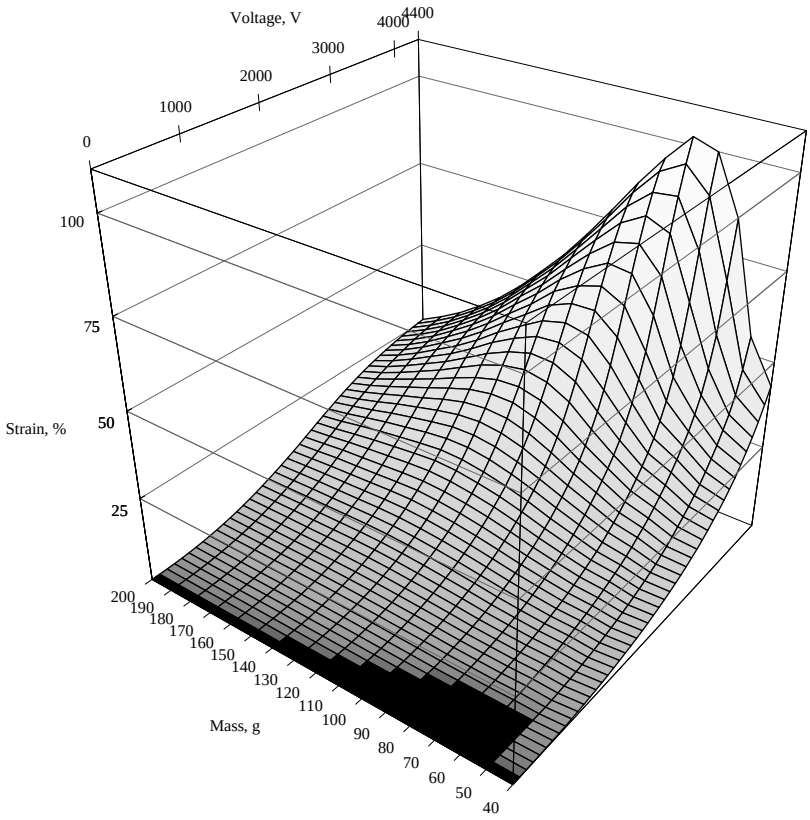

Figure 6.15: Engineering strain plotted for the VHB™4910 actuator, which was pre-strained 400% in width direction. The maximum strain was 76.1% at 4000 V, and 102% at 4400 V.

the applied weights are lower.

The engineering strain, calculated from the actuated length, is plotted in figure 6.15. The maximum strain at 4000 V is 76.1%, and lies at an applied weight of 90 g. At 4400 V, the maximum strain is 102.2%, and now lies at an applied weight of 80 g.

The maximum strain at a given voltage depends rather much on the ap-

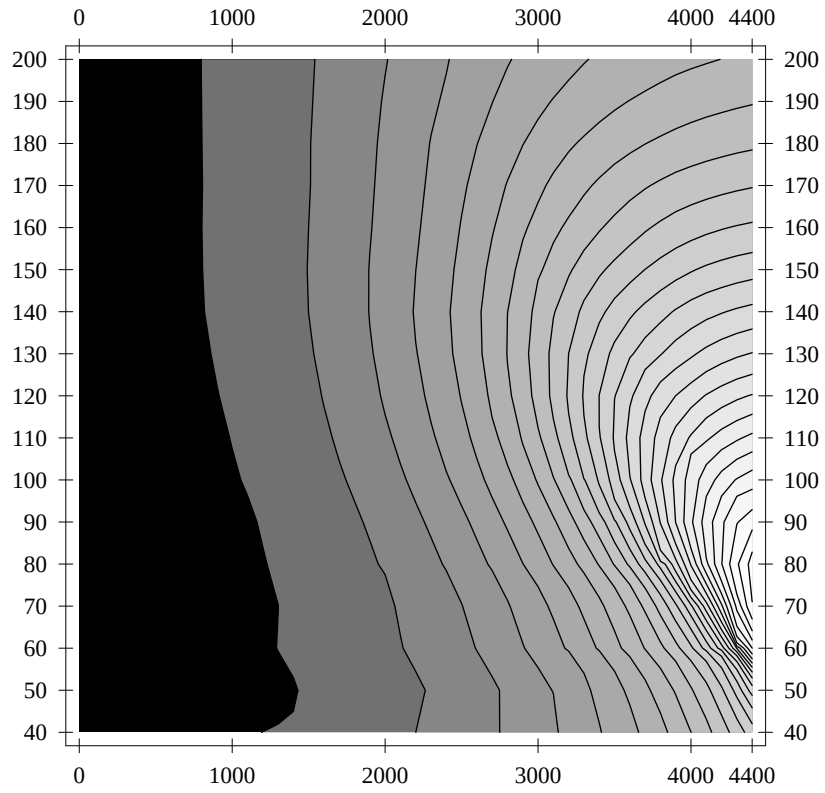

Figure 6.16: Contour surface of the VHB™4910 actuator, for which the pre-strain in width direction was 400%. Notice the shift in the position of maximum strain as the voltage is increased.

plied weight. The shift is easily seen in the contour plot of the engineering strain, figure 6.16. At 2000 V, the maximum lies at an applied weight of $\sim$ 145 g, at 3000 V it lies at $\sim$ 130 g, and at 3500 V it is down to $\sim$ 115 g.

Again, it was attempted to model the actuator. When inserting the parameters for the actuator, the resulting maximum strain at 4400 V was 522%, and was found for an applied weight of 50 g, which is far from the measured op-

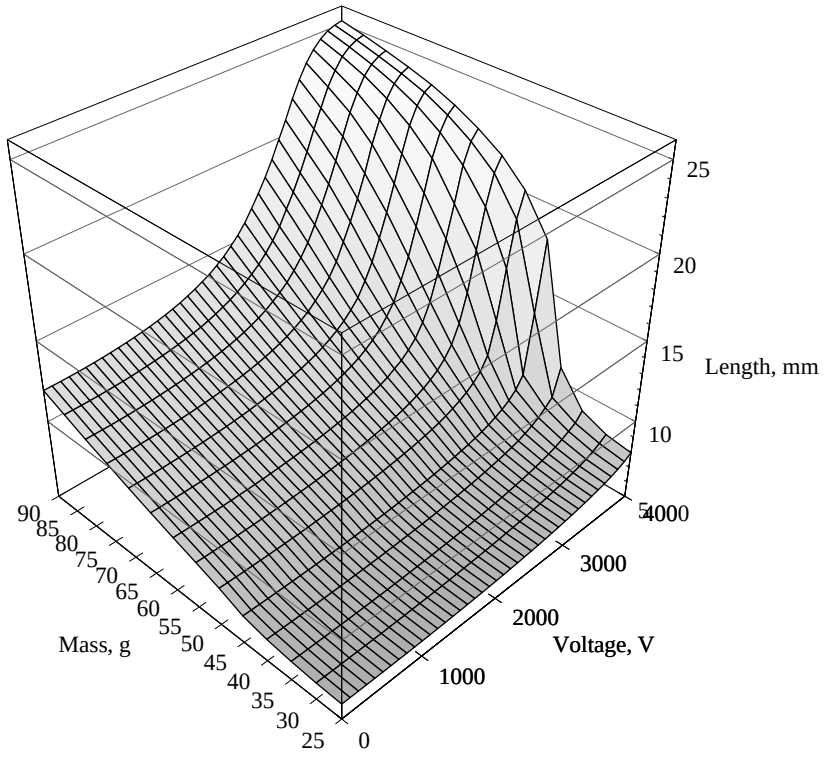

Figure 6.17: Actuated lengths of VHB™4910 actuator, for which the pre-strain in width direction was 500%.

timum value of 90 g. Introducing an efficiency parameter of 48% returned a maximum strain of 102%, lying at an applied weight of 130 g. It seems that the model does not apply well to this actuator.

6.5.3 Width pre-strain 500%

The measured length under actuation, obtained on an actuator with a pre-strain of 500% in width, is presented in figure 6.17. Voltages were varied between 0–4000 V, and applied weights were varied between 25–90 g, now in steps of 5 g. The appearance of this actuated length 'surface' differs much from those previously presented, since the length increases rapidly for voltages between 3000 V and 4000 V.

The surface gradient becomes quite small in the area of high voltage and applied weight. In this area, the strain is evidently hindered by the increase in elastic stress for high strains, figure 6.1. The actuator is most 'dynamic' in the high gradient region of the actuated length plot. In use, the actuator could advantageously be biased with a voltage of 3000 V, by which the length would vary rapidly in a small region of applied voltage.

The engineering strain, presented in figure 6.18, varies rapidly with both the applied voltage and the applied weight. The maximum engineering strain is 173%, obtained at a voltage of 4000 V, and an applied weight of 55 g. In moving along the iso-voltage curve of 4000 V, the output engineering strain varies from 35% to 173% for a 50% increase in applied weight. This signifies the importance of locating the optimum applied weight for a given DEA.

The results of applying the parameters of this actuator to the model are not presented, since the engineering strain in the model diverges for voltages above 3000 V. The extreme performance of this actuator probably can't be captured in this simple model.

Several reasons for the shortcoming of the model can be given. Since the model fit so well with the output of the silicone actuator, the reasons for the shortcoming of the model with respect to VHB™4910 actuators must be found in the properties that differ between the two. First, the VHB™4910 material displays a very large component of visco-elasticity loss. In principle, the time-dependent strain should be measured, and the whole stress-strain history of the actuator should taken into account. Second, the force from the reinforcing strips on the sides of the actuator, used to keep the actuating area somewhat rectangular, have not been included in the model. The effect of this is of course minor, because the Ogden model is fitted to the measured force-strain curve of the actuator. Third, the pre-strain enters the model only through the thickness of the actuator – it is likely that first-order effects are introduced, which are not included in the model either. The pre-strain is likely to mediate channelling of the actuation force transversally to the output direction.

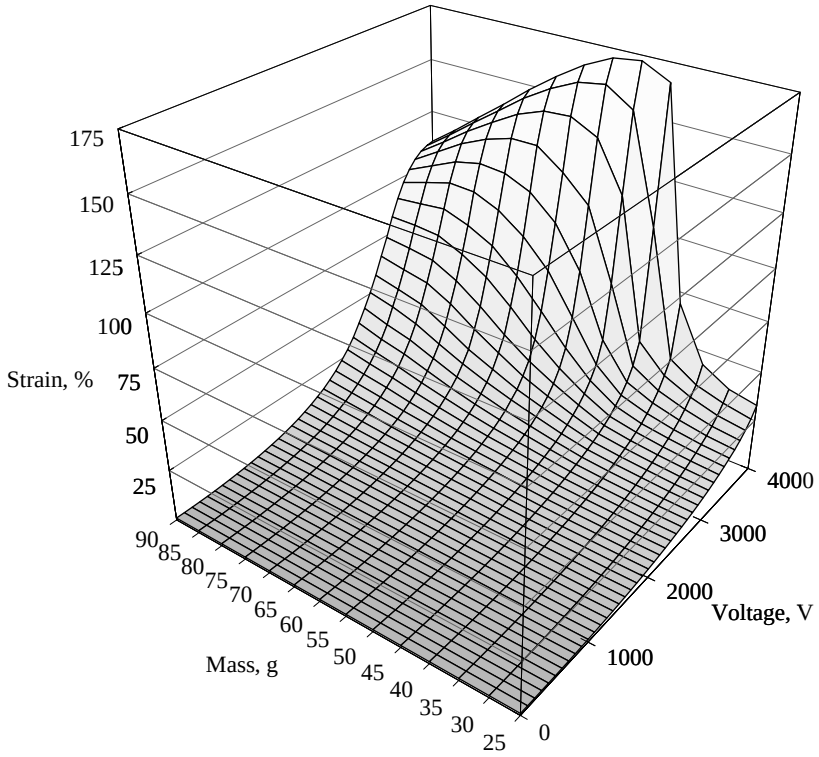

Figure 6.18: Plot of the engineering strain of the VHB™4910 actuator, for which the pre-strain in width was 500%. The maximum engineering strain was 173%, at an applied weight of 55 g.

7

Conclusion

Stress and strain have been introduced as tensor properties. Several theoretical models of stress-strain behavior were presented, of which the Ogden model was capable of fitting the observed behaviour in the entire range of measurement. Dielectricity was defined, and Maxwell stress was derived. The connection between Maxwell stress and electrostriction was described; both depend on the electric field to the second order. The theories of elasticity and Maxwell stress were combined, in the special case of a DEA constrained in the width direction.

Percolation properties were introduced, and an experiment was presented, in which the fraction of conducting graphite in insulating silicone rubber was varied. The results were of poor quality, still a distinct sign of percolation was observed: the conductivity at zero frequency exhibited a large jump at 23% volume fraction.

Mixtures of conducting carbon black in insulating polymer were developed, for use as compliant electrodes. For producing stable electrodes, a system of one-component silicone glue and Ketjenblack suspended in heptane was developed. This mixture was sprayed on pre-strained silicone elastomer films, providing stable compliant electrodes.

Procedures for manufacturing of DEA with two kinds of elastomer film were developed. Handling of thin silicone elastomer films is possible if temporary frames are used; these are cut away in the final manufacturing step. The manufacture and handling of VHB™4910 actuators is easier, since the film itself provides gluing, such that frames and electrodes are very easy to apply. These DEA structures are simple, making it easier to describe them theoretically.

Force-strain measurements were obtained using the actuator test bench. For a silicone actuator, the force-strain curve included artefacts of the additional stress from the compliant electrodes. Introducing a cut-off function, similar to the Fermi-Dirac distribution function, it was possible to fit the force-strain curve in the whole range of strain.

The blocking force of a VHB™4910 actuator was presented. The depen-

dence of the blocking force on applied voltage was parabolic, as expected from the Maxwell stress equation. Discrepancies were observed, which could not be explained through the model. In order of increasing length pre-strain, the 'efficiency' was 87%, 81%, and 76%. It was suggested that the efficiency factor should be explained by a channelling of the developed actuation stress in the transversal direction.

Measurements of electric breakdown strength of pre-strained VHB™4910 were presented, for isotropic pre-strains. The electric breakdown strength was shown to be near inversely proportional to the thickness of the stretched elastomer, increasing from 17 MV/m to 270 MV/m. An explanation of the increase involving a 'grid effect' was suggested: the polymer chains constituting the elastomer film are stretched out to form a grid, which would have a high cross-section for collision with ions accelerated by the applied electric field. This effect would increase with strain.

The actuator test bench was programmed to simulate a constant applied weight through force feedback. An automated data collection program was written, in order to vary the applied voltage and weight in a pre-defined grid. The resulting actuated lengths were obtained on a DEA. The actuated lengths were plotted in 3D-plots, to produce nicely interconnected plot surfaces, an indication of how well the actuator test bench functions. The 'engineering strain' was defined, as the strain measured at a given mass, with the reference length taken to be the length measured at zero applied voltage.

Measurements were performed on a silicone elastomer actuator. A pronounced peak was observed in the engineering strain, stating the fact that there is an optimum applied weight at which the highest actuated strain is found. The parameters of the silicone actuator were inserted in the derived model, and quantitative correspondence was found.

Measurements were also obtained on three VHB™4910 actuators. The pre-strain in width was 300%, 400%, and 500%. In order of increasing pre-strain, the maximum engineering strains were 53%, 76%, and 173%, which is very high, considering the voltage was limited to 4000 V. The applied weight corresponding to the peak value was seen to change between actuators. Even for a specific actuator, the optimum applied weight shifts with voltage. The derived model did not work well for any of the VHB™4910 actuators. It was possible to fit the results from the 300% width pre-strain actuator, by introducing an efficiency of 48% on the Maxwell stress. This strategy was not successful for the higher pre-strain actuators. It is concluded that inclusion of the width pre-strain in the model is necessary for predicting the response of the VHB™4910

actuators.

It has been shown in this thesis, that pre-strain influences the performance of a DEA profoundly. The pre-strain can be applied in two directions: in the width direction, and in the length. In the width direction, pre-strain is obtained in the manufacturing process, while in the length direction, pre-strain is obtained by loading the DEA with an applied weight. Pre-strain raises the electric breakdown field. In addition, pre-strain thins the film, such that the electric field is increased for the same applied voltage. Furthermore, pre-strain increases the actuation pressure.

With proper choice of actuator dimensions, it is possible to match the actuator exactly to its working environment. For VHB™4910 actuators, the optimum pre-strain may be found through measurement techniques, which have been presented in this thesis. For silicone actuators, the matching can be facilitated with the developed model.

Appendix A

The stress tensor

Generally, stress is a tensor property. On every surface in a body the stress can be split up in a component, which is normal to the plane, and two (perpendicular) components in the plane. These components are known as the tensile stress and the shear stress components, respectively. The stress configuration in a body constitutes a *field*, such that the stress in one point is not necessarily the same as in the adjacent point. In this thesis the elements of the stress tensor are constants, but generally they are not independent of position.

The definitions and concepts in this appendix derive from three textbooks concerning elasticity, by authors Macosko [31], Chou and Pagano [53], and Varga [54].

A.1 The stress tensor

Stresses act on points in a body. To evaluate the stress, we cut the point P with a plane, the normal of which is $\hat{\boldsymbol{n}}$. If forces act on the body, a force $\boldsymbol{f}_n$ will act on the plane, which is generally not in the same direction as $\hat{\boldsymbol{n}}$. This force is divided by a small area $d\boldsymbol{a}$ of the cut plane around P, resulting in a stress *vector* per unit area, $\boldsymbol{\sigma}_n$. To recapitulate, $\boldsymbol{\sigma}_n$ is the total stress on the plane with normal vector $\hat{\boldsymbol{n}}$ in the point P. Thus, if we move in the $\hat{\boldsymbol{n}}$-plane a distance from P, $\boldsymbol{\sigma}_n$ will generally be different.

The force on the $\hat{\boldsymbol{n}}$-plane is equal to the force on each of the planes $\hat{\boldsymbol{x}}$, $\hat{\boldsymbol{y}}$, and $\hat{\boldsymbol{z}}$, because the force has to balance in equilibrium. This is written as

$$a_n\boldsymbol{\sigma}_n = a_x\boldsymbol{\sigma}_x + a_y\boldsymbol{\sigma}_y + a_z\boldsymbol{\sigma}_z$$

where a_n is a small area in the $\hat{\boldsymbol{n}}$-plane, and a_x, a_x, and a_x are the projections of this area on the $\hat{\boldsymbol{x}}$, $\hat{\boldsymbol{y}}$, and $\hat{\boldsymbol{z}}$-planes, i.e. $a_x = a_n\hat{\boldsymbol{n}} \cdot \hat{\boldsymbol{x}}$. Written out this becomes

$$a_n\boldsymbol{\sigma}_n = (a_n\hat{\boldsymbol{n}} \cdot \hat{\boldsymbol{x}})\boldsymbol{\sigma}_x + (a_n\hat{\boldsymbol{n}} \cdot \hat{\boldsymbol{y}})\boldsymbol{\sigma}_y + (a_n\hat{\boldsymbol{n}} \cdot \hat{\boldsymbol{z}})\boldsymbol{\sigma}_z$$

Dividing by a_n

$$\boldsymbol{\sigma}_n = \hat{\boldsymbol{n}} \cdot [\hat{\boldsymbol{x}}\boldsymbol{\sigma}_x + \hat{\boldsymbol{y}}\boldsymbol{\sigma}_y + \hat{\boldsymbol{z}}\boldsymbol{\sigma}_z]$$

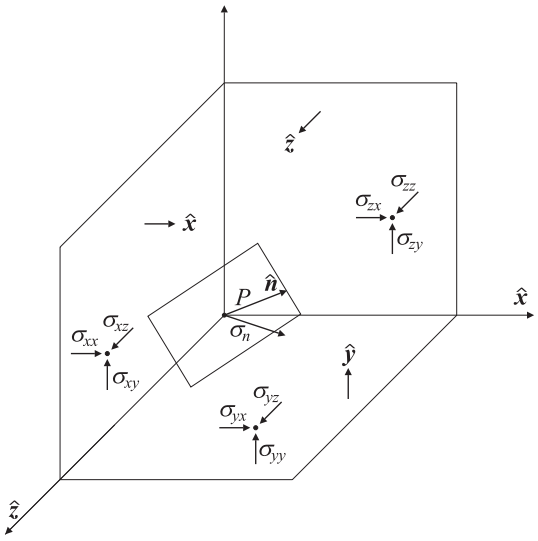

Figure A.1: Components of stress tensor.

$\hat{\boldsymbol{x}}\boldsymbol{\sigma}_x$, $\hat{\boldsymbol{y}}\boldsymbol{\sigma}_y$, and $\hat{\boldsymbol{z}}\boldsymbol{\sigma}_z$ are known as vector *dyads*. A dyad carries two directions, the first is normal to the plane that the stress vector works on, the second the direction of the stress vector itself.

In figure A.1 the components of the stress in each plane are pictured, e.g. in the $\hat{\boldsymbol{x}}$-plane the stress is $\boldsymbol{\sigma}_x = \hat{\boldsymbol{x}}\sigma_{xx} + \hat{\boldsymbol{y}}\sigma_{xy} + \hat{\boldsymbol{z}}\sigma_{xz}$ in order to account for both tensile and shear stresses. The stress vector $\boldsymbol{\sigma}_n$ in the $\hat{\boldsymbol{n}}$-plane can then be written as

$$\begin{aligned}\boldsymbol{\sigma}_n = \hat{\boldsymbol{n}} \cdot [\quad & \hat{\boldsymbol{x}}\hat{\boldsymbol{x}}\sigma_{xx} + \hat{\boldsymbol{x}}\hat{\boldsymbol{y}}\sigma_{xy} + \hat{\boldsymbol{x}}\hat{\boldsymbol{z}}\sigma_{xz} \\ & + \hat{\boldsymbol{y}}\hat{\boldsymbol{x}}\sigma_{yx} + \hat{\boldsymbol{y}}\hat{\boldsymbol{y}}\sigma_{yy} + \hat{\boldsymbol{y}}\hat{\boldsymbol{z}}\sigma_{yz} \\ & + \hat{\boldsymbol{z}}\hat{\boldsymbol{x}}\sigma_{zx} + \hat{\boldsymbol{z}}\hat{\boldsymbol{y}}\sigma_{zy} + \hat{\boldsymbol{z}}\hat{\boldsymbol{z}}\sigma_{zz} \quad]\end{aligned}$$

The parenthesis is known as a tensor, the *stress* tensor. It is written in the following way, in which the unit dyads are understood

$$\boldsymbol{\sigma} = \begin{bmatrix} \sigma_{xx} & \sigma_{xy} & \sigma_{xz} \\ \sigma_{yx} & \sigma_{yy} & \sigma_{yz} \\ \sigma_{zx} & \sigma_{zy} & \sigma_{zz} \end{bmatrix}$$

by which the stress vector is conveniently written as

$$\boldsymbol{\sigma}_n = \hat{\boldsymbol{n}} \cdot \boldsymbol{\sigma}$$

To improve on the notation, numbered coordinates are used to designate the axes, i.e. $\hat{\boldsymbol{x}}$, $\hat{\boldsymbol{y}}$, and $\hat{\boldsymbol{z}}$, are replaced by $\hat{\boldsymbol{x}}_1$, $\hat{\boldsymbol{x}}_2$, and $\hat{\boldsymbol{x}}_3$, as this will prove convenient. In the numbered coordinate representation, the whole stress tensor is designated by σ_{ij} instead of $\boldsymbol{\sigma}$, thus

$$\sigma_{ij} = \begin{bmatrix} \sigma_{11} & \sigma_{12} & \sigma_{13} \\ \sigma_{21} & \sigma_{22} & \sigma_{23} \\ \sigma_{31} & \sigma_{32} & \sigma_{33} \end{bmatrix}$$

and again the unit dyads $\hat{\boldsymbol{x}}_i\hat{\boldsymbol{x}}_j$ are understood.

The whole stress tensor is represented by σ_{ij}, where both indices i and j are summed from 1 to 3, returning all nine components, multiplied by their respective dyad. This is written explicitly as

$$\boldsymbol{\sigma} = \sum_{i=1}^{3}\sum_{j=1}^{3} \hat{\boldsymbol{x}}_i\,\hat{\boldsymbol{x}}_j\,\sigma_{ij}$$

With this notation, many of the vector and tensor operations can be written in a much simpler way. A further simplification of the written formulae is achieved when use is made of Einstein's implicit summation scheme. When one index is repeated, a summation over the full range of the index is understood (as in e.g. $\sigma_{ii} = \sigma_{11} + \sigma_{22} + \sigma_{33}$).

$$\begin{aligned}
\boldsymbol{a} &= \sum_{i=1}^{3} \hat{\boldsymbol{x}}_i a_i = a_i \\
\boldsymbol{\sigma} &= \sum_{i=1}^{3}\sum_{j=1}^{3} \hat{\boldsymbol{x}}_i\,\hat{\boldsymbol{x}}_j\,\sigma_{ij} = \sigma_{ij} \\
\hat{\boldsymbol{n}} \cdot \boldsymbol{a} &= \sum_{i=1}^{3} \hat{n}_i a_i = \hat{n}_i a_i \\
\hat{\boldsymbol{n}} \cdot \boldsymbol{\sigma} &= \sum_{i=1}^{3} \hat{\boldsymbol{x}}_i \sum_{j=1}^{3} \hat{n}_j \sigma_{ji} = \hat{n}_j \sigma_{ji} = \hat{n}_i \sigma_{ij}
\end{aligned}$$

Using these definitions, some of the above results are restated in the following. The stress (traction) vector $\boldsymbol{\sigma}_n$ on the $\hat{\boldsymbol{n}}$-plane is written as

$$\boldsymbol{\sigma}_n = \sigma_j^n = \hat{\boldsymbol{n}} \cdot \boldsymbol{\sigma} = \hat{n}_i \sigma_{ij}$$

The component of the traction vector in the direction of the $\hat{\boldsymbol{n}}$-vector is

$$\sigma_{nn} = \hat{\boldsymbol{n}} \cdot \boldsymbol{\sigma} \cdot \hat{\boldsymbol{n}} = \hat{n}_i \sigma_{ij} \hat{n}_j$$

The stress tensor is symmetric, thus it is equal to its transpose

$$\boldsymbol{\sigma} = \boldsymbol{\sigma}^T \qquad \Leftrightarrow \qquad \sigma_{ij} = \sigma_{ji}$$

The identity matrix, with elements 1 in the diagonal and 0 elsewhere is written using the Kronecker delta

$$\mathbf{I} = \delta_{ij}$$

This tensor is used to describe the situation when the stress is determined only by the pressure p of the surroundings

$$\boldsymbol{T} = -p\,\mathbf{I} \qquad \Leftrightarrow \qquad T_{ij} = -p\,\delta_{ij}$$

A.2 Principal stresses and invariants

It is always possible to construct a plane through a body under stress, such that only a single normal stress acts on the plane. The plane is known as a *principal* plane, and the normal stress on the plane is known as a *principal* stress. In fact, there are three such planes through any point in the body, and three corresponding stress vectors. In going from one point to the next, the principal planes and stress are not necessarily the same. The principal stresses are mutually perpendicular. Therefore, if the coordinate system is lined up with the principal stress vectors, the resulting principal stress tensor is diagonal

$$T_{ij}^p = \begin{bmatrix} \sigma_1 & 0 & 0 \\ 0 & \sigma_2 & 0 \\ 0 & 0 & \sigma_3 \end{bmatrix}$$

The stress vector and the normal vector of a principal plane are in the same direction,

$$\sigma_i^n = \sigma\, n_i$$

where σ is the magnitude of the stress vector σ_i. Since $\sigma_i^n = n_i T_{ij}$, the search for the principle stresses and their magnitudes is fulfilled by solving the eigenvalue problem

$$\begin{aligned} & \sigma_i^n = n_i T_{ij} = \sigma\, n_i \\ \Leftrightarrow \quad & n_i (T_{ij} - \sigma\, \delta_{ij}) = 0 \end{aligned}$$

Since n_i is not zero, $(T_{ij} - \sigma\, \delta_{ij})$ has to be. The solution of this can be found by setting up the characteristic equation,

$$\begin{aligned} & \det(T_{ij} - \sigma\, \delta_{ij}) = 0 \\ \Leftrightarrow \quad & \sigma^3 - I_1^T \sigma^2 + I_2^T \sigma - I_3^T = 0 \end{aligned}$$

The roots σ_i of this equation fulfil the following equations, which are invariants of the characteristic equation

$$\begin{aligned} I_1^T &= T_{ii} = \sigma_1 + \sigma_2 + \sigma_3 \qquad I_2^T = \frac{1}{2}\left[(T_{ii})^2 - (T^2)_{ii} \right] = \sigma_1\sigma_2 + \sigma_1\sigma_3 + \sigma_2\sigma_3 \\ I_3^T &= \det T_{ij} = \sigma_1\sigma_2\sigma_3 \end{aligned}$$

The invariants of the characteristic equation are named so, because they retain the same value in whichever coordinate system is used. Linear combinations of these invariants are also invariant.

A.3 Finite deformation tensors

For finite deformations we define a tensor, w_{ij}, connecting a reference state x_i' with the current state x_i. The tensor is known as the *deformation gradient* tensor, the action of which is to 'differentiate' the current state with respect to the reference state. It is thus assumed that the current state can be written as a continuous function of the reference state, $\boldsymbol{x} = \boldsymbol{x}(\boldsymbol{x}', t)$

$$\begin{aligned} \mathbf{W} = \boldsymbol{\nabla}' \boldsymbol{x} &= \frac{\partial \boldsymbol{x}}{\partial \boldsymbol{x}'} \\ w_{ij} &= \frac{\partial x_i}{\partial x_j'} \end{aligned}$$

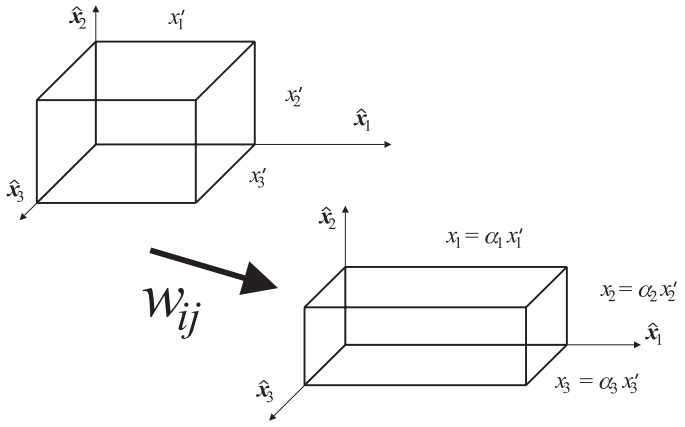

Figure A.2: Uniaxial deformation.

In figure A.2 the uniaxial deformation of a cube is illustrated. The displacement functions are

$$\begin{aligned} x_1 &= \alpha_1 x_1' \\ x_2 &= \alpha_2 x_2' \\ x_3 &= \alpha_3 x_3' \end{aligned}$$

describing the deformation of the cube from the reference (primed) state to the present state. The deformation gradient tensor describing this deformation is then

$$\mathbf{W} = w_{ij} = \frac{\partial x_i}{\partial x_j'} = \begin{bmatrix} \alpha_1 & 0 & 0 \\ 0 & \alpha_2 & 0 \\ 0 & 0 & \alpha_3 \end{bmatrix}$$

This is a diagonal tensor.

There are various bounds on the expansion ratios, α_i, which can be used to simplify the deformation gradient tensor. The uni-axial deformation of figure A.2 takes place with rotational symmetry about the $\hat{\boldsymbol{x}}_1$-axis, then $\alpha_2 = \alpha_3$. Also, we assume that the cube is incompressible, which is a good approxima-

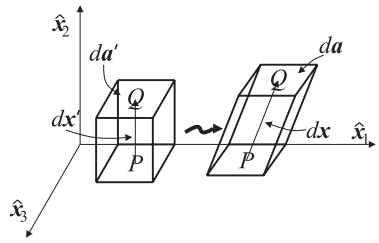

Figure A.3: An illustration of the physical description underlying the Finger tensor.

tion for elastomers. Then

$$\alpha_1\alpha_2\alpha_3 = 1 \quad \Leftrightarrow \quad \alpha_1 = \frac{1}{\alpha_2\alpha_3} = \frac{1}{\alpha_2^2} \quad \Leftrightarrow \quad \alpha_2 = \frac{1}{\sqrt{\alpha_1}}$$

The deformation gradient may then be written as

$$w_{ij} = \begin{bmatrix} \alpha_1 & 0 & 0 \\ 0 & \frac{1}{\sqrt{\alpha_1}} & 0 \\ 0 & 0 & \frac{1}{\sqrt{\alpha_1}} \end{bmatrix}$$

The finger tensor is defined from the deformation gradient tensor as

$$\mathbf{B} = \mathbf{W} \cdot \mathbf{W}^T \qquad \Leftrightarrow \qquad B_{ij} = w_{ik}w_{jk}$$

The Finger tensor describes the local area change. This can be elucidated by constructing a specific measure of the local area change, μ, of a small area element $d\boldsymbol{a}'$. In figure A.3 a deformation has been illustrated. The deformation gradient connects the present state with the past state through $d\boldsymbol{x} = \mathbf{W} \cdot d\boldsymbol{x}'$. Since the material is incompressible, $d\boldsymbol{a}' \cdot d\boldsymbol{x}' = d\boldsymbol{a} \cdot d\boldsymbol{x}$, thus

$$d\boldsymbol{a}' = d\boldsymbol{a} \cdot \frac{d\boldsymbol{x}}{d\boldsymbol{x}'} = d\boldsymbol{a} \cdot \mathbf{W}$$

The relative local area change squared is then evaluated as

$$\mu^2 = \frac{d\boldsymbol{a}' \cdot d\boldsymbol{a}'}{d\boldsymbol{a} \cdot d\boldsymbol{a}} = \frac{(d\boldsymbol{a} \cdot \mathbf{W}) \cdot (d\boldsymbol{a} \cdot \mathbf{W})}{|d\boldsymbol{a}|^2} = \frac{d\boldsymbol{a} \cdot (\mathbf{W} \cdot \mathbf{W}^T) \cdot d\boldsymbol{a}}{|d\boldsymbol{a}| \cdot |d\boldsymbol{a}|} = \frac{d\boldsymbol{a} \cdot \mathbf{B} \cdot d\boldsymbol{a}}{|d\boldsymbol{a}| \cdot |d\boldsymbol{a}|}$$

The unit normal of $d\boldsymbol{a}$ is written as $\hat{\boldsymbol{n}} = \frac{d\boldsymbol{a}}{|d\boldsymbol{a}|}$, by which the above reduces to

$$\mu^2 = \hat{\boldsymbol{n}} \cdot \mathbf{B} \cdot \hat{\boldsymbol{n}}$$

The deformation gradient for a uniaxial extension is diagonal, thus the Finger tensor is

$$B_{ij} = \begin{bmatrix} \alpha_1^2 & 0 & 0 \\ 0 & \frac{1}{\alpha_1} & 0 \\ 0 & 0 & \frac{1}{\alpha_1} \end{bmatrix} \qquad \left(B_{ij}^2 = \begin{bmatrix} \alpha_1^4 & 0 & 0 \\ 0 & \frac{1}{\alpha_1^2} & 0 \\ 0 & 0 & \frac{1}{\alpha_1^2} \end{bmatrix} \right)$$

When there is no deformation, the Finger tensor is unity,

$$\mathbf{B} = \mathbf{I} \qquad \Leftrightarrow \qquad B_{ij} = \delta_{ij}$$

The strain tensor can be derived from the Finger tensor as

$$\boldsymbol{\varepsilon} = \mathbf{B} - \mathbf{I} \qquad \Leftrightarrow \qquad \varepsilon_{ij} = B_{ij} - \delta_{ij}$$

All elements of the strain tensor are zero when there is no deformation.

The invariants of the Finger tensor are calculated using the set of invariants defined for the stress tensor above,

$$\begin{aligned} I_1^B &= B_{ii} = \alpha_1^2 + \alpha_2^2 + \alpha_3^2 \\ I_2^B &= \frac{1}{2}\left[(B_{ii})^2 - (B^2)_{ii}\right] = \alpha_1^2\alpha_2^2 + \alpha_2^2\alpha_3^2 + \alpha_1^2\alpha_3^2 = \frac{1}{\alpha_1^2} + \frac{1}{\alpha_2^2} + \frac{1}{\alpha_3^2} \\ I_3^B &= \det B_{ij} = \alpha_1^2\alpha_2^2\alpha_3^2 \end{aligned}$$

For uniaxial extension, the invariants of the Finger tensor evaluate to

$$\begin{aligned} I_1^B &= \alpha_1^2 + \frac{2}{\alpha_1} \\ I_2^B &= 2\alpha_1 + \frac{1}{\alpha_1^2} \\ I_3^B &= \alpha_1^2\alpha_1^{-1}\alpha_1^{-1} = 1 \end{aligned}$$

Property	Scalar	Tensor
Stress	$p = \frac{f}{A}$	$\boldsymbol{\sigma}$, σ_{ij}
Total stress		$\mathbf{T}$, T_{ij}
Expansion ratio	α	$\mathbf{B}$, B_{ij}
Strain	ε	ε_{ij}
Dielectric constant	ϵ	ϵ_{ij}
Deformation gradient		$\mathbf{W} = \boldsymbol{\nabla}' \boldsymbol{x}$, $w_{ij} = \frac{\partial x_i}{\partial x'_j}$
Finger		$B_{ij} = w_{ik} w_{kj}$

Appendix B

Articles

Here follows reprints of the two articles published so far, to which this author has made active contributions.

Appendix C

Fit and model programs

After data was collected, it was analysed using Mathematica®3.0 procedures. First the analysis program for stress-strain measurements is presented. It should be mentioned that the programs were included as is, by which in many places Danish names for parameters are used. A short dictionary

Fejl: Error

Hele: All, entire

Kraft: Force

Laengde: Length

Nul: Zero

Nulpunkt: Zero point

C.1 Stress-strain measurements

The initial part of the program loads various packages.

```
<< Statistics`DataSmoothing`;
<< Statistics`LinearRegression`;
<< Graphics`MultipleListPlot`;
<< Statistics`NonlinearFit`;
```

Then the data is loaded.

```
Indfil = "c : /data/010608/E625 − electrodes2.txt";
Et = ReadList[Indfil, {Number, Number}];
UseTheseDataPoints = 9900; Dimensions[Et]
w1 = 0.000052; w2 = 0.045; f0 = 20.9; g = 9.82; Pick = 50;
```

Here the data are sorted, for later ease of treatment and plotting.

```
Laengde = Table[Et[[i, 1]], {i, UseTheseDataPoints}];
Strain = Table[(Laengde[[i]]/1000 − 10)/10,
   {i, UseTheseDataPoints}];
```

```
Kraft = Table[g(Et[[i,2]] - f0)/1000,
   {i,UseTheseDataPoints}];
StrainKraft = Table[{Strain[[i]],Kraft[[i]]},
   {i,UseTheseDataPoints}];
PickStrainKraft = Table[{Strain[[Pick i]],Kraft[[Pick i]]},
   {i,Length[Strain]/Pick}];l0
LaengdeKraft = Table[{Laengde[[i]] - l0 * 1000,Kraft[[i]]},
   {i,Length[Laengde]}];
PickLaengdeKraft = Table[LaengdeKraft[[Pick i]],
   {i,1,Length[LaengdeKraft]/Pick}];
HeleLaengdeKraft = Table[{Laengde[[i]],Kraft[[i]]},
   {i,Length[Laengde]}];
PickHeleLaengdeKraft = Table[HeleLaengdeKraft[[Pick i]],
   {i,Length[HeleLaengdeKraft]/Pick}];
ListPlot[PickHeleLaengdeKraft,PlotJoined->False,
   PlotStyle->{PointSize[.005]},
   PlotRange->{{14.5,15.8},{0,.1}},Frame->True,
   TextStyle->{FontFamily->"Times",FontSize->9},
   FrameLabel->{"Totallengthl,mm","Forcef,N"},
   ImageSize->{300,200}];
```

The above part returns the number of data points, the zero-strain length of the sample, and the defined zero-strain-length of the sample. The latter two generally differ, due to slack in the initial part of the measurement. The data are sorted into different two-column tables, for ease of handling later in the program. `Pick` is a number used to lower the number of data points when plotting the data. Here one in fifty data points are chosen for plotting.

Now the Hooke model is fitted, that is, a straight line is fitted to the first, linear part of the stress-strain curve.

```
Vindue = 10;Nulpunkt = 361;Mange = 10;
FitData = Table[Table[{Strain[[i]],Kraft[[i]]},
   {i,Nulpunkt,u + Nulpunkt + Vindue}],{u,Mange}];
Hfit = Table[Fit[FitData[[i]],{1,e},e],{i,Mange}];
KraftNulFejl = Table[Hfit[[i]][[1]]1000/g,{i,Mange}];
LaengdeNulFejl = Table[-Hfit[[i]][[1]]/Hfit[[i]][[2,1]],
   {i,Mange}];
KraftKonstantK = Table[Hfit[[i]][[2,1]]/l0,{i,Mange}];
TensileModulus = Table[Hfit[[i]][[2,1]]/(w1w2),
   {i,Mange}];
```

```
ListPlot[TensileModulus];
{L = Mean[LaengdeNulFejl] * 10 * 1000, P = Mean[KraftNulFejl],
   K = Mean[KraftKonstantK], G = Mean[TensileModulus]/3,
   Tensile = 3G}
```

The data is prepared for plotting, then plotted.

```
FitHooke = Table[{Laengde[([i])] - 10 * 1000,
   K/1000 * ((Laengde[([i])] - 10 * 1000))},
   {i, Length[Laengde]}];
PickFitHooke = Table[FitHooke[([Pick i])],
   {i, Length[FitHooke]/Pick}];
MultipleListPlot[PickLaengdeKraft, PickFitHooke,
   PlotJoined->{False, True}, PlotRange->{{0, 1}, {0, .2}},
   SymbolShape->{PlotSymbol[Box, .5, Filled->False], None},
   PlotStyle->{{}, {Thickness[0.001]}}, Frame->True,
   TextStyle->{FontFamily->"Times", FontSize->9},
   FrameLabel->{"Extensionlengthl - (10), mm",
   "Forcef, N"}, ImageSize->{300, 210}];
```

For an actuator, which is constrained in width, the Mooney-Rivlin and the Neo-Hookean models return the same force-strain behaviour. Therefore these fits are considered simultaneously.

```
Vindue = 2000; Nulpunkt = 250; Mange = 1;
FitData = Table[Table[{Strain[[i]], Kraft[[i]]/(w1 * w2)},
   {i, Nulpunkt, u + Nulpunkt + Vindue}], {u, Mange}];
Hfit = Table[Fit[FitData[[i]], {(1 - 1/(1 + e)^3)}, e], {i, Mange}];
G = Mean[Table[Hfit[[i]][[1, 1]], {i, Mange}]]/2;
StrainMR = Table[{Strain[[i]], w1 * w2 * G(1 + Strain[[i]] -
   1/(1 + Strain[[i]])^3)}, {i, Length[Strain]}];
PickStrainMR = Table[StrainMR[[Pick i]],
   {i, Length[StrainMR]/Pick}];
Error = Table[{PickStrainKraft[[i, 1]],
   Log[Abs[(PickStrainMR[[i, 2]] - PickStrainKraft[[i, 2]])/
   PickStrainKraft[[i, 2]]]]},
   {i, Length[PickStrainKraft]}];
ListPlot[Error];
```

The `Error` table is a measure of the difference between the data and the fit. The logarithm is taken, to facilitate easy plotting and visual inspection of the

fit. The resulting fit is plotted with the data, using an expression similar to the plot in the Hookean section.

The fitting of the Ogden expression can't be performed with the `Fit` routine, since the exponents may be non-integer. The routine `NonLinearRegress` is therefore used. It performs a non-linear fit, using special fitting routines, as described in the Help section of Mathematica. After fitting, it outputs the results, and a report on the (statistical) properties of the fit, such as the bounds on the obtained fit values. The presented routine is used for fitting of the silicone actuator with rubber electrodes, therefore the 'Fermi'-function is present too. First the value of `k1` is kept constant.

```
Fermi = 1/(1 + Exp[(0.65 - e)/.06]);
Ogden = mu1((1 + e)^(k1 - 1) - (1 + e)^(-k1 - 1))+
   Fermi * mu2((lamb(e + 1))^(k2 - 1) - (lamb(e + 1))^(-k2 - 1));
Vindue = 8850; Nulpunkt = 500;
kstart = 1.3;
FitData = Table[{Strain[[Pick i]], Kraft[[Pick i]]/(w1 * w2)},
   {i, Nulpunkt/Pick, (Nulpunkt + Vindue)/Pick}];
Ogdenfit = NonlinearRegress[FitData, Ogden/.k1->kstart, {e},
   {{mu1, 388000}, {mu2, 30299}, {k2, 5.78}, {lamb, 0.686}},
   ShowProgress->True, MaxIterations->200]
```

The fit continues by letting `k1` vary, and keeping `mu1` constant. The output values for the other parameters are used as seed parameters for the new run of the fitting routine. After this run, the fitting routine is run with `mu1` varying, and `k1` constant.

```
Ogdenfit1 = NonlinearRegress[FitData,
   Ogden/.Ogdenfit[[1, 2, 1]], {e},
   {{k1, kstart}, {mu2, Ogdenfit[[1, 2, 2, 2]]},
   {k2, Ogdenfit[[1, 2, 3, 2]]}, {lamb, Ogdenfit[[1, 2, 4, 2]]}},
   ShowProgress->True, MaxIterations->200]
Ogdenfit2 = NonlinearRegress[FitData,
   Ogden/.Ogdenfit1[[1, 2, 1]], {e},
   {{mu1, Ogdenfit[[1, 2, 1, 2]]}, {mu2, Ogdenfit1[[1, 2, 2, 2]]},
   {k2, Ogdenfit1[[1, 2, 3, 2]]}, {lamb, Ogdenfit1[[1, 2, 4, 2]]}},
   ShowProgress->True, MaxIterations->200]
```

This section of the program uses the same principle as the above, having either `k1` or `mu1` varying, while the other is constant. At this point the fitting

can be continued indefinitely, by running this part of the program again and again.

```
Ogdenfit1 = NonlinearRegress[FitData,
   Ogden/.Ogdenfit2[[1,2,1]],{e},
   {{k1,Ogdenfit1[[1,2,1,2]]},{mu2,Ogdenfit2[[1,2,2,2]]},
   {k2,Ogdenfit2[[1,2,3,2]]},{lamb,Ogdenfit2[[1,2,4,2]]}},
   ShowProgress->False,MaxIterations->200]
Ogdenfit2 = NonlinearRegress[FitData,
   Ogden/.Ogdenfit1[[1,2,1]],{e},
   {{mu1,Ogdenfit2[[1,2,1,2]]},{mu2,Ogdenfit1[[1,2,2,2]]},
   {k2,Ogdenfit1[[1,2,3,2]]},{lamb,Ogdenfit1[[1,2,4,2]]}},
   ShowProgress->False,MaxIterations->200]
```

In the final fitting sequence all parameters are allowed to vary, using the seed parameters obtained from the previous fits. The output is plotted for visual inspection of the validity of the obtained fit.

```
OgdenfitFinal = NonlinearRegress[FitData,Ogden,{e},
   {{mu1,Ogdenfit2[[1,2,1,2]]},{k1,Ogdenfit1[[1,2,1,2]]},
   {mu2,Ogdenfit2[[1,2,2,2]]},{k2,Ogdenfit2[[1,2,3,2]]},
   {lamb,Ogdenfit2[[1,2,4,2]]}},
   ShowProgress->True,MaxIterations->100];
StrainOgden = Table[{Strain[[i]],
   w1*w2*Ogden/.OgdenfitFinal[[1,2]]/.e->Strain[[i]]},
   {i,Length[Strain]}];
PickStrainOgden = Table[StrainOgden[[Pick i]],
   {i,Length[StrainOgden]/Pick}];
```

C.2 Actuator modelling

The actuator strain response for a given applied weight is modelled by inputting the force-strain behaviour, and using the theoretical Maxwell expression for evaluation of the actuation force. The resulting equilibrium strain is obtained using a Mathematica routine called `FindRoot`. First all physical parameters of the actuator are defined. The silicone actuator is chosen for this example.

```
<< Graphics'MultipleListPlot';
```

```
x3 = 0.000052; x2 = 0.045; w2 = 0.040; g0 = 9.82; l0 = 14.91/1000;
e0 = 8.85 * 10^-12; d = 2.3; eps = w2 * d * e0/x3;
mu1 = 358535; k1 = 1.407; mu2 = 34332; k2 = 5.739; lamb = 0.663;
G = 329944; knst = G * x2 * x3;
Mass = m * g0/1000;
Actuator = epsV^2 (1 + e);
Hooke = knst * e;
HookeStrain = (knst + Mass)/(knst - eps * V^2) - 1;
HookeEngStrain = 100 * eps * V^2/(knst - eps * V^2);
NeoHooke = knst * (1 + e - (1 + e)^-3);
NeoHookeKraft = Simplify[NeoHooke - Mass - Actuator];
Fermi = 1/(1 + Exp[(0.65 - e)/.06]);
Ogden = x2 * x3 * (mu1((1 + e)^(k1 - 1) - (1 + e)^(-k1 - 1)) +
   Fermi * mu2 * ((lamb * (e + 1))^(k2 - 1) - (lamb * (e + 1))^(-k2 - 1)));
Ogden = Simplify[Ogden];
m = 50;
NeoHookeKraft = Simplify[NeoHooke - Mass - Actuator];
OgdenKraft = Simplify[Ogden - Mass - Actuator];
NK = NeoHookeKraft;
OK = OgdenKraft;
Plot[{Fermi, Ogden, NeoHooke, Hooke}, {e, 0, 1.35}];
```

The last plot returns the force-strain behaviour of the models under evaluation.

The procedure `FindRoot` is employed for different values of applied voltage, from 0–3000 V.

```
Volt = Range[0, 3000, 25];
NS = Table[FindRoot[NK/.V- > Volt[[i]], {e, 1}][[1, 2]], {i, Length[Volt]}];
OS = Table[FindRoot[OK/.V- > Volt[[i]], {e, 1}][[1, 2]], {i, Length[Volt]}];
EHS = Table[{Volt[[i]], HookeEngStrain/.V- > Volt[[i]]},
   {i, Length[Volt]}];
ENS = Table[{Volt[[i]], 100(NS[[i]] - NS[[1]])/(NS[[1]] + 1)},
   {i, Length[Volt]}];
EOS = Table[{Volt[[i]], 100(OS[[i]] - OS[[1]])/(OS[[1]] + 1)},
   {i, Length[Volt]}];
MultipleListPlot[EHS, ENS, EOS, PlotStyle- > {Thickness[.001]},
   PlotJoined- > True, SymbolShape- > None, Frame- > True,
   PlotRange- > {{0, 3000}, {0, 20}},
   TextStyle- > {FontFamily- > "Times", FontSize- > 9},
```

```
FrameLabel->{"Voltage,V","Strain[Epsilon]"};
```

The resulting graph is presented in figure 3.5. The procedure was repeated for several applied masses, to produce figure 6.8.

References

[1] R. A. Anderson, "Mechanical stress in a dielectric solid from a uniform dielectric field", *Physical Review B* **33**(2), 1302–1307 (1986).

[2] M. Zhenyi, J. I. Scheinbeim, J. W. Lee, and B. A. Newman, "High field electrostrictive response of polymers", *Journal of Polymer Science: Part B: Polymer Physics* **32**, 2721–2731 (1994).

[3] K. Elhami, B. Gauthier-Manuel, J. F. Manceau, and F. Bastien, "Electrostriction of the copolymer of vinylidene-flouride and triflouroethylene", *Journal of Applied Physics* **77**(8), 3987–3990 (1995).

[4] V. Bharti, X.-Z. Zhao, Q. M. Zhang, R. Romotowski, F. Tito, and R. Ting, "Ultrahigh field induced strain and polarization response in electron irradiated poly(vinylidene flouride-triflouroethylene) copolymer", *Material Research Innovation* **2**, 57–63 (1998).

[5] Q. M. Zhang, V. Bharti, and X.-Z. Zhao, "Giant electrostriction and relaxor ferroelectric behavior in electron-irradiated poly(vinylidene flouride-triflouroethylene) copolymer", *Science* **280**, 2101–2104 (1998).

[6] X.-Z. Zhao, V. Bharti, Q. M. Zhang, T. Romotowski, F. Tito, and R. Ting, "Electromechanical properties of electrostrictive poly(vinylidene flouride-triflouroethylene) copolymer", *Applied Physics Letters* **73**(14), 2054–2056 (1998).

[7] Z.-Y. Cheng, V. Bharti, T.-B. Xu, H. Xu, T. Mai, and Q. M. Zhang, "Electrostrictive poly(vinylidene flouride-triflouroethylene) copolymers", *Sensors and Actuators A* **90**, 138–147 (2001).

[8] Y. Bar-Cohen, editor, *Proceedings of SPIE: Smart Structures and Materials 2001: Electroactive Polymer Actuators and Devices*, 4329, SPIE–The International Society for Optical Engineering, Newport Beach, USA, March 2001.

[9] Z.-Y. Cheng, H. S. Xu, T. Mai, M. Chung, and Q. M. Zhang, "P(VDF-TrFE)-based electrostrictive co/ter-polymers and its device performance", in *Smart Structures and Materials 2001: Electroactive Polymer Actu-*

ators and Devices, edited by Y. Bar-Cohen, Proceedings of SPIE, Vol. 4329, pages 106–116, 2001.

[10] R. Pelrine, R. Kornbluh, Q. Pei, and J. Joseph, "High-speed electrically actuated elastomers with strain greater than 100%", *Science* **287**, 836–839 (2000).

[11] T. Hirai, H. Sadatoh, T. Ueda, T. Kasazaki, Y. Kurita, M. Hirai, and S. Hayashi, "Polyurethane elastomer actuator", *Die Angewandte Makromolekulare Chemie* **240**, 221–229 (1996).

[12] Q. M. Zhang, J. Su, C. H. Kim, R. Ting, and R. Capps, "An experimental investigation of electromechanical responses in a polyurethane elastomer", *Journal of Applied Physics* **81**(6), 2770–2776 (1997).

[13] J. Su, Q. M. Zhang, and R. Ting, "Space-charge-enhanced electromechanical response in thin-film polyurethane elastomers", *Applied Physics Letters* **71**(3), 386–388 (1997).

[14] J. Su, Q. M. Zhang, C. H. Kim, R. Ting, and R. Capps, "Effects of transitional phenomena on the electric field induced strain-electrostrictive response of a segmented polyurethane elastomer", *Journal of Applied Polymer Science* **65**(7), 1363–1370 (1997).

[15] T. Ueda, T. Kasazaki, N. Kunitake, T. Hirai, J. Kyokane, and K. Yoshino, "Polyurethane elastomer actuator", *Synthetic Metals* **85**, 1415–1416 (1997).

[16] Y. M. Shkel and J. Klingenberg, Daniel, "Electrostriction of polarizable materials: Comparison of models with experimental data", *Journal of Applied Physics* **83**(1), 415–424 (1998).

[17] J. Su, Q. M. Zhang, P.-C. Wang, A. G. MacDiarmid, and K. J. Wynne, "Preparation and characterization of electrostrictive polyurethane films with conductive polymer electrodes", *Polymers for Advanced Technologies* **9**, 317–321 (1998).

[18] J. Kyokane, H. Ishimoto, H. Yugen, T. Hirai, T. Ueda, and K. Yoshino, "Polyurethane elastomer actuator", *Synthetic Metals* **103**, 2366–2367 (1999).

[19] R. Pelrine, R. Kornbluh, and J. Joseph, "Electrostriction of polymer dielectrics with compliant electrodes as a means of actuation", *Sensors and Actuators A* **64**, 77–85 (1998).

[20] R. Heydt, R. Kornbluh, R. Pelrine, and V. Mason, "Design and performance of an electrostrictive-polymer-film acoustic actuator", *Journal of Sound and Vibration* **215**(2), 297–311 (1998).

[21] R. Kornbluh, R. Pelrine, J. Joseph, R. Heydt, Q. Pei, and S. Chiba, "High-field electrostriction of elastomeric polymer dielectrics for actuation", in *Smart Structures and Materials 2001: Electroactive Polymer Actuators and Devices*, edited by Y. Bar-Cohen, pages 149–161, 1999.

[22] R. Pelrine, R. Kornbluh, J. Joseph, R. Heydt, Q. Pei, and S. Chiba, "High-field deformation of elastomeric dielectrics for actuators", *Materials Science and Engineering C* **11**, 89–100 (2000).

[23] R. Pelrine, R. Kornbluh, and G. Kofod, "High-strain actuator materials based on dielectric elastomers", *Advanced Materials* **12**(16), 1223–1225 (2000).

[24] R. Pelrine, P. Sommer-Larsen, R. Kornbluh, R. Heydt, G. Kofod, Q. Pei, and P. Gravesen, "Application of dielectric elastomer actuators", in *Smart Structures and Materials 2001: Electroactive Polymer Actuators and Devices*, edited by Y. Bar-Cohen, Proceedings of SPIE, Vol. 4329, pages 335–349, 2001.

[25] R. Kornbluh, R. Pelrine, and Q. Pei, "Dielectric elastomer produces strain of 380%", http://ndeaa.jpl.nasa.gov/nasa-nde/newsltr/WW-EAP_Newsletter2-2.PDF, December 2000.

[26] J. W. Jeon, K. C. Park, S. An, J. D. Nam, H. Choi, H. Kim, S. S. Bae, and Y. Tak, "Electrostrictive polymer actuators and their control systems", in *Smart Structures and Materials 2001: Electroactive Polymer Actuators and Devices*, edited by Y. Bar-Cohen, Proceedings of SPIE, Vol. 4329, pages 380–388, 2001.

[27] Y. Bar-Cohen, "Transition of EAP material from novelty to practical applications: are we there yet?", in *Smart Structures and Materials 2001: Electroactive Polymer Actuators and Devices*, edited by Y. Bar-Cohen, Proceedings of SPIE, Vol. 4329, pages 1–6, 2001.

[28] C. Melhuish and A. Adamatzky, "Biologically inspired robots", in *Smart Structures and Materials 2001: Electroactive Polymer Actuators and Devices*, edited by Y. Bar-Cohen, Proceedings of SPIE, Vol. 4329, pages 16–27, 2001.

[29] S. L. Rosen, *Fundamental principles of polymeric materials*, John Wiley and Sons, Inc., New York, 2nd edition, 1982.

[30] J. J. Aklonis and W. J. MacKnight, *Introduction to polymer viscoelasticity*, Wiley, New York, 2nd edition, 1983.

[31] C. W. Macosko, *Rheology: principles, measurements, and applications*, VCH. Publishers, Inc., New York, 1994.

[32] R. W. Ogden, "Large deformation isotropic elasticity - on the correlation of theory and experiment for incompressible rubberlike solids", *Proceedings of the Royal Society of London A* **326**, 565–584 (1972).

[33] H. Fröhlich, *Theory of dielectrics*, Oxford University Press, London, 2nd edition, 1958.

[34] S. Havriliak, Jr and S. J. Havriliak, "Dielectric relaxation parameters for polymers", in *Physical properties of polymers handbook*, edited by J. E. Mark, chapter 36, AIP Press, Woodbury, New York, 1996.

[35] N. G. McCrum, B. E. Read, and G. Williams, *Anelastic and dielectric effects in polymeric solids*, Dover, New York, 1967.

[36] J. A. Stratton, *Electromagnetic theory*, McGraw-Hill Book Company, Inc., London, 1941.

[37] R. E. Newnham, V. Sundar, R. Yimnirun, J. Su, and Q. M. Zhang, "Electrostriction: Nonlinear electromechanical coupling in solid dielectrics", *Journal of Physical Chemistry B* **101**, 10141–10150 (1997).

[38] V. Sundar and R. E. Newnham, "Electrostriction and polarization", *Ferroelectrics* **135**, 431–446 (1992).

[39] G. Kloos, "Relation of the electrostrictive coefficents of a non-ionic isotropic dielectric to other material constants", *Journal of Physics D: Applied Physics* **28**, 1680–1686 (1995).

[40] I. Krakovský, T. Romijn, and A. P. de Boer, "A few remarks on the electrostriction of polymers", *Journal of Applied Physics* **85**(1), 628–629 (1999).

[41] P. Sommer-Larsen, J. Hooker, G. Kofod, K. West, M. Benslimane, and P. Gravesen, "Response of dielectric elastomer actuators", in *Smart Structures and Materials 2001: Electroactive Polymer Actuators and Devices*, edited by Y. Bar-Cohen, Proceedings of SPIE, Vol. 4329, pages 157–163, 2001.

[42] D. Stauffer, *Introduction to percolation theory*, Taylor & Francis, London, 1985.

[43] J. P. Clerc, G. Giraud, J. M. Laugier, and J. M. Luck, "The electrical conductivity of binary disordered systems, percolation clusters, fractals and related models", *Advances in physics* **39**(3), 191–309 (1990).

[44] L. J. Adriaanse, J. A. Reedijk, P. A. A. Teunissen, H. B. Brom, M. A. J. Michels, and J. C. M. Brokken-Zijp, "High-dilution carbon-black / polymer composites: hierarchical percolating network derived from Hz to THz ac conductivity", *Physical Review Letters* **78**(9), 1755–1758 (1997).

[45] M. T. Connor, S. Roy, T. A. Ezquerra, and F. J. B. Calleja, "Broadband ac conductivity of conductor-polymer composites", *Physical Review B* **57**(4), 2286–2294 (1998).

[46] C. Brosseua, P. Boulic, F. Queffelec, C. Bourbigot, Y. Le Mest, J. Loaec, and A. Beroual, "Dielectric and microstructure properties of polymer carbon black composites", *Journal of Applied Physics* **81**(2), 882–891 (1997).

[47] A. Faldt and G. Kofod, "Dielectric spectroscopy of graphite filled PDMS rubbers", Course report, May 1999.

[48] E. M. Dannenberg, L. Paquin, and H. Gwinnel, "Carbon black", *Encyclopedia of Chemical Technology* **4**, 1037–1074 (1992).

[49] Akzo Nobel, Literbuen 9, DK-2740 Skovlunde, *Polymer Additives: Ketjenblack EC*, black95 / 01 edition.

[50] AIS Analytical Instruments Systems GmbH, Hauptstr. 49, D-56412 Ruppach Goldhausen, *Alpha High Resolution Dielectric Analyzer: User's Manual*, 8 / 1998 edition, Distributed and supported by Novocontrol GmbH, D-56414 Hundsangen.

Risø–R–1286(EN)

[51] 3M, "VHB double coated acrylic foamtapes and adhesive transfer tapes", http://www.3m.com/us/mfg_industrial/adhesives/pdf/501622.pdf, March 1998.

[52] G. Kofod, R. Kornbluh, R. Pelrine, and P. Sommer-Larsen, "Actuation response of polyacrylate dielectric elastomers", in *Smart Structures and Materials 2001: Electroactive Polymer Actuators and Devices*, edited by Y. Bar-Cohen, Proceedings of SPIE, Vol. 4329, pages 141–147, 2001.

[53] P. C. Chou and N. J. Pagano, *Elasticity: tensor, dyadic, and engineering approaches*, Dover, Mineola, New York, 1992.

[54] O. H. Varga, "Stress-strain behaviour of elastic materials, selected problems of large deformations", in *Polymer Reviews*, edited by H. F. Mark and E. H. Immergut, Vol. 15, Interscience Publishers, London, 1966.

Bibiliographic Data Sheet **Risø–R–1286(EN)**

Title and authors

"Dielectric elastomer actuators" Guggi Heine Remme Kofod

ISBN

87–550–2924–8; 87–550–2925–6 (Internet)

ISSN

0106–2840

Department or group

The Danish Polymer Centre, Risø

Date

September, 2001

Sponsorship

THOR grant No. 9700882

Pages	Tables	Illustrations	References
139	1	48	54

Abstract

Ph.D. thesis regarding the manufacture and theoretical description of dielectric elastomer actuators (DEA). The DEA is best described as a compliant capacitor, in which both the insulating dielectric medium and the conducting electrodes can change size. The manufacture of actuators made from both 3M™ VHB™4910 tape, and silicone elastomer film is described. Several types of conducting electrodes have been developed and applied. Their performance has been measured using force feedback for establishing the strain response, and blocking force for establishing the force output. A model was derived from first principles, with no fitting parameters. The constituents of the model have been found from both experimental and theoretical approaches. This model fits very well with experimental results for silicone actuators, while it was more dubious for VHB™4910 actuators.

Available on request from Information Service Department, Risø National Laboratory, (Afdelingen for Informationsservice, Forskningscenter Risø), P.O. Box 49, DK-4000 Roskilde, Denmark. Telephone (+45) 4677 4004, Telefax (+45) 4677 4013.